

POLITECNICO DI MILANO

SCHOOL OF INDUSTRIAL AND INFORMATION ENGINEERING

DEPARTMENT OF ENERGY

MASTER OF SCIENCE IN NUCLEAR ENGINEERING



## Ion Beam Analysis with Laser-Driven Proton Beams

*Advisor:*  
Prof. Matteo Passoni  
*Co-Advisor:*  
Dr. Luca Fedeli

*Graduation Thesis of:*  
Francesco Mirani  
836181

ACADEMIC YEAR 2016-2017



# Contents

<b>Abstract</b>	<b>i</b>
<b>Sommario</b>	<b>iii</b>
<b>Estratto</b>	<b>v</b>
<b>1 Ion Beam Analysis and Ion Acceleration Systems</b>	<b>1</b>
1.1 Introduction to Ion Beam Analysis (IBA)	1
1.1.1 Analytical Spectroscopy Techniques	1
1.1.2 Particle Induced X-ray Emission (PIXE)	4
1.1.3 Rutherford Backscattering (RBS)	7
1.1.4 Elastic Recoil Detection (ERD)	12
1.1.5 Nuclear Reaction Analysis (NRA) and Particle Induced Gamma-Ray Emission (PIGE)	15
1.1.6 Neutron Activation Analysis (NAA)	17
1.2 Ion acceleration systems	19
1.2.1 Introduction to conventional accelerators	19
1.2.2 Van de Graaf generators and two stage tandem accelerators	21
1.2.3 Cyclotrons	22
1.3 Proton acceleration driven by superintense laser pulses	22
1.3.1 Basics of interaction of laser pulses with overdense targets	23
1.3.2 Sheath field formation at the rear side and ion acceleration	25
<b>2 PIXE and PIGE Spectroscopy</b>	<b>27</b>
2.1 Experimental apparatus for PIXE	27
2.1.1 Scattering chamber	27
2.1.2 In-air PIXE	28
2.1.3 Detection system	28
2.1.4 PIXE with heavy ions	29
2.1.5 Fluorescence and yield enhancement effects	30
2.1.6 Sources of background	31
2.2 Theoretical description of PIXE	32
2.2.1 Thin targets	32
2.2.2 Thick homogeneous target	34

## CONTENTS

2.2.3	Multilayer targets . . . . .	36
2.2.4	Generic non-homogeneous target . . . . .	37
2.3	PIGE analysis . . . . .	39
2.3.1	$\gamma$ -rays Spectrometry . . . . .	39
2.4	Theoretical description of PIGE . . . . .	41
2.4.1	PIGE analysis with standards . . . . .	42
2.4.2	PIGE bulk analysis without standards . . . . .	43
2.4.3	Resonance depth profiling . . . . .	43
2.5	Open issues and goals of the thesis work . . . . .	44
<b>3</b>	<b>Numerical simulation tools</b>	<b>47</b>
3.1	Geant4 Monte Carlo simulation toolkit . . . . .	47
3.1.1	<i>main()</i> program . . . . .	49
3.1.2	Mandatory user classes . . . . .	50
3.1.3	Optional user classes . . . . .	54
3.1.4	Executing the simulation . . . . .	55
3.2	Particle In Cell (PIC) simulation . . . . .	56
<b>4</b>	<b>PIXE analysis with laser-driven proton sources</b>	<b>58</b>
4.1	PIXE modeling for non-monoenergetic protons . . . . .	58
4.1.1	Thin target . . . . .	59
4.1.2	Thick homogeneous target . . . . .	61
4.1.3	Multilayer target . . . . .	63
4.1.4	Generic non-homogeneous target . . . . .	65
4.2	Monte Carlo simulation of PIXE data . . . . .	70
4.2.1	Physics processes . . . . .	70
4.2.2	Simulated experimental set-up . . . . .	71
4.2.3	Primary particles . . . . .	72
4.2.4	Detector and data recording . . . . .	72
4.2.5	Comparison with experimental data from literature . . . . .	74
4.3	Comparison between PIXE analysis with monoenergetic and exponential proton spectra . . . . .	76
4.3.1	Main assumptions . . . . .	76
4.3.2	Thin target . . . . .	77
4.3.3	Thick homogeneous target . . . . .	79
4.3.4	Multilayer target . . . . .	81
4.3.5	Generic non-homogeneous target . . . . .	83
4.3.6	Final considerations . . . . .	85
<b>5</b>	<b>A more realistic analysis: PIXE &amp; PIGE characterization of paint layers</b>	<b>87</b>
5.1	PIXE analysis using PIC laser-driven proton spectrum and a Von Hamos spectrometer . . . . .	87
5.1.1	Sample composition and type of analysis . . . . .	88

## CONTENTS

5.1.2	PIC simulation as Monte Carlo input . . . . .	88
5.1.3	Geometry set-up and Von Hamos detector configuration . . . . .	89
5.1.4	Results and considerations . . . . .	90
5.2	Characterization of paint layers with PIXE & PIGE . . . . .	93
5.2.1	<i>Differential PIXE</i> for the characterization of <i>Madonna dei Fusi</i> by Leonardo da Vinci . . . . .	93
5.2.2	PIGE for identification of Lapis-Lazuli in paintings . . . . .	99
<b>6</b>	<b>Conclusions</b>	<b>103</b>
6.1	Perspectives and open issues . . . . .	105
<b>A</b>	<b>Cross section</b>	<b>106</b>
A.1	Rutherford scattering cross section . . . . .	107
<b>B</b>	<b>Von Hamos detection system</b>	<b>109</b>
B.1	X-ray registration . . . . .	110
B.2	X-ray reflection . . . . .	110
<b>C</b>	<b>Block diagrams</b>	<b>113</b>
C.0.1	Hystograms of the codes . . . . .	113
C.0.2	Databases . . . . .	117

# List of Figures

1.1	Possible interactions involved in IBA. . . . .	3
1.2	Ion Beam Analysis experimental scheme. . . . .	3
1.3	Atomic energy level scheme (reproduced from [5]). . . . .	4
1.4	Fluorescence yield as a function of the atomic number $Z$ of the emitting element. . . . .	5
1.5	Ionization cross sections (from the Geant4 dataset). . . . .	6
1.6	A typical PIXE spectrum (reproduced from [5]). . . . .	6
1.7	Principle of RBS. . . . .	7
1.8	Interpretation of RBS spectra. . . . .	11
1.9	Principle of ERD. . . . .	12
1.10	Example of ERD spectrum(reproduced from [5]). . . . .	14
1.11	PIGE cross section for Na (reproduced from [42]). . . . .	17
1.12	Van de Graaff generator scheme. . . . .	21
1.13	Cyclotron accelerator scheme. . . . .	22
1.14	TNSA scheme. . . . .	25
1.15	Four proton energy spectra from different laser facilities (reproduced from [1]). . . . .	26
1.16	Maximum proton energy as a function of the irradiance for three possible ranges of laser pulse duration (reproduced from [47]). . . . .	26
2.1	Scattering chamber scheme (reproduced from [5]). . . . .	28
2.2	Scheme of Si(Li) detector (reproduced from [48]). . . . .	29
2.3	Absolute Si(Li) detector efficiency (reproduced from [5]). . . . .	29
2.4	Enhancement effect scheme. . . . .	30
2.5	Scheme of PIXE analysis with thin targets. . . . .	32
2.6	Scheme of PIXE analysis with thick targets. . . . .	35
2.7	Scheme of PIXE analysis with multilayer targets. . . . .	36
2.8	Scheme of PIXE analysis with generic non-homogeneous targets. . . . .	37
2.9	PIGE resonance depth profiling scheme . . . . .	44
2.10	Example of cross section from IBANDL database: $^{24}\text{Mg}(p, p\gamma)^{24}\text{Mg}$ , $90^\circ$ between beam direction and detector, $E_\gamma = 1369$ keV . . . . .	44
3.1	Geant4 class category diagram. . . . .	48

LIST OF FIGURES

3.2	Sampling of the distribution function with macro-particles. Each macro-particle has a definite momentum, but is extended in space.	57
4.1	Example of shaping function with temperature $\alpha = 0.6 \text{ MeV}^{-1}$ , $E_{p,min} = 1 \text{ MeV}$ and $E_{p,max} = 6 \text{ MeV}$ .	60
4.2	Differential yields for a thin target ( $1\mu\text{m}$ ) composed by 20% of Ni, 40% of Cr, 30% of Fe and 10% of Ti. The shaping function is the same reported in the fig. 4.1 and the X-ray lines considered are 7.46 keV for Ni, 5.41 keV for Cr, 6.4 keV for Fe and 4.51 keV for Ti.	60
4.3	$E(\rho r)$ for $E_p = 2, 3, 4, 5$ and $6 \text{ MeV}$ slowing down in a thick target composed by 40% of Ni, 30% of Cr and 30% of Mo.	62
4.4	Differential yields for thick target composed by 20% of 40% of Ni, 30% of Cr and 30% of Mo. The shaping function is the same reported in 4.1 and the X-ray lines considered are 7.46 keV for Ni, 5.41 keV for Cr and 17.4 keV for Mo.	63
4.5	$E(\rho r)$ for $E_p = 1, 2, 3, 4$ and $5 \text{ MeV}$ protons slowing down in a multilayer target composed by 20% of Ni and 80% of Mo for the first $3 \mu\text{m}$ layer, 40% of Ni and 60% of Cr for the second $9 \mu\text{m}$ layer, 30% of Cr and 70% of Mo for the third $17 \mu\text{m}$ layer. The shaping function is the same reported in fig. 4.1 and the considered X-ray lines are 7.46 keV for Ni, 5.41 keV for Cr and 17.4 keV for Mo.	64
4.6	Exponential proton energy spectrum with temperature $\alpha = 0.6 \text{ MeV}^{-1}$ , $E_{p,min} = 1 \text{ MeV}$ and $E_{p,max} = 6 \text{ MeV}$ , subdivided into energy intervals.	67
4.7	Summary of the analyzed cases for both monoenergetic protons (Sec. 2.2) and with an exponential energy spectrum (Sec. 4.1).	69
4.8	Geometry set-up of Monte Carlo simulations.	71
4.9	Monte Carlo simulation of PIXE with monoenergetic proton beam.	71
4.10	Monte Carlo simulation of PIXE with an exponential proton energy spectrum.	71
4.11	Example of a discrete probability distribution function for a proton energy spectrum with temperature $\alpha = 0.6 \text{ MeV}^{-1}$ , $E_{p,max} = 6 \text{ MeV}$ and $E_{p,min} = 1 \text{ MeV}$ .	72
4.12	Example of an energy spectrum of $10^5$ protons extracted from the distribution reported in fig. 4.11.	72
4.13	Detector intrinsic efficiency curve employed in all the Monte Carlo simulations.	73
4.14	Ratio of the X-ray yields (reproduced from [2]).	74
4.15	Nickel concentration profile (reproduced from [2]).	74
4.16	Comparison between experimental (reproduced from [2]) and simulated results.	75

LIST OF FIGURES

4.17	Ratio between the X-ray yields of Cu and Ni for different proton initial energies from Monte Carlo simulation and theoretical model.	76
4.18	Nickel concentration profile derived from the analysis of the Monte Carlo simulation outputs (blue) and expected nickel concentration profile (dotted line).	76
4.19	X-ray spectrum using monoenergetic protons for the thin target case.	78
4.20	Differential X-ray yields for the thin target case.	78
4.21	X-ray spectrum using monoenergetic protons for the thick target case.	80
4.22	Differential X-ray yields for the thin target case.	80
4.23	X-ray spectrum using monoenergetic protons for the multilayer target case.	81
4.24	Differential X-ray yields for the multilayer target case.	82
4.25	Concentration profile of the surface layer for a broach (reproduced from [36]).	83
4.26	Differential X-ray yields for the generic non-homogeneous target case.	84
4.27	Comparison between the real broach concentration profiles (dotted black line) and the ones derived from the analysis (blue line).	85
5.1	$d^2N_p(E_p, \theta)/dE_p d\theta$ , 2D PIC simulation output.	89
5.2	Bragg reflection scheme.	89
5.3	Planar Von Hamos spectrograph.	89
5.4	Full-cylinder Von Hamos geometry.	90
5.5	Running simulation.	90
5.6	First screen (pre-focus) and related spectrum.	90
5.7	Second screen (post-focus) and related spectrum.	90
5.8	Third screen (post-focus) and related spectrum.	91
5.9	Proton spectra from the PIC simulation (continuous line) and chosen for the analysis (dotted line).	91
5.10	Retrieved mass concentrations for different values of the spectrum temperature $\alpha$ .	92
5.11	<i>Madonna dei Fusi</i> by Leonardo da Vinci.	93
5.12	Spectra collected for four different energies on the hand of the Virgin (reproduced from [4]).	95
5.13	Comparison between the model result assuming exactly the sample composition reported in table 5.4 (continuous blue line), the model result without the <i>imprimitura</i> contribution to the Pb peak (dotted blue line) and the experimental result (red points) for monoenergetic protons.	97
5.14	Comparison between model results for monoenergetic protons (blue lines) and protons with exponential energy spectrum (red lines).	99



*LIST OF FIGURES*

5.15	Comparison between publication results (black points) and theoretical results (red points). . . . .	101
5.16	PIGE cross section for Na(p,p' $\gamma$ )Na reaction, $E_\gamma = 441$ keV at $135^\circ$ from the IBANDL database. . . . .	102
5.17	Comparison between the calculated $\gamma$ -ray yield in the case of monoenergetic protons (red points) and protons with exponential energy spectrum (blue points). . . . .	102
A.1	Particle beam orthogonally incident on a thin target. . . . .	106
A.2	Dependence of scattering on the impact parameter $b$ . . . . .	107
B.1	Integral reflectivity of the crystal. . . . .	109
B.2	Full-cylinder Von Hamos reflection scheme. . . . .	111
C.1	Block diagram of the code for the thin target analysis. . . . .	113
C.2	Block diagram of the code for the thick homogeneous target analysis. . . . .	114
C.3	Block diagram of the code for the Multilayer analysis. . . . .	115
C.4	Block diagram of the code for the Differential analysis. . . . .	116

# List of Tables

1.1	Examples of some X-ray energies. . . . .	5
1.2	Some important reactions for NRA from [5] . . . . .	16
1.3	Some important reactions for PIGE from [5]. . . . .	17
2.1	Ratio of secondary over primary yield for Fe and Ni (values from [49]). . . . .	31
4.1	Simulations outputs (counts/nC) and analysis results (%) for the thin target case. . . . .	79
4.2	Simulation outputs (counts/nc) and results of the analysis (%) for the thick target case. . . . .	81
4.3	Multilayer target structure set initially in the simulation. . . . .	81
4.4	Outputs and results for the multilayer target case. . . . .	82
4.5	Simulation outputs (counts / nC) for the Differential PIXE case. . . . .	84
5.1	Sword-scabbard bulk elemental composition. . . . .	88
5.2	Real concentrations vs. retrieved concentrations. . . . .	91
5.3	Ratio of the Hg over Pb peaks for different <i>incarnato</i> areas, reported in ref. [4]. . . . .	95
5.4	Modelling the composition of the painting in the four points considered in the analysis. . . . .	96



# Abstract

Ion Beam Analysis techniques allow to retrieve the composition of a sample by the irradiation with ion beams produced by an accelerator. These non-destructive analytical methods are widely used for scientific (e.g. biology, materials science and cultural heritage studies) and industrial (e.g. criminology, pollutant analysis and study of mineral samples) applications. Following the interaction with the particles, the atoms and nuclei of the material emit radiations (X-rays,  $\gamma$ -rays, etc.) which are characteristic of the atomic or isotopic species. Their detection allows to determine, in a non-destructive way, the elemental composition and the concentration profiles within a thickness of some  $\mu\text{m}$  from the surface of the sample. Two important IBA techniques are Particle Induced X-ray Emission (PIXE) and Particle Induced Gamma Ray Emission (PIGE). They are based respectively on the X-rays emitted due to ionization and  $\gamma$ -rays generated in nuclear reactions.

The proton sources used to perform PIXE and PIGE are Van de Graaff generators, TANDEM accelerators and cyclotrons, capable of producing monoenergetic proton beams with energy of few MeV. Despite their continuous development, accelerators still maintain high costs and size, preventing the large scale diffusion of IBA techniques.

Laser-driven ion acceleration could represent an alternative proton source for PIXE and PIGE. Laser-driven ion acceleration relies on ultra-intense ( $I > 10^{18} \text{ W/cm}^2$ ), ultra-short (10s fs - ps) laser pulses interacting with solid targets. Employing a compact table-top laser, it is possible to generate proton bunches characterized by an exponential energy spectrum with maximum energy equal to some MeV (so compatible with those traditionally adopted in PIXE and PIGE analysis).

The purpose of this thesis is therefore to study the feasibility of applying this type of source to PIXE and PIGE techniques.

Since the models currently available in literature for the description of PIXE and PIGE assume a monoenergetic proton source, the first step is to extend these models for an ion source with an exponential energy distribution. The theoretical description of PIXE and PIGE allows to implement iterative codes to retrieve the composition of a sample from a collection of experimental data (photon spectra).

In this thesis synthetic experimental data are simulated with a Monte Carlo

code, which accounts for all the physical processes relevant for the scenario of interest. Then, the developed iterative codes for the analysis of laser-driven PIXE spectra are employed in order to analyze the simulation results. This means that, starting from the X-ray yields obtained with the Monte Carlo, the composition of different samples has been retrieved using the iterative code. This will be done by first considering a very idealized set-up, then including the presence of a more realistic experimental apparatus. The aim of this procedure is to validate the developed models.

The final Chapter addresses the issue of a suitable photon detector for PIXE with a laser-driven source, since traditional Si(Li) detectors might be unsuitable due to their poor temporal resolution. A realistic detector based on crystal diffraction is simulated.

# Sommario

Le tecniche di Ion Beam Analysis permettono di ricavare la composizione di un campione tramite l'irraggiamento dello stesso con fasci di ioni prodotti da un acceleratore. Queste tecniche non distruttive sono ampiamente utilizzate in ambito scientifico (ad esempio in biologia, scienza dei materiali e beni culturali) e industriale (criminologia, analisi di inquinanti e analisi di minerali). In seguito all'interazione con le particelle del fascio, gli atomi e i nuclei del materiale emettono radiazioni (Raggi X, Raggi  $\gamma$ , etc.) caratteristiche della specie atomica o isotopica. La loro rilevazione consente di determinare, in modo non distruttivo, la composizione del campione e i profili di concentrazione entro uno spessore di alcuni  $\mu\text{m}$  dalla sua superficie. La Particle Induced X-ray Emission (PIXE) e la Particle Induced Gamma Ray Emission (PIGE) sono due importanti tecniche IBA. Esse si basano rispettivamente sui raggi X emessi a seguito di ionizzazione e sui raggi  $\gamma$  generati in reazioni nucleari.

Le sorgenti di protoni impiegate per svolgere la PIXE e la PIGE sono i generatori di Van de Graaff, gli acceleratori TANDEM e i ciclotroni, capaci di produrre fasci monoenergetici di protoni con energia di alcuni MeV. Nonostante il loro continuo sviluppo, gli acceleratori mantengono ancora oggi dimensioni e costi elevati, impedendo la diffusione su larga scala delle tecniche IBA.

L'accelerazione tramite laser potrebbe rappresentare una sorgente alternativa per PIXE e PIGE. Essa si basa su impulsi laser ultra-intensi ( $I > 10^{18} \text{ W/cm}^2$ ) e ultra-brevi (10s fs - ps) che interagiscono con target solidi. Tramite l'utilizzo di un laser da tavolo compatto, è possibile generare impulsi di protoni caratterizzati da uno spettro di energia esponenziale con una energia massima pari ad alcuni MeV (compatibile con quelle tradizionalmente impiegate nell'analisi PIXE e PIGE).

Pertanto, lo scopo di questa tesi è studiare la fattibilità nell'applicare questo tipo di sorgente alle tecniche PIXE e PIGE.

Poiché i modelli attualmente disponibili in letteratura per la descrizione di PIXE e PIGE assumono una sorgente mono-energetica di protoni, il primo passo è quello di estendere questi modelli ad una sorgente di ioni con uno spettro di energia esponenziale. La descrizione teorica di PIXE e PIGE consente di implementare codici iterativi per ricavare la composizione di un campione a partire da una raccolta di dati sperimentali (spettri di fotoni).

In questa tesi i dati sperimentali sintetici vengono simulati con un codice Monte

Carlo, in grado di riprodurre tutti i processi fisici rilevanti per lo scenario di interesse. Vengono quindi utilizzati i codici iterativi sviluppati per l'analisi di spettri PIXE laser-driven per analizzare i risultati della simulazione. Ciò significa che, a partire dalle rese dei raggi X ottenuti con il Monte Carlo, è stata ricavata la composizione di diversi campioni utilizzando il codice iterativo. Questo sarà fatto prima considerando una set-up molto idealizzata, poi includendo la presenza di un apparato sperimentale più realistico. Lo scopo di questa procedura è quello di validare i modelli sviluppati.

Il capitolo finale affronta la questione di individuare un rivelatore di raggi X appropriato per PIXE eseguita con una sorgente laser, in quanto i rivelatori tradizionali Si(Li) potrebbero essere inadatti a causa della loro scarsa risoluzione temporale. Verrà simulato un detector realistico basato sulla diffrazione di un cristallo.

# Estratto

In questa tesi viene studiata la possibilità di svolgere analisi di Particle Induced X-ray Emission (PIXE) e Particle Induced Gamma Ray Emission (PIGE) impiegando sorgenti di protoni da laser. In particolare, sono stati sviluppati e successivamente validati i modelli per la descrizione teorica della PIXE e della PIGE eseguita con protoni non monoenergetici.

L'Ion Beam Analysis (IBA) rappresenta una famiglia di tecniche analitiche per la caratterizzazione elementare dei campioni. Queste metodologie sono basate sull'interazione tra un fascio di particelle primarie, generalmente protoni con energia di alcuni MeV, e gli atomi (o i nuclei) del campione indagato. Durante l'irraggiamento viene generata una grande varietà di prodotti, le cui proprietà sono caratteristiche della composizione del campione. Di conseguenza, la misura delle particelle secondarie emesse consente di determinare quali elementi sono presenti, in che concentrazioni, e come sono distribuiti lungo lo spessore (ricavarne i profili di concentrazione). Queste tecniche sono accumulate dal fatto di essere non distruttive, di misurare concentrazioni dell'ordine di ppm e di sondare spessori che si estendono fino a diversi  $\mu\text{m}$  dalla superficie del campione.

Tra le varie tecniche raggruppate nell'IBA, è importante menzionare la Particle Induced X-ray Emission (PIXE) e la Particle Induced Gamma Ray Emission (PIGE). La prima è basata sulla misura dei raggi X emessi a seguito delle ionizzazioni indotte dal fascio di protoni incidente. Nella PIGE ciò che viene registrato sono i raggi  $\gamma$  emessi durante le reazioni nucleari indotte dalle particelle primarie. Tanto i raggi X quanto i raggi  $\gamma$  sono caratteristici dell'elemento o dell'isotopo emettitore. Altri due esempi di tecniche IBA sono la Rutherford Backscattering (RBS) e l'Elastic Recoil Detection (ERD). La RBS coinvolge la misura degli ioni del fascio incidente ad angoli all'indietro in seguito a urto elastico con i nuclei del bersaglio. Viceversa, nell'ERD le particelle misurate sono i nuclei di ricollo del bersaglio ad angoli in avanti a seguito di urto elastico con gli ioni del fascio. In entrambi i casi, le energie delle particelle registrate sono impiegate per ricavare la distribuzione degli elementi lungo lo spessore del campione.

Al giorno d'oggi, le tecniche IBA sono svolte in circa 300 centri di ricerca nel mondo e per diverse applicazioni. Tra gli ambiti in cui sono impiegate troviamo la biologia, la scienza dei materiali, criminologia, analisi di inquinanti, mineralogia, archeologia e analisi dei beni culturali.



L'apparato sperimentale impiegato per svolgere attività di Ion Beam Analysis prevede l'utilizzo di un acceleratore di particelle, generalmente un generatore di Van de Graaff o un ciclotrone, capace di fornire protoni monoenergetici con energie di alcuni MeV e correnti che possono andare da decine di pA a decine di nA. Nonostante la continua evoluzione degli acceleratori, queste macchine presentano ancora alcuni svantaggi: sono molto costose, hanno grandi dimensioni (quindi non sono trasportabili per svolgere misure in situ) e l'energia dei fasci prodotti non è facilmente modificabile.

In questo contesto, una possibile alternativa è rappresentata dalle sorgenti laser-plasma. L'interazione tra un impulso laser super-intenso ultra-breve e un target solido è in grado di generare un bunch di protoni caratterizzati dall'aver uno spettro di energia esponenziale, il cui valore massimo può arrivare anche a diverse decine di MeV. Il numero di protoni accelerati ad ogni sparo può variare tra  $10^9$  e  $10^{12}$  part/MeV. Gli spari possono essere eseguiti con una frequenza che può arrivare fino a decine di Hz. Una sorgente di protoni di questo tipo presenterebbe tutta una serie di vantaggi, in particolare:

- Portabilità (fondamentale nel momento in cui i campioni non possono essere trasportati, come nel caso di alcuni beni culturali quali affreschi, statue e grandi quadri).
- Meno costosa degli acceleratori di particelle.
- In linea di principio, possibilità di svolgere un'analisi molto rapidamente, al limite con un singolo sparo.
- Energie massime più elevate (fino a decine di MeV invece che alcuni MeV), quindi possibilità di sondare spessori maggiori del campione.
- Elevata corrente e laminarità alla sorgente.
- Possibilità di analizzare ampie aree (la dimensione dello spot dell'impulso di protoni sul campione può avere dimensioni di  $\text{cm}^2$ ).

L'obiettivo di questa tesi è di studiare la possibilità di impiegare sorgenti di protoni da laser per svolgere Ion Beam Analysis, in particolare la Particle Induced X-ray Emission e Particle Induced Gamma Ray Emission.

Come menzionato all'inizio di questo estratto, la PIXE e la PIGE sono basate rispettivamente sulla misura dei raggi X e  $\gamma$  emessi durante l'irraggiamento di campioni con fasci di protoni. Il risultato delle misure sperimentali consiste in degli spettri contenenti i picchi caratteristici dei raggi X e  $\gamma$ . La presenza degli elementi è riconoscibile dalle linee caratteristiche negli spettri, mentre la loro concentrazione è calcolabile a partire dalle rese associate a ciascun picco tramite appositi codici (ad esempio GUPIX e GeoPIXE). Questi sono basati su una modellizzazione teorica della tecnica, in particolare su equazioni in grado di fornire il numero di fotoni misurati in funzione delle proprietà del materiale

(la concentrazione), quantità fisiche (e.g. la sezione d'urto di ionizzazione) e i parametri dell'apparato sperimentale (e.g. l'angolo solido sotteso dal detector). Per quanto riguarda la PIXE, è possibile studiare diverse tipologie di campioni adottando il modello appropriato al fine di estrarre informazioni di natura diversa. In particolare, si possono analizzare target sottili o spessi, entrambi di composizione omogenea. In questo caso l'obiettivo della misura è quello di determinare la concentrazione massica degli elementi presenti. Considerando un target multilayer composto da diversi strati omogenei, e assumendo di conoscere a priori la composizione elementare di ognuno di essi, è possibile ricavarne gli spessori. In fine, è possibile anche considerare il caso di un target dotato di una composizione e distribuzione degli elementi lungo lo spessore completamente incognite. In questo caso, è possibile sfruttare una variante della PIXE nota come *PIXE Differenziale*. Essa, impiegando un certo numero di fasci a energie diverse, permette di ricavare i profili di concentrazione degli elementi nel campione.

I modelli teorici oggi disponibili in letteratura, necessari per l'analisi quantitativa degli spettri PIXE, prevedono di impiegare solo uno spettro monoenergetico di protoni. Di conseguenza, il primo obiettivo di questa tesi è quello di estendere i suddetti modelli includendo la possibilità di utilizzare anche protoni caratterizzati dall'averne uno spettro non monoenergetico. Ciò è stato fatto considerando tutti e quattro i casi citati.

Un secondo punto cruciale consiste nel testare la validità dei modelli sviluppati. Questo può essere fatto considerando dei dati per le rese dei raggi X ottenuti da campioni di composizione nota e irraggiati con sorgenti di protoni da laser. Tramite l'applicazione di un procedimento iterativo basato sui modelli sviluppati, è possibile ricavare le concentrazioni degli elementi presenti, gli spessori dei layer o i profili di concentrazione. Confrontando i valori ottenuti con quelli realmente presenti nei campioni si può stabilire se l'analisi ha avuto successo e se i modelli sono corretti.

Il primo articolo [1] volto a proporre e dimostrare sperimentalmente la possibilità di eseguire la PIXE con una sorgente di protoni da laser è stato pubblicato durante lo svolgimento di questa tesi. Gli autori mostrano come sia possibile registrare lo spettro dei raggi X, quindi riconoscere gli elementi presenti nel campione. Attraverso l'uso di un codice Monte Carlo, dimostrano come una sorgente di protoni da laser non sia più distruttiva di un normale acceleratore nei confronti del campione. Tuttavia essi non conducono alcun genere di analisi quantitativa. Quindi, in assenza di un numero consistente di dati sperimentali in letteratura, è stato necessario impiegare uno strumento numerico opportuno per simulare un ipotetico esperimento PIXE eseguito con protoni da laser. Questo strumento e la simulazione Monte Carlo.

Di conseguenza, è stato preparato un primo set di simulazioni, iniziando con l'impiego di una sorgente di protoni dotata di uno spettro puramente esponenziale e assumendo di impiegare un detector molto idealizzato. I raggi X entranti in un volume cilindrico rappresentante il detector sono registrati in uno spettro,

previa applicazione di una funzione di efficienza e di una funzione di risposta. I modelli sviluppati sono stati innanzitutto testati sui risultati di queste simulazioni.

In un secondo tempo, è stata sviluppata la simulazione di un set-up sperimentale più realistico. In questo caso, lo spettro dei protoni generati dal Monte Carlo non è più un semplice esponenziale, ma è il risultato di una simulazione Particle-In-Cell (PIC). Per quanto riguarda il detector, è stato proposto e implementato nella simulazione uno spettrometro di Von Hamos. Esso prevede l'impiego di un cristallo capace di riflettere su uno schermo i raggi X, disperdendoli tramite la riflessione di Bragg. La simulazione è rappresentativa di un impulso con  $10^{11}$  protoni, un numero compatibile con quelli generati da alcuni laser in un singolo sparo. L'analisi delle rese restituite dalla simulazione è stata eseguita con il modello sviluppato, assumendo di poter trattare lo spettro come un semplice esponenziale. I risultati rimangono in accordo con la composizione originariamente impostata nel codice Monte Carlo. Non solo, è stato anche osservato che una variazione della temperatura dello spettro influisce in modo trascurabile sui valori delle concentrazioni ricavate.

L'ultima parte di questo lavoro ha coinvolto l'applicazione della PIXE e della PIGE all'ambito dei beni culturali, in particolare all'analisi dei dipinti. Più precisamente, sono state valutate le potenzialità della PIXE svolta con protoni dal laser nel caratterizzare la composizione stratigrafica dei dipinti. Per quanto riguarda la PIGE, è stata studiata la sensibilità di questa tecnica nel rilevare la presenza dei lapis-lazuli tramite la misura dei raggi  $\gamma$  caratteristici del sodio.

La prima parte del Capitolo 1 costituisce un'introduzione all'Ion Beam Analysis e vi sono presentate in modo generale le principali tecniche che fanno parte di questa famiglia. Oltre alla PIXE, PIGE, RBS e ERD già menzionate in precedenza, vengono trattate la Nuclear Reaction Analysis (NRA) e la Neutron Activation Analysis (NAA). La NRA si basa sulle reazioni nucleari che avvengono tra gli ioni incidenti e i nuclei del bersaglio, con emissione di particelle di diversa natura ( $\gamma$ , p,  $\alpha$ , etc.). La NAA non rientra tra le tecniche IBA in quanto le particelle incidenti sul campione non sono ioni, ma neutroni. Tuttavia, per via della sua importanza, è stata comunque inclusa una sua breve descrizione. In particolare, l'irraggiamento di un materiale tramite neutroni termici può produrre reazioni nucleari che lasciano i nuclei in stati eccitati. In seguito si ha diseccitazione con emissione di radiazione caratteristica.

Nella seconda parte del capitolo vengono brevemente descritti gli acceleratori di particelle impiegati per svolgere studi IBA. I più diffusi sono i generatori di Van de Graaff, i Tandem e i ciclotroni. I primi due sono basati sulla generazione di un forte campo elettrostatico tra la messa a terra e un conduttore su cui viene accumulata una elevata quantità di carica. Gli ioni emessi dalla sorgente vengono accelerati in questo campo. Viceversa, i ciclotroni sono acceleratori in cui il moto degli ioni è circolare. Questi ultimi fanno uso di campo elettrico alternato e di un campo magnetico ortogonale al piano in cui le particelle si muovono. Alla fine del capitolo si trova una descrizione delle sorgenti laser-

plasmi, in particolare del regime di interazione noto come Target Normal Sheth Acceleration (TNSA).

Il capitolo 2 contiene una descrizione più dettagliata della PIXE e della PIGE, per via dell'importanza che queste due tecniche rivestono nel lavoro svolto. Nella sezione conclusiva sono anche riportati gli obiettivi della tesi.

Il Capitolo inizia dalla PIXE, evidenziando il fatto che essa può essere svolta sia in vuoto, attraverso l'uso di un'apposita camera, che in aria. Segue una breve descrizione dei detector Si(Li) generalmente impiegati e delle possibili sorgenti di background nello spettro. Viene anche menzionata una variante della PIXE eseguita con ioni pesanti e il meccanismo noto come *enancement effect*. In quest'ultimo, l'emissione di raggi X, detti primari, indotti dall'interazione con il fascio di protoni induce a sua volta fluorescenza nel campione producendo raggi X detti secondari.

La trattazione prosegue con l'esposizione dei modelli presenti in letteratura per descrivere i vari tipi di analisi PIXE. Come detto in precedenza, nel caso di target omogenei, sottili o spessi, l'analisi è volta a ricavare le concentrazioni degli elementi presenti. Nel caso di target multilayer, nota la composizione di ogni strato, è possibile ricavarne gli spessori. Per tutti queste tipologie l'analisi può essere svolta impiegando un solo fascio di protoni monoenergetici. In fine, nel caso in cui la composizione del campione sia completamente incognita, è possibile, impiegando più fasci di protoni aventi energie diverse, ricavare i profili di concentrazione. Per quanto riguarda la PIGE, viene svolta una descrizione del tutto analoga considerando prima l'apparato sperimentale, poi il modello necessario a svolgere l'analisi quantitativa. Il capitolo si conclude con l'esposizione degli obiettivi della tesi.

Nel Capitolo 3 vengono esposti, in via del tutto generale, gli strumenti numerici necessari a svolgere il lavoro di tesi: il toolkit Geant4 per le simulazioni Monte Carlo e il metodo Particle-In-Cell (PIC). Geant4 è un toolkit di classi astratte per simulare il trasporto di particelle nella materia. Oltre al passaggio di particelle primarie di diversa natura, permette di simulare le interazioni conseguenti, la generazione e il successivo trasporto delle particelle secondarie. Sarà questo lo strumento impiegato per simulare la PIXE, una volta definito lo spettro dei protoni da impiegare e impostato nel codice della simulazione. Per avere a disposizione uno spettro realistico con cui generare protoni nel Monte Carlo, verrà impiegato il metodo PIC. Si tratta di un metodo per la simulazione cinetica dei plasmi che, tramite un approccio lagrangiano ed euleriano combinato, fornisce una soluzione al sistema di equazioni Maxwell-Vlasov.

Nella prima parte del Capitolo 4 sono stati estesi i modelli presentati nel Capitolo 2 al fine di includere nella descrizione della PIXE la possibilità di impiegare protoni non monoenergetici. Come già accennato questo lavoro è stato svolto sistematicamente per tutti e 4 i casi di interesse. Considerando nello specifico il caso della PIXE differenziale, l'impiego di protoni a energie differenti implica di poter sondare spessori diversi del campione. La derivazione dei profili di concentrazione tramite il modello si basa su questa osservazione.

Quindi, l'estensione più diretta al caso non monoenergetico prevede l'impiego di più impulsi di protoni per i quali viene modificata l'energia massima dello spettro.

Una possibile alternativa consiste nell'utilizzo di un singolo sparo e nella raccolta separata dei raggi X associati a intervalli di energia diverse nello spettro dei protoni incidenti. Infatti, dato che i protoni sono emessi tutti nello stesso istante di tempo, arriveranno sul campione distribuiti in una certa finestra di tempo. La sua durata dipenderà dalla differenza tra l'energia massima e minima nello spettro di energia dei protoni e dalla distanza tra la sorgente e il campione. Concettualmente, sarebbe quindi necessario raccogliere separatamente i raggi X prodotti in intervalli di tempo consecutivi e corrispondenti agli intervalli di energia dei protoni nello spettro. Ovviamente questa alternativa implica di poter disporre di un detector molto veloce, in grado di raccogliere separatamente i raggi X emessi in intervalli di tempo consecutivi e della durata di  $ns$  o decine di  $ns$ .

Il Capitolo prosegue con una descrizione dettagliata della prima simulazione Monte Carlo e con la riproduzione tramite lo stesso di un caso di analisi PIXE con protoni monoenergetici presente in letteratura. Il confronto tra i dati sperimentali riportati in [2] e i risultati della simulazione ha permesso di comprovare la validità del Monte Carlo.

La seconda parte del Capitolo mostra i risultati dell'analisi svolta tramite il modello teorico, applicato alle rese generate con le simulazioni (e protoni dotati di spettro esponenziale). In tutti e 4 i casi, la composizione del campione ricavata è in accordo con quella impostata inizialmente nel codice Monte Carlo. Questo conferma la validità dei modelli sviluppati. Lo stesso procedimento è stato svolto considerando gli stessi campioni, ma svolgendo la simulazione con protoni monoenergetici. Da un confronto si evince come la sensibilità nella misura sia pressochè la stessa per le due tipologie di sorgenti.

Il Capitolo 5 si divide in due parti: nella prima parte viene eseguita una simulazione Monte Carlo in cui viene impiegato uno spettro PIC di energia dei protoni e si utilizza uno spettrometro di Von Hamos per registrare i raggi X; nella seconda parte si esegue uno studio volto a testare le potenzialità della PIXE e della PIGE svolte con protoni da laser nell'analisi dei dipinti.

L'ultima simulazione eseguita in questo lavoro considera il caso di un campione spesso e omogeneo riprodotto la composizione del fodero di una spada romana [3]. Lo spettro dei protoni incidenti inserito nel Monte Carlo è a sua volta il risultato di una simulazione PIC, quindi più realistico rispetto ad una semplice funzione esponenziale. Si è anche considerato il caso di un detector più adatto a raccogliere lo spettro dei raggi X emessi. Ovviamente, dato che i detector a Si(Li) presentano un tempo morto che è dell'ordine dei  $\mu s$ , questi ultimi non possono essere impiegati per registrare raggi X emessi in una finestra di tempo che è dell'ordine di decine di  $ns$ . Viceversa, un detector passivo come lo spettrometro di Von Hamos non presenterebbe problemi di tempo morto. Esso si basa sulla riflessione dei raggi X tramite un cristallo su uno schermo (ad es-

empio, un Imaging Plate). L'obiettivo dell'analisi è quindi quello di verificare se, approssimando lo spettro dei protoni nel modello ad un puro esponenziale, i risultati in termini delle concentrazioni ricavate rimangono corretti. Si è voluto in oltre testare quanto il risultato dell'analisi sia dipendente dalla temperatura dello spettro dei protoni ipotizzata nel modello.

Anche in questo caso le concentrazioni ricavate sono risultate in accordo con i valori impostati nel Monte Carlo. In oltre, la loro dipendenza dalla temperatura dello spettro ipotizzata è molto debole. Questo suggerisce una buona solidità dell'analisi PIXE svolta con protoni da laser rispetto a un parametro soggetto a forti variazioni da misura a misura.

Per quanto riguarda l'analisi dei dipinti, si è voluta testare innanzitutto la capacità della PIXE svolta con protoni da laser nel ricavare informazioni sulla loro struttura multilayer. In [4], è stata stimata la composizione di alcuni punti del dipinto *Madonna dei Fusi* di Leonardo da Vinci, facendo uso di diversi fasci di protoni aventi energie diverse. Dato l'elevata complessità di questo tipo di campione, è da escludere la possibilità di ricavare veri e propri profili di concentrazione. Tuttavia, assumendo di essere di fronte a una struttura multilayer e considerando che le rese dei raggi X sono rappresentative solo dalla composizione degli strati attraversati dai protoni, gli autori dell'articolo sono riusciti ad individuare gli spessori dei vari layer che compongono la *Madonna dei Fusi*. Lo stesso tipo di ragionamento è stato testato considerando di impiegare protoni da laser aventi diverse energie massime negli spettri. Questo è stato fatto ricavando l'andamento del rapporto delle rese in funzione dell'energia massima, tramite il modello teorico, previa conoscenza della composizione del dipinto (da [4]).

Un ragionamento del tutto analogo a quanto esposto è stato fatto anche per testare la sensibilità della PIGE eseguita con protoni da laser nell'identificazione dei lapis-lazuli. Considerando la composizione di diversi campioni aventi concentrazione di lapis-lazuli sempre minore, si è impiegato il modello teorico per calcolare la resa dei raggi  $\gamma$  generati per via dell'irraggiamento con protoni da laser. Si è riscontrato che la sensibilità è analoga a quella che ci si aspetta impiegando protoni monoenergetici.

Nel Capitolo 6 sono riportate le conclusioni di questo lavoro, oltre a una serie di possibili obiettivi futuri. In particolare, è di fondamentale importanza testare sperimentalmente quanto simulato in questo lavoro, in modo da poter applicare i modelli a effettivi dati sperimentali. E' anche necessario individuare possibili detector alternativi agli spettrometri di Von Hamos, possibilmente caratterizzati da un'efficienza maggiore. In fine, per quanto riguarda l'applicazione ai beni culturali, potrebbe essere opportuno fare una valutazione del possibile danno provocato su di essi da impulsi di protoni da laser.

La trattazione è completata da tre appendici. La prima riguarda la definizione di sezione d'urto e il suo calcolo in un caso specifico (lo scattering di Rutherford). La seconda presenta nel dettaglio lo spettrometro di Von Hamos considerato e come è stato inserito nella simulazione Monte Carlo. La terza mostra la rapp-

resenzione tramite diagrammi di flusso dei codici sviluppati per l'analisi degli spettri PIXE svolta con protoni da laser.

# Chapter 1

## Ion Beam Analysis and Ion Acceleration Systems

### 1.1 Introduction to Ion Beam Analysis (IBA)

#### 1.1.1 Analytical Spectroscopy Techniques

*Ion Beam Analysis (IBA)* [5, 6, 7] is a wide group of analytical techniques employed for the elemental characterization of samples, based on the interaction of few MeV ion beams with materials. IBA techniques can be used to perform various interdisciplinary studies for the identification and quantification of elements in geological, biological, industrial, metallurgic and cultural heritage samples. IBA can be considered as a part of a larger collection of methods born from the applied research in the atomic and nuclear low energy physics. The grouping of different techniques in the same family can follow different criteria, for example they can be shared by the same type of incident primary or emitted secondary particles. In this Section, an overview of the main analytical methods is reported.

#### **X-ray spectroscopy**

*X-ray spectroscopy* techniques [8, 9] use the generation of X-rays through the ionization and subsequent de-excitation in the probed sample (see Sec. 1.1.2). *Electron microscopy* relies on electrons as primary particles, for *X-ray Fluorescence (XRF)* ionization is induced with x-rays. If the primary particle is an ion, the technique is called *Particle Induced X-ray Emission (PIXE)* [5, 8, 10, 11, 12].

#### **Electron spectroscopy-based techniques**

On the other hand, in *X-ray Photoelectron Spectroscopy (XPS)* and *Auger Electron Spectroscopy (AES)* [13, 14, 15, 16], the X-rays cause ionizations to which follows the emission of the electrons. In the case of XPS the electrons directly



emitted during the ionization event are detected, in the case of AES they are the Auger electrons that can be produced in the de-excitation.

### **Primary ions-based spectroscopy techniques**

*Secondary Ion Mass Spectroscopy (SIMS)* and *Ion Scattering Spectroscopy (ISS)* are united by the use of primary particles with energies of some *keVs*. In ISS [17, 18, 19], the energy of the primary particles that can be elastically scattered from surface atoms is measured. The analysis is based on the fact that this energy depends on the mass of the atoms involved.

As far as SIMS [20, 21, 22] is concerned, the process of interest is the penetration of primary ions into solid matter and the creation of damages of different nature, such as dislocations in the lattice. In the so called "sputtering" process, ions, molecules or clusters of molecules can be ejected from the target and their detection can provide information about the sample.

The latter two techniques have many affinities with *Rutherford Backscattering (RBS)* and *Elastic Recoil Detection (ERD)*, which however rely on higher energy ions, in the order of several MeV [5]. The reader can find a detailed description in Sec. 1.1.3 and 1.1.4.

Among other methods widely used in surface analysis worth mentioning are *Raman spectroscopy*, *Scanning Electron Microscopy (SEM)* and *X-ray Diffraction (XRD)*. Briefly, the *Raman spectroscopy* [23, 24] is based on the irradiation of the sample with laser pulses (visible range). The photons scattered by the molecules lose an amount of energy equal to that of the vibrational states, and they are analyzed by a spectrometer. On the other hand, *SEM* [25, 26] is a topographical technique that employs an electron beam incident on the sample and is based on the detection of the backscattered electrons to provide an image of the surface.

X-ray Diffraction [27] employs an electromagnetic wave interacting with an ordered array of atoms like an ionic crystal, producing a secondary wave (of the same wavelength) scattered in all directions by the atoms. The secondary waves give rise to interference phenomena. Constructive interference results in diffracted rays scattered only along well-defined directions. The directions and the intensities of the diffracted rays depend on the crystal symmetry, on the atomic number and spatial distribution of the atoms inside the crystal.

### **IBA general concept**

When ions with energies of the order of some MeV per nucleon are made to collide with a material, many interactions can take place generating different kinds of products, as it is shown schematically in fig. 1.1.

Among these, there are X-rays,  $\gamma$ -rays, backscattered projectiles, recoiled ions and nuclear reaction products. The essence of IBA lies in the detection of the emitted secondary particles, whose properties are related with the sample composition.

These techniques, which are subject to some degree of complementarity, allow to determine the sample elemental composition with an accuracy of few ppm and to derive the elemental composition depth profile up to some micrometers from the surface. Despite the different nature of the interactions involved, there are some features in common between the different kinds of analysis:

- They are in general non-destructive techniques and thus suitable to study very delicate materials such as artifacts of historical and artistic importance.
- A small amount of sample (few milligrams) is needed.
- Only the portion of the sample directly stricken by the beam is probed.
- They allow performing multielemental measures.
- They do not require sample preparation.

Conceptually, the experimental set-up scheme required to perform IBA is presented in fig. 1.2 and it is fairly common to all techniques falling within this category.

In the first part of this Chapter some IBA techniques will be briefly presented,

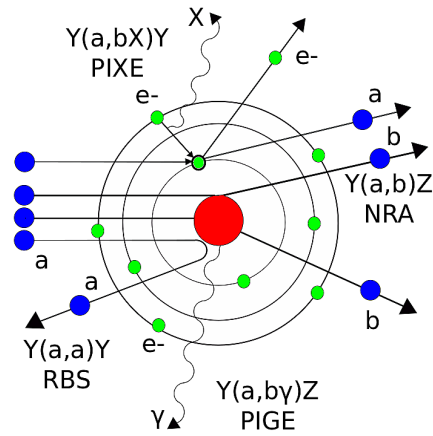


**Figure 1.1:** Possible interactions involved in IBA.

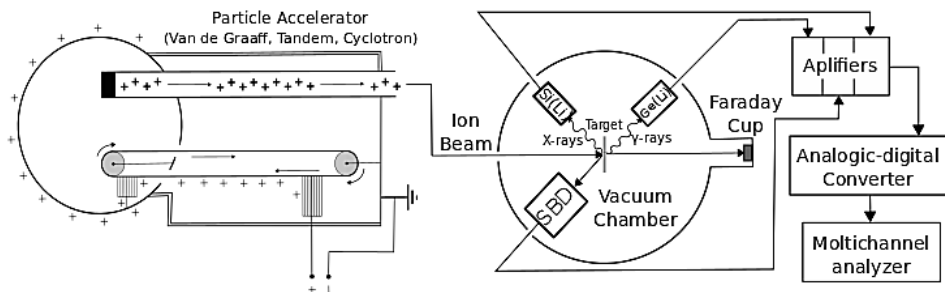


**Figure 1.2:** Ion Beam Analysis experimental scheme.

taking as reference the description provided in [5] and adopting the same formalism, while in the second one several ion beam sources will be described.

### 1.1.2 Particle Induced X-ray Emission (PIXE)

Particle Induced X-ray Emission (PIXE) is a well-established X-ray emission spectroscopy technique based on the measurement of the energy, or equivalently the wavelength, and the number of the emitted X-rays following excitation with an ion beam. The characteristic energies allow to recognize the elements (qualitative analysis) while, recording the X-ray intensities, their concentrations can be determined (quantitative analysis).

When a charged particle impinges on the sample, generally protons with initial energy of  $1 \div 5$  MeV, an electron can be ejected from an inner shell of an atom producing a vacancy (this process is called ionization). Very quickly, an outer shell electron will drop into the vacancy in a de-excitation process and an amount of energy equal to the difference between the binding energy of the two atomic shells involved is released. Then, the de-excitation can follow two different channels: the emission of an Auger electron or the emission of a photon. When an Auger electron is emitted, the excess of energy involved in the de-excitation is transferred to a higher shell electron with lower binding energy with respect to the one previously released. Consequently, this electron is ejected from the atom. In the other case an amount of energy equal to the difference between the two shells is directly emitted from the atom in the form of an X-ray. Due to the fact that the binding energies of the shells are well-defined for each element, this is the useful process in order to probe the sample because the released photon is characteristic of the emitter and it can be observed with a proper detector.

In the following Sections some basic concepts related to PIXE are introduced, while a more detailed description of this technique will be provided in Sec.2.1 and Sec. 2.2, because of its relevance for this thesis work.

#### The Mosley law and X-ray energies

In fig. 1.3 a simple energy levels scheme is reported with some examples of transitions, which of course identify also the characteristic emitted X-rays. The Siegbahn notation [28, 29] is used to name the spectral lines. A spectral series is a group of homogeneous lines (e.g. the  $K\alpha_1$  or  $L\alpha_1$ ) for which Mosley, in 1913, derived an experimental relation between the frequency  $\nu$  of the emitted X-ray and the atomic number

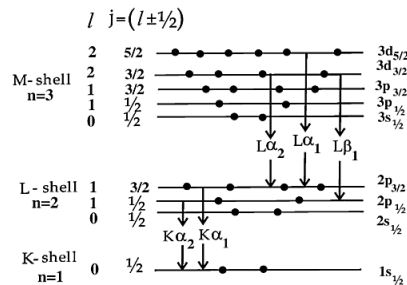


**Figure 1.3:** Atomic energy level scheme (reproduced from [5]).

$Z$ :

$$\nu = Q(Z - \sigma)^2 \quad (1.1)$$

In eq. 1.1,  $Q$  is a proportionality constant (e.g.  $(3R/4)c$  for  $K\alpha$  or  $(5R/36)c$  for  $L\alpha$  where  $R$  is the Rydberg constant and  $c$  is the speed of light) and  $\sigma$  is called screening constant. This relation shows that the X-ray energy, and thus also the frequency, increases quadratically with the atomic number and it is lower for higher electronic shells involved. Altogether, the X-ray energies range from few hundreds of eV to tens of keV, as it is shown in table 1.1.

**Table 1.1:** *Examples of some X-ray energies.*

Z	Elem.	$K\alpha$ (keV)	$L\alpha$ (keV)	Z	Elem.	$K\alpha$ (keV)	$L\alpha$ (keV)
13	Al	1.49	~	50	Sn	25.27	3.45
20	Ca	3.69	0.34	55	Cs	30.97	4.29
25	Mn	5.90	0.64	60	Nd	37.36	5.22
30	Zn	8.63	1.01	65	Tb	44.48	6.26
35	Br	11.89	1.48	70	Yb	52.39	7.41
40	Zr	15.73	2.04	79	Au	68.8	9.66
45	Rh	20.21	2.69	83	Bi	77.12	10.77

### The fluorescence yield

As far as X-ray emission spectroscopy is concerned, an important parameter is the fluorescence yield  $\omega_x$ , which has to be taken into consideration due to its effect on the intensity of the emitted spectra.

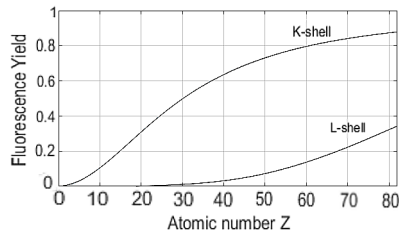


**Figure 1.4:** *Fluorescence yield as a function of the atomic number  $Z$  of the emitting element.*

It is defined in terms of the ratio of radiative  $\sigma_x$  to total transition probabilities for a specific spectral line:

$$\omega_x = \frac{\sigma_x}{\sigma_x + \sigma_A} \quad (1.2)$$

where  $\sigma_A$  represents the Auger process probability. As reported in fig. 1.4, the fluorescence yield increases with the atomic number and it can differ significantly from one shell to another ( $\omega_K$  is higher than  $\omega_L$ ).

### The ionization cross section

One of the main advantages of PIXE is the large value of the ionization cross sections, which are shown in fig. 1.5 (a general description of the concept of cross section can be found in Appendix A). In the proton energy range commonly

employed, these are of the order of thousands of barns both for the K-series of the low  $Z$  elements and for the L-series of the high  $Z$  elements. This fact, combined with the behavior of the fluorescence yield, guarantees an exceptionally high X-ray intensity when compared to other analytical techniques employing nuclear reactions, for which the cross section is often in the order of millibarns.

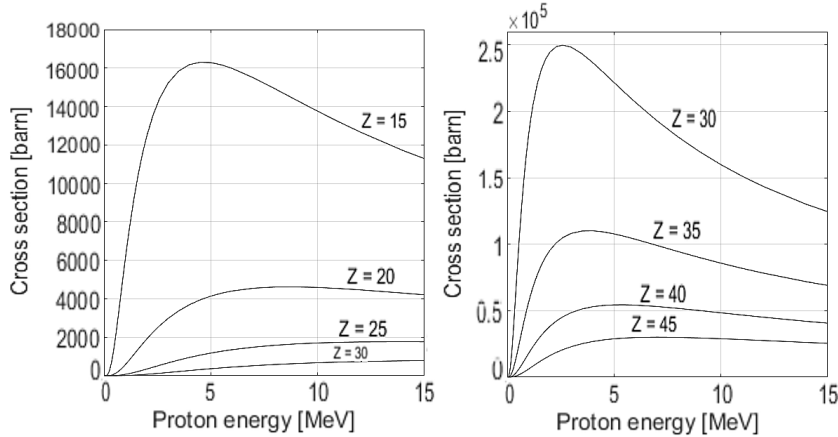


**Figure 1.5:** Ionization cross sections (from the Geant4 dataset).

### Recording and read-out of the spectrum

The detection of X-rays is usually performed using a Si(Li) or Ge semiconductor detectors and a typical result of a PIXE measurement is shown in fig. 1.6.

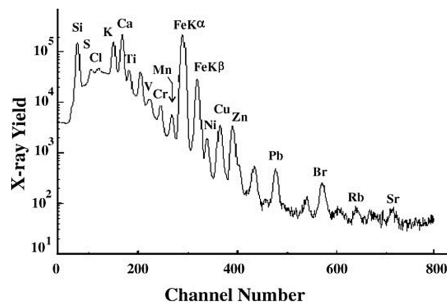


**Figure 1.6:** A typical PIXE spectrum (reproduced from [5]).

The X-ray energies of interest are below 20 keV where the K photons for  $Z < 40$  and the L photons for heavier elements lie. The qualitative analysis is performed comparing the peaks present in the spectrum with the values reported in tables. In case of overlapping of different peaks, the elements are recognized from the presence of other characteristic non-overlapping lines.

The quantitative analysis with PIXE is possible because the number of emitted x-rays is directly proportional to the concentration of the element generating them. It can be performed following two different strategies: the system calibration using reference standards, or the adoption of an absolute analytical method. Nowadays there are different programs capable of performing the absolute analysis without the presence of any standards, such as GUPIX [30] and GeoPIXE [31]. These codes are based on a

formalism which will be presented in Sec. 2.2.

A brief summary of key features of PIXE is given in the following. First of all, as mentioned above, it is a non-destructive technique that allows both qualitative and quantitative analysis. Given the high yield of X-ray production, this is a relatively fast analysis (generally it requires few minutes) and it is characterized by an excellent sensitivity (ppm). Practically, since X-rays with energy lower than 1 keV are strongly absorbed into the typically analyzed samples (or any other layer between the sample and the active volume of the detector), PIXE allows to detect elements starting from Sodium to Uranium.

The main disadvantage of PIXE is the complete lack of information about the organic components of the samples or the chemical bonds. However, given the multi-elementarity detection capacity of the technique, it is possible to deduce information about molecular composition on the basis of stoichiometry and known concentrations of the individual elements.

PIXE is currently used to carry out environmental [32, 33], geological [34], biological [35] and archaeological [36] studies. In addition, PIXE is of crucial importance also in the field of cultural heritage preservation [4, 37, 38, 39]. In fact, knowing the composition of the materials of an artwork is fundamental because it allows to check the degradation and to assist experts in choosing compatible and reversible restoration techniques.

### 1.1.3 Rutherford Backscattering (RBS)

Rutherford Backscattering Spectroscopy (RBS) is an analytical technique which can provide the depth distribution of impurities in surface layers through the detection of particles elastically backscattered from the sample, as it is shown in fig. 1.7. In RBS, monoenergetic primary ions such as protons, deuterons and  $\alpha$ -particles with energy equal to 1÷3 MeV impinge on the sample. Traveling inside the material, they can be deflected at an obtuse angle by the electrostatic field of a nucleus. If this backscattered particles still have enough energy to leave the sample, they can be detected. Below, the fundamental parameters needed to correctly interpret a RBS spectrum are described.

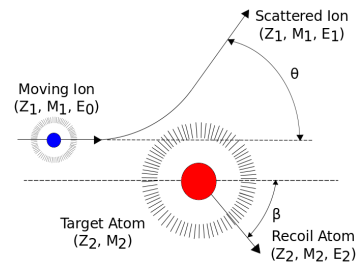


**Figure 1.7:** *Principle of RBS.*

#### Kinematic factor

The kinematic factor associated to the backscattered particles  $K_{bs}$  is defined as the ratio between the projectile energy before and after a collision and it is

given by the following relation (refer to fig. 1.7).

$$K_{bs}(\theta, M_1, M_2) = \frac{E_1}{E_0} = \left( \frac{(M_2^2 - M_1^2 \sin^2 \theta)^{1/2} + M_1 \cos \theta}{M_1 + M_2} \right)^2 \quad (1.3)$$

Here the assumptions are elastic interaction, projectile energy  $E_0$  much larger than the binding energies of the target atom and absence of nuclear reactions. In eq. 1.3,  $M_1$  and  $M_2$  are the projectile and target masses respectively, while  $\theta$  is the scattering angle in the laboratory reference frame. The kinematic factor do not depend on the initial energy of the primary particles and it can be expressed only as a function of the mass ratio  $M_2/M_1$  and  $\theta$ . So, fixing the scattering angle  $\theta$ , the projectile mass  $M_1$  and initial energy  $E_0$ , the identification of an element can be made on the bases of  $K_{bs}$ , which is uniquely related to  $M_2$ .

It can be noticed that the mass resolution of RBS analysis is higher for lighter elements because the amount of momentum transferred from the projectile to the target nucleus is more significant for smaller  $M_2$ .

### Rutherford scattering cross section

The probability that a primary particle would be scattered in a certain direction, as the result of a Coulombian collision, can be expressed in terms of the Rutherford differential scattering cross section, here expressed in the laboratory reference system:

$$\left( \frac{d\sigma}{d\Omega} \right)_{lab,bs} = \left( \frac{Z_1 Z_2 e^2}{8\pi\epsilon_0 E_0} \right)^2 \frac{1}{\sin^4 \theta} \frac{[M_2 \cos \theta + (M_2^2 - M_1^2 \sin^2 \theta)^{1/2}]^2}{M_2 (M_2^2 - M_1^2 \sin^2 \theta)^{1/2}} \quad (1.4)$$

The reader can find a description of Rutherford cross section in Appendix A. Assuming  $M_2 \gg M_1$ :

$$\left( \frac{d\sigma}{d\Omega} \right)_{lab,bs} \approx \left( \frac{Z_1 Z_2 e^2}{16\pi\epsilon_0 E_0} \right)^2 \frac{1}{\sin^4(\theta \setminus 2)} \quad (1.5)$$

In this equation  $E_0$  and  $\theta$  are the incident particle energy and the scattering angle in the laboratory frame,  $Z_1$  and  $Z_2$  are the atomic numbers of the incident ion and target nucleus. It worth to point out that the differential cross section is very forward picked, going as  $1 \setminus \sin^4(\theta \setminus 2)$  and decrease with the projectile energy as  $1 \setminus E_0^2$ .

The number of particles detected per unit time  $dN$  can be expressed as:

$$dN = \left( \frac{d\sigma}{d\Omega} \right)_{lab} N(nt) d\Omega \quad (1.6)$$

where  $N$  is the number of particles hitting the target per unit time and unit area,  $nt$  is the number of atoms in the material per unit area,  $d\Omega$  is the solid angle subtended by the detector.

### Stopping power and energy straggling

A final important quantity, which has to be mentioned before considering the shape of the spectra obtained performing RBS, is the energy lost by a particle traveling inside matter per unit path length, called stopping power  $S(E)$  and given by the Bethe-Bloch formula:

$$S(E) = -\frac{dE}{dx} = 4\pi N_A r_e^2 m_e c^2 \rho \frac{Z}{A} \frac{z^2}{\beta^2} \left[ \frac{1}{2} \ln \left( \frac{2m_e c^2 \beta^2 \gamma^2 T_{max}}{I^2} \right) - \beta^2 - \frac{\delta}{2} \right] \quad (1.7)$$

where  $N_A$  is the Avogadro number,  $r_e$  is the electron radius,  $m_e$  is the electron mass,  $I$  is the mean excitation potential of the material,  $Z$  and  $A$  are the atomic and mass number of the material,  $z$  is the incident particle charge in units of  $e$ ,  $\rho$  is the material density,  $\beta$  is the particle velocity in units of  $c$ ,  $\gamma$  is equal to  $1/\sqrt{1-\beta^2}$ ,  $T_{max}$  is the maximum energy transferable to an electron in a collision and  $\delta$  is a correction for the density at high energies. Usually for RBS spectra calculations, the energy loss is expressed in terms of stopping cross section  $\varepsilon = \frac{1}{N} \frac{dE}{dx}$ , being  $N$  the medium number density.

The interactions causing the slowing down of primary particles are essentially of two types: inelastic collisions with electrons of the medium and elastic collision with the sample nuclei. In the energy range of interest for RBS, energy loss is mainly due to the first type of interaction.

The stopping power  $S(E)$  allows to calculate the correlation between depth and energy and this suggests that the resolution be strongly influenced by the uncertainty on both the initial energy of the impinging particles and the spread in energy loss along the path inside the material, called energy straggling. The straggling is the consequence of the statistical fluctuation in terms of kind and number of encounters which the projectile can face during its path.

### Particle detectors

In this section, some detectors employed to detect the scattered particles are listed:

- *Surface Barrier Detectors (SBD)*

SBD are semiconductor diodes working in current mode characterized by a very linear response and available with a thin entrance window (protons with 1 MeV energy loose about 14 keV). In general, they are made with n-type silicon and the active area is approximately equal to 50 mm<sup>2</sup>. Basically, when the ionizing radiation interacts with the active medium it produces free electrons in the conduction band and holes in the valence band which generate a transient current in the external circuit under the influence of an electric field. As the number of electron-hole pairs is proportional to the energy deposited by the radiation in the semiconductor and the energy necessary to create one of them is known, the signal can be used to measure the intensity of the incident radiation.



- *$\Delta E$  vs.  $E$  telescopes*

A solid state  $\Delta E$  vs.  $E$  telescope is formed by various active mediums of known thicknesses placed one over the other and by a hodoscope, an instrument used to detect passing charged particles and determine their trajectories. A particle entering in the detector with an angle  $\alpha$  with respect to the normal (measured with the hodoscope) deposits an energy  $\Delta E$  in the first thin detector and an energy  $E'$  in the second thick one. Assuming  $dE/dx \approx \Delta E/(\Delta L \sec \alpha) \sim Z^2/v^2$  because of the Bethe-Bloch formula and  $E \approx E' \approx Mv^2/2$  neglecting the attenuation in the first detector, it can be assumed that  $(dE/dx)E \sim Z^2M$ . This final quantity is unique for each element, where  $\Delta L$  is the first detector thickness,  $M$  and  $Z$  are the incident particle mass and charge.

- *Microchannel plate detectors (MCP)*

A MCP is a slab of conductive glass, 2 mm approximately thick, made of an array of small capillaries. The microchannels have a diameter of about  $10 \mu\text{m}$  and they are parallel to each other, oriented to the normal of the plate with an angle of  $\sim 8^\circ$ , ensuring that each particle entering in the channels will interact with the surface. The impact triggers a cascade of electrons which propagates inside the channel wall under the action of an electric field. When the electrons exit the channel, they are collected on an anode and the total current is measured by an external circuit. MCP have the advantages of being compact, small, they have good timing properties, high gain and allow performing 2D imaging.

- *Magnetic spectrometers*

Magnetic spectrometers are based on the principle that when a particle of charge  $q$  enters in a constant magnetic field  $B$  it is deflected in a circular trajectory of radius  $r$ , leading in the orthogonal plane with respect to the magnetic field direction. This is caused by the Lorentz force and the relation between the momentum of the particle  $p$  and the radius  $r$  is given by  $p = qBr$ . Every trajectory is followed by all particles having the same momentum-to-charge ratio. The deflected particles can be selected on the basis of the trajectory making use of a slit and, varying the value of  $B$ , the energy spectrum can be measured.

## **RBS spectra interpretation**

Considering a thin layer on the surface of the sample and characterized by a different elemental composition with respect to the substrate, the resulting backscattered particle energy spectrum will present a single peak at energy  $E_1 = kE_0$  and a continuum, as it is shown in fig. 1.8. The peak is due to the thin layer while the continuum is related to the substrate. In this case the energy loss in the thin layer is lower than the experimental resolution.

In the case of the presence of a thick layer at a certain depth inside the target,

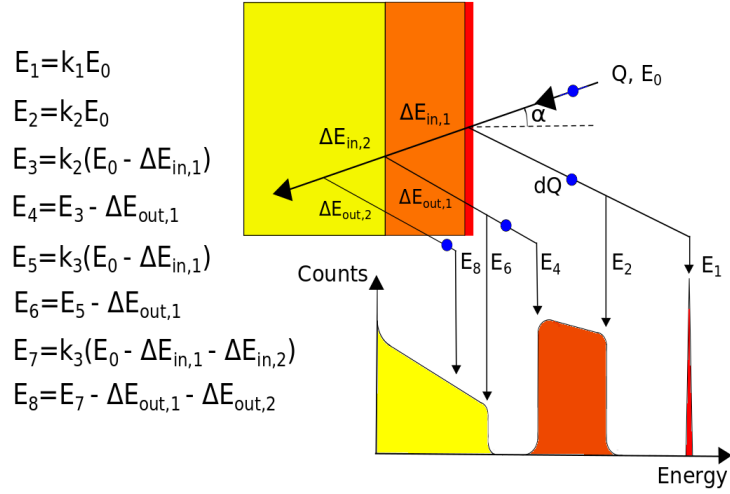


**Figure 1.8:** Interpretation of RBS spectra.

the energy loss has to be taken into account and the peak becomes a brick whose thickness is representative of the layer thickness.

In both cases, the detected particle number can be related to the sublayer thickness  $\Delta x$  expressed in terms of atoms/cm<sup>2</sup> through the cross section (eq. 1.8). This massive thickness is related to the concentration of the element in the layer through the density.

$$dQ = Q d\Omega \left( \frac{d\sigma}{d\Omega} \right)_{lab,bs} \frac{\Delta x}{\cos \alpha} \quad (1.8)$$

In eq. 1.8,  $Q$  is the number of incident particles impinging at the angle  $\alpha$  with respect to the normal,  $dQ$  is the number of counts of backscattered particles, related to the peak area,  $d\Omega$  is the detector solid angle and  $(\frac{d\sigma}{d\Omega})_{lab,bs}$  is the differential cross section expressed by eq. 1.4.

In conclusion, the position of the recorded signal is related to the mass of the element through the cinematic factor  $K_{bs}$ , the width of the signal is connected to the thickness through the stopping power  $S$  and the height is connected with the elemental concentration through the cross section. In any case, the spectrum analysis is generally performed using computer codes such as the Transport of Ions in Matter, TRIM [40], in order to simulate the experiment and then interpret the result.

In conclusion, RBS is a non-destructive technique widely used for near-surface layers elemental analysis in solids for elements from Be to U. It is quantitative without standards with typical precision of  $\pm 3\%$ . The depth range is typically 2-20  $\mu\text{m}$  with resolution of  $5 \div 50$  nm. Due to the fact that the cross section is proportional to  $Z_2^2$ , RBS is particularly suitable for the identification of heavy elements in light matrices.

RBS is currently employed for the absolute determination of film and surface layer thicknesses, distribution in depth of surface impurities and elemental composition of complex materials.

#### 1.1.4 Elastic Recoil Detection (ERD)

With respect to RBS, which make use of the backscattered primary particles, Elastic Recoil Detection (ERD) is based on the detection of the recoiled target nuclei elastically scattered in the forward direction (see the scheme reported in fig. 1.9).

While for Rutherford Backscattering the mass of the projectile has to be lower with respect to the mass of target nuclei in order to be scattered in the backward direction, ERD is performed using heavy projectiles (from C to Au) with energy  $\sim 1$  MeV/u in order to recoil the sample nuclei in the forward direction. A filter is placed in front of the detector to stop the heavier primary particles scattered in the same direction of the secondary ones. ERD is able to provide mass and concentration profile information of the elements within the surface layers.

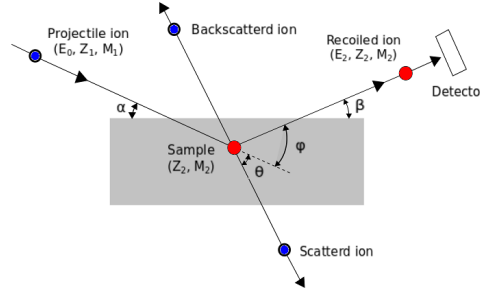


Figure 1.9: Principle of ERD.

#### Fundamental concepts

Again, the fundamentals of ERD are:

- The energy transferred in the elastic two-body collision through the concept of kinematic factor  $k_{er} = \frac{E_2}{E_0}$ . Here, the ratio is not between the projectile energies before  $E_0$  and after  $E_1$  the collision as for  $k_{bs}$  defined in eq. 1.3, but between  $E_0$  and the energy of the recoiled particle  $E_2$ :

$$k_{er} = \frac{4M_1M_2 \cos^2 \theta}{(M_1 + M_2)^2} \quad (1.9)$$

where  $M_1$  and  $M_2$  are the projectile and recoiled atom masses and  $\theta$  is the recoil angle. Clearly, the fraction of energy retained by the incident particle is given by  $k_{bs} = \frac{E_1}{E_0}$  (eq. 1.3).

- The probability of occurrence of the event, so that a secondary recoiled particle would be scattered in a certain direction, through the concept of differential scattering cross section  $(d\sigma/d\Omega)_{lab,er}$  (here expressed in the

laboratory reference frame).

$$\left(\frac{d\sigma}{d\Omega}\right)_{lab,er} = \left(\frac{Z_1 Z_2 e^2}{8\pi\epsilon_0 E_0}\right)^2 \frac{(1 + M_1 \setminus M_2)^2}{\cos^3 \theta} \quad (1.10)$$

where  $Z_1$  and  $Z_2$  are the atomic numbers of the projectile and of the target atom. The  $1 \setminus E_0^2$  dependence shows that the number of recoiled particles decreases with the energy of the primaries  $E_0$ , so with the depth because of the projectiles slow down starting from the initial energy  $E_0$ .

- The energy loss of the projectile moving inside the medium (concept of stopping power  $S$ ) expressed in terms of a relative energy loss factor.

$$S_{rel} = \frac{dE_0 \setminus dx}{E_0} \frac{1}{\sin \alpha} + \frac{dE_2 \setminus dx}{E_2} \frac{1}{\sin \beta} \quad (1.11)$$

where  $E_0$  and  $E_2$  are the primary and secondary particle energy before and after the collision,  $\alpha$  and  $\beta$  are the incident and exit angles of the incident beam and recoiled particles, as it is shown in fig. 1.9. The energy resolution of course depends upon the relative energy resolution  $\delta E_2 \setminus E_2$  and the relative energy loss:

$$\delta x = \frac{\delta E_2}{E_2} (S_{rel})^{-1} \quad (1.12)$$

As in the case of RBS, the resolution depends also on the energy straggling.

### ERD spectra measurement and interpretation

ERD, starting from H, allows to detect almost all possible elements with a sensitivity equal to 1% and to perform depth profiling with a precision less than 10 nm. The projectiles employed are heavy ions with energy of 20-200 MeV and in particular of 2 MeV for He in the case of H detection. The accessible depth range is in the order of 1  $\mu\text{m}$ .

The simplest experimental set-up involves the use of a Surface Barrier Detector (SBD). Since heavier target elements generate higher detected energies, in the case of heavy element substrate the presence of a high background is observed, which shadows the contribution of light elements. So, as lighter particles have a smaller stopping power with respect to the heaviest one, the contribution coming from light elements can be separated simply eliminating the one coming from the heaviest by a stopping foil in front of the detector. Cutting the contribution from the heaviest elements, the part of the spectrum related to the light elements becomes clearly visible and the separation of 3 - 4 of them is possible. Also in this case, applying the listed physical parameters, the energy spectrum of the recoiled particles can be converted into a concentration profile.

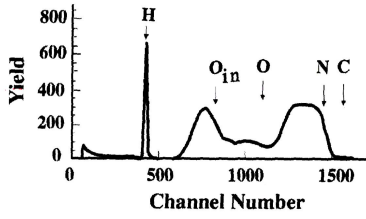


**Figure 1.10:** *Example of ERD spectrum (reproduced from [5]).*

depth profile cannot be reconstructed. This depends on the stopping power which affects the depth resolution  $\delta x$ : the energy loss factor for H is smaller than for N.

In some cases, in particular when the concentration ratio between two elements is small and they are superimposed in the spectrum, it is difficult to separate the contributions. Furthermore, the energy resolution of the detection system strongly affects the depth resolution of the whole analysis. Therefore, as the resolution of SBD degrades increasing  $Z$ , they are not the best choice performing ERD. So, alternative detection systems are generally employed, based on the detection of the recoiled particle kinetic energy (associated with the signal amplitude) and the measurement of another characteristic parameter.

The parameters and the corresponding detection systems are the velocity in time-of-fly spectrometry (time is related to velocity through the traveled distance), momentum-over-charge ratio in magnetic spectrograph or stopping power in  $\Delta E$  vs.  $E$  telescopes.

The depth profile is given by the backward calculation of the recoiling depth  $x$ , linking the energy of the incident projectiles  $E_0$  with the energy of the detected secondary particles  $E_2$ :

$$E_2 = k_{er} \left( E_0 - \frac{x\varepsilon_{in}}{\sin \alpha} \right) - \frac{x\varepsilon_{out}}{\sin(\phi - \alpha)} \quad (1.13)$$

where  $\varepsilon_{in}$  and  $\varepsilon_{out}$  are the stopping powers of the primary and secondary particles inside the material and  $k_{er}$  is the kinematic factor provided by eq. 1.9. The yield of the detected recoils  $Y(x)$  is given by:

$$Y(x) = N(x) \left( \frac{d\sigma}{d\Omega} \right)_{lab,er} (E_0 - \varepsilon_{in}(x \backslash \cos \alpha)) n_i \Delta x d\Omega \quad (1.14)$$

where  $N(x)$  is the number of incident ions reaching the depth  $x$ , the differential scattering cross section  $d\sigma/d\Omega_{lab,er}$  is given by eq. 1.10,  $n_i$  is the total number of incident ions,  $d\Omega$  is the detector solid angle and  $\Delta x$  is the ion path length in the sample.

### 1.1.5 Nuclear Reaction Analysis (NRA) and Particle Induced Gamma-Ray Emission (PIGE)

Nuclear Reaction Analysis and Particle Induced Gamma-Ray Emission are complementary methods to PIXE for the detection of light elements. Here the interactions involve nuclear forces. In NRA, the primary ions are absorbed by the analyte nuclei and a different secondary particle is promptly emitted and detected. So this technique is not only element-specific, but also isotope-specific. Due to the fact that the energy of the products is a function of the projectile energy, also the depth distribution can be evaluated from the energy distribution of the emitted secondary particles. Also, the presence of resonances in the reaction cross section can help to obtain a depth scale for the impurity concentrations.

PIGE is based on a restricted class of nuclear reactions, such as  $(p, \gamma)$ ,  $(p, p\gamma)$  and  $(p, \alpha\gamma)$ , involving the emission of a  $\gamma$ -ray and its detection. This kind of event doesn't always happen for all the elements, so in some cases PIGE can be not applicable. For light primary particles of energy up to 3 MeV, the only accessible elements are those with  $Z$  lower than 15, so PIGE is restricted to the detection of light elements.

#### Nuclear Reaction Analysis

In NRA, and also in the case of PIGE, the energy of the primary particles has to overcome the Coulomb barrier  $B_c$  in order to enable the projectile to reach the nucleus and produce a nuclear reaction:

$$B_c = \frac{Z_1 Z_2}{(M_1^{1/3} + M_2^{1/3})} [\text{MeV}] \quad (1.15)$$

In eq. 1.15,  $Z_1$  and  $Z_2$  are the projectile and target atomic numbers,  $M_1$  and  $M_2$  are the masses respectively. From this equation it can be shown that  $B_c$  is generally of the order of 1 MeV, so primaries with energy in the range 1 ÷ 5 MeV are generally employed. The products' ( $\gamma$ , p, n, d,  $\alpha$ , etc.) yield is proportional to the isotope concentration.

A general equation can be written in order to represent any kind of reaction which can take place:

$$a + X \rightarrow X^* \rightarrow Y + b + n\gamma \quad (1.16)$$

$$Q = E_b + E_Y + E_\gamma - E_a \quad (1.17)$$

where  $a$  is the incident particle of kinetic energy  $E_a$ ,  $X$  is the target nucleus,  $X^*$  is the compound nucleus,  $Y$  and  $b$  are the reaction products of kinetic energy  $E_Y$  and  $E_b$  and  $Q$  is their excess of energy. The sign of  $Q$  discriminates between endothermic reactions ( $Q < 0$ ), characterized by a critical energy for  $E_1$  under which the reaction can not take place, and exothermic reactions ( $Q > 0$ ) for

which any value of  $E_1$  is permissible.

Another important distinction is between Resonant NRA, characterized by the presence of resonances in the cross sections and usually employed to determine depth scaling of impurities, and Non-resonant NRA. In this second case the analysis is almost equivalent to RBS, apart from the different kinematics.

For the detection of charged particles, solid-state surface barrier detectors are employed combined with the presence of a stopper foil. The sheet ensures a reduction in the particle energy, which is then stopped in the detector active volume (this is especially important when exothermic reactions are involved).

Usually NRA is employed to detect the elements from H to Al with good

**Table 1.2:** *Some important reactions for NRA from [5]*

Reaction	Incident Ion Energy (MeV)	Emitted Energy (MeV)	Cross Section (mb/sr)
${}^2\text{H}(\text{d},\text{p}){}^3\text{H}$	1.0	2.3	5.2
${}^2\text{H}({}^3\text{He},\text{p}){}^4\text{He}$	0.7	13.0	61
${}^6\text{Li}(\text{d},\alpha){}^4\text{He}$	0.7	9.7	35
${}^7\text{Li}(\text{p},\alpha){}^4\text{He}$	1.5	7.7	9
${}^{11}\text{B}(\text{p},\alpha){}^8\text{Be}$	0.65	3.70	550
${}^{12}\text{C}(\text{d},\text{p}){}^{13}\text{C}$	1.2	3.1	35
${}^{15}\text{N}(\text{p},\alpha){}^{12}\text{C}$	0.8	3.9	15
${}^{18}\text{O}(\text{p},\alpha){}^{15}\text{N}$	0.73	3.4	15
${}^{19}\text{F}(\text{p},\alpha){}^{16}\text{O}$	1.25	6.9	0.5
${}^{23}\text{Na}(\text{p},\alpha){}^{20}\text{Ne}$	0.592	2.24	4
${}^{31}\text{P}(\text{p},\alpha){}^{28}\text{Si}$	1.514	2.734	16

sensitivity in the order of ppm. The main disadvantages are the possible high levels of radiations related to the emission of  $\gamma$ -rays and neutrons in addition to the complexity of the spectra recorded, which increases with higher energy of primary particles. This is a consequence of the increment in the number of possible channels for the reactions increasing the energy of the projectiles.

In table 1.2 are listed some important nuclear reactions employed in NRA.

### Particle Induced Gamma-Ray Emission

Particle Induced  $\gamma$ -ray Emission (PIGE) is based on the emission of  $\gamma$  photons following excitation due to the interaction between the sample nuclei and projectiles (generally protons with energy of  $3 \div \text{MeV}$ ). This analysis is alternative to PIXE because the best sensitivity is for elements with  $Z$  between 3 and 20. The difficulties concerning PIGE are essentially due to the shape and magnitude of the cross sections: they are orders of magnitude lower than the ionization cross sections, they decrease with  $Z$  for the target nuclei due to the increasing of

the Coulomb repulsion (only low  $Z$  elements can be detected) and it is difficult to find energy regions for which they are monotonic to perform a simple bulk analysis. An example is reported in fig. 1.11.

While in NRA the attenuation in energy of the emitted charged particles allows to perform depth scaling like in the case of ERD or RBS, in PIGE this is not possible because the  $\gamma$  rays are only attenuated in intensity and not in energy. Anyway, depth profile information can be obtained exploiting the presence of resonances in the cross sections for PIGE: changing the initial proton energy, also the position where the resonance is reached inside the material changes, producing  $\gamma$  rays according to the local composition.

A special advantage of PIGE is the possibility to detect at the same time the major elemental components of organic samples such as C, N, O, and Na. Due to a certain lack of knowledge in the cross sections, the PIGE quantitative analysis is mainly performed with the use of reference standards [41]. More details can be found in Sec. 2.4.1. In any case, in [42] a code for quantitative analysis without standards inspired to the one used for PIXE analysis is presented (see Sec. 2.4.2).

Finally, in table 1.3 are listed some common nuclear reaction employed in PIGE.

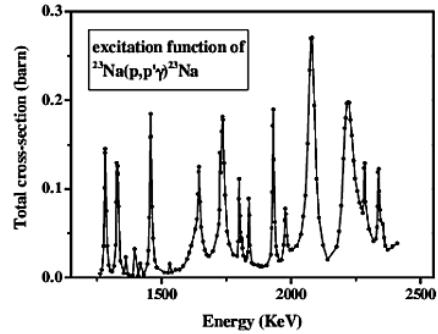


**Figure 1.11:** PIGE cross section for Na (reproduced from [42]).

**Table 1.3:** Some important reactions for PIGE from [5].

Reaction	E- $\gamma$ (keV)	Reaction	E- $\gamma$ (keV)
${}^7\text{Li}(p,n\gamma){}^7\text{Be}$	429	${}^{27}\text{Al}(p,p'\gamma){}^{27}\text{Al}$	843, 1013
${}^9\text{Be}(p,\gamma){}^{10}\text{B}$	478	${}^{28}\text{Si}(p,p'\gamma){}^{28}\text{Si}$	1779
${}^{10}\text{B}(p,\alpha\gamma){}^7\text{Be}$	717	${}^{31}\text{P}(p,p'\gamma){}^{31}\text{P}$	1266
${}^{15}\text{N}(p,\alpha\gamma){}^{12}\text{C}$	4439	${}^{32}\text{Si}(p,p'\gamma){}^{32}\text{Si}$	2230
${}^{18}\text{O}(p,p'\gamma){}^{18}\text{O}$	1982	${}^{35}\text{Cl}(p,p'\gamma){}^{35}\text{Cl}$	1220, 1763
${}^{19}\text{F}(p,p'\gamma){}^{19}\text{F}$	110, 197, 1236, 1349, 1357	${}^{41}\text{K}(p,\alpha\gamma){}^{38}\text{Ar}$	2168

### 1.1.6 Neutron Activation Analysis (NAA)

Neutron Activation Analysis is not an IBA technique because it does not make use of ions as projectiles. In any case, due to its importance and because sometimes neutrons are generated employing an ion beam as primary particles (see Sec. 1.1.6), it will be also described in this Chapter.

NAA is based on the irradiation of the sample with neutrons and the consequent



conversion of the stable atoms in  $\gamma$ -emitting radioisotopes. The  $\gamma$ -rays are characteristic of the emitter, so of the parent element initially involved in the reaction. It is important to emphasize that this is a comparative technique, so it requires the use of standards of known concentration for the elements of interest.

The mainly involved reaction is the neutron capture and the subsequent  $\beta$ -decay followed by the emission of a  $\gamma$ -photon. Due to the fact that the cross section for this process is higher for lower projectile energy, the employed neutrons are generally thermalized ( $E_n \sim 0.025$  eV).

The qualitative analysis is made on the basis of the observed  $\gamma$ -ray energies with a Ge(Li) or HpGe semiconductor detector, while for a quantitative analysis the fundamental quantity is the intensity of the emitted photons. In particular the number of  $\gamma$ -rays emitted per unit time by the unknown sample is compared to the number of  $\gamma$ -rays emitted per unit time by the standard after irradiation.

### Prompt and Delayed NAA

The most important distinction, as far as NAA is concerned, is between Prompt and Delayed Gamma Neutron Activation Analysis. PGNAA is based on the detection of the promptly emitted  $\gamma$ -rays, so the measurement is performed during the irradiation, while in DGNAA only the delayed emitted  $\gamma$ -photons are measured. Of course this second variant requires a certain waiting time before the measurement can be done.

PGNAA is mainly applied to detect nuclides with very high neutron capture cross section, elements which decay too rapidly to be detected when irradiation is over or elements which do not produce radionuclides after neutron capture.

DGNAA is more widely used than PGNAA because the waiting time before the measurement can be adapted in order to increase the sensitivity to long-lived radionuclides which suffer from interference by a short-lived one. This possibility makes DGNAA a very selective analytical technique.

### Neutron sources

The major neutron sources employed to perform NAA are:

- **Nuclear Reactors**, in which neutrons are produced during fission and the neutron flux is of the order of  $10^{12} \div 10^{15} \frac{\text{part}}{\text{cm}^2\text{s}}$ . Here neutrons are thermal, epithermal and fast, so they require thermalization before they can be used in NAA.
- $^{252}\text{Cf}$  has a half-life of 2.6 years (96 % for  $\alpha$ -decay and 4 % for fission), it produces 3.76 neutrons per event with an energy of 1.5 MeV. As the result, 1 mg of  $^{252}\text{Cf}$  can emit  $2.3 \times 10^9 \frac{\text{part}}{\text{s}}$ .
- **Fusion Type Neutron Generators** are machines capable of generating neutrons with energies up to 14 MeV, using (D,T) or (D,D) reactions. The

yield for these sources is of the order of  $10^{12} \frac{\text{part}}{\text{s}}$ .

- **Particle accelerators** can be used in order to generate neutrons through the acceleration of charged particles and the subsequent interaction with suitable targets. In this way reactions such as  ${}^2\text{H}(d, n){}^3\text{He}$ ,  ${}^3\text{H}(d, n){}^4\text{He}$ ,  ${}^7\text{Li}(p, n){}^7\text{Be}$  and  ${}^9\text{Be}(d, n){}^{10}\text{B}$  can take place, generating neutron fluxes of the order of  $10^9 \frac{\text{part}}{\text{cm}^2\text{s}}$ .

### Main features of NAA

NAA has the advantage of being free of any matrix interference because the main matrix elements (H, C, O, N etc.) do not produce radioisotopes under neutron irradiation, so it is suitable for searching trace elements. It is also a non-destructive technique, it requires only a small amount of sample, it allows to identify many elements simultaneously and to make the measurements at different times in order to increase the selectivity.

Due to the possible presence of many overlaps in the spectrum, NAA often requires to wait some time after the irradiation before making the measurement. This waiting time can be of several days or weeks, so in case of a long-lived radionuclide, NAA can take long time to complete a full analysis.

## 1.2 Ion acceleration systems

### 1.2.1 Introduction to conventional accelerators

Particle accelerators are devices that produce a beam of energetic ions. Van de Graaff is credited with inventing the first accelerator. In 1931, he invented the first prototype of an electrostatic generator [43]. This model was able to produce protons with energy up to 5 MeV. Subsequently, the so-called tandem version [44] was created allowing to double the energy up to 10 MeV. At the same time, in the 1930s, Lawrence put forward the proposal of a scheme for the realization of a circular accelerator, the cyclotron [45], which was able to generate a high energy, monoenergetic proton beam. A strong boost in the field of particle acceleration occurred in the 1940s, with the invention of the synchrotron [46] to accelerate electrons. During the second half of the 20th century, the rise in supplied particle energies with these machines grew steadily till it reached its technical and financial limits.

Nowadays, particles accelerators are employed worldwide in many applications such as nuclear physics research, radioisotope production, radiation therapy, sterilization of biological materials and, of course, Ion Beam Analysis. Despite the variety of configurations available, there are some aspects in common between the various technologies:

- **Source of electrically charged particles**

The principal source of protons for a particle accelerator is a hydrogen gas

that is ionized: electrons and protons are separated in an electric field and the second ones are passed through a hole. In large particle accelerators, protons are generally provided as negative hydrogen ions, which form when the initial molecular gas is ionized. The electrons in excess are stripped through the passage in a thin foil before the last acceleration stage.

- **Accelerating electric field**

One of the key features of an accelerator is the presence of an electric field for the acceleration of charged particles. In the simplest case, this is a constant static field between negative and positive potentials. The difference in the potential determines the energy gain of a particle accelerated inside. The energy acquired by an elementary charge moving in a potential of 1 volt takes the name of electron volt (eV) and it is equal to  $1.6 \times 10^{-19}$  J.

An example of an accelerator that uses a constant electric field, usually equal to millions of volts, is the generator of Van de Graaff. An alternative to the presence of such strong, and therefore difficult to manage, fields is the repetitive use of weaker electrical fields. For example, in LINACs (linear accelerators), particles are passed through a series of weaker fields. Another solution is the passage for many times in the same field as in the case of cyclical accelerators (cyclotrons and synchrotrons).

A repetitive structure suggests the use of an alternating voltage to create the electric field: a positive charge accelerated to a negative potential receives a renewed boost if at its passage the potential becomes positive. However, given the high velocity of the ions, it is necessary that the potential varies with a frequency of millions of cycles per second (MHz). In fact, this is achieved by employing the alternating electric field present in an electromagnetic wave in the spectrum of radio waves (100 MHz) or microwaves (3000 MHz).

- **Magnetic fields to control the direction of the charged particles**

Magnetic fields are used to control the direction of the particle beam. In the simplest case, by the effect of Lorentz's force, a particle moving at right angles in the direction of a uniform magnetic field feels a force in the orthogonal direction to the field and to the motion. The particle will follow a circular trajectory in this plane.

In cyclotrons, a uniform static magnetic field is used to obtain a spiral motion in the outward direction while the protons are accelerated by an electric field. In the synchrotron, particles are accelerated along a constant radial circle path where the field increases along the ring. Magnetic fields are also used to focus the beam through the use of quadrupole pairs.

In this chapter it is not intended to treat all kinds of particle accelerators in detail, but to give some information about the configurations used to perform IBA, in particular Van de Graaff generators and cyclotrons.

## 1.2.2 Van de Graaff generators and two stage tandem accelerators

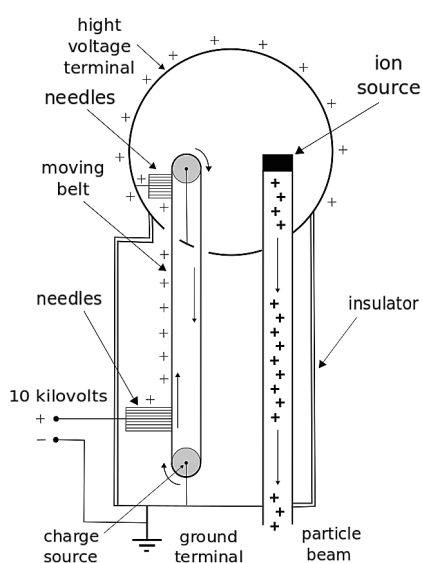


**Figure 1.12:** Van de Graaff generator scheme.

In the Van de Graaff generators, the electrical charge required to form the constant electric field is carried by a belt of insulating material moved by two pulleys: one is placed in correspondence of the ground terminal and the other is inside a spherical high voltage terminal. Near the ground pulley, the belt is loaded with positive charges by needles. These needles are alimented by a power supply that brings them to a potential of tens of kilovolts.

The gas in contact with the needles is ionized and the ions are collected on the belt which carries the charges to the high voltage terminal. In the high-voltage terminal of the pulley there are other needles that collect the charges and carry them to the outer surface of the terminal. The scheme is shown in fig. 1.12.

In this way, it is possible to generate a potential up to 20 megavolts between the

two terminals, which can accelerate the positive ions produced by a source placed on the positively-charged terminal.

Van de Graaff generators are often used as the main acceleration stage in two-stage tandem accelerators. This system is able to provide protons with twice the energy with respect to the single-stage configuration already described.

In tandem accelerators, a source provides protons that are accelerated at low energies by an auxiliary voltage supply, then they pass through a low pressure gas in which they are partially converted into negative ions. Through the passage in a magnetic field the carriers are separated and the negative ion beam is accelerated towards the positive high voltage terminal of a Van de Graaff generator (first acceleration stage). At the end of the terminal, the beam crosses a carbon foil that strips electrons and converts negative ions into protons. These are then accelerated on the other side of the same high voltage terminal (second acceleration stage).

### 1.2.3 Cyclotrons

The key aspect in the operation of a cyclotron is the isochronicity of the ion orbit in the uniform magnetic field: the time required for a particle with a certain mass to complete a circular trajectory is equal for any velocity as long as it is much less than the speed of light. This makes it possible to accelerate a particle for many times thanks to a high voltage, reversed in polarity and at constant frequency.

The scheme of a cyclotron is shown in fig. 1.13: an ion source is placed in the center of a cylindrical vacuum chamber with a constant and uniform magnetic field oriented orthogonal to the faces. The acceleration voltage is generated by two electrodes (dees) and it is characterized by an oscillation frequency equal to that of the particles' revolution in the magnetic field. The electric field related to the accelerating potential is concentrated in the gap between the dees, while it is not present inside them. So, the path of the particles will be circular in the dees where there is no acceleration because the potential is constant, while each time the beam passes inside the gap it will be accelerated by the presence of the potential difference.

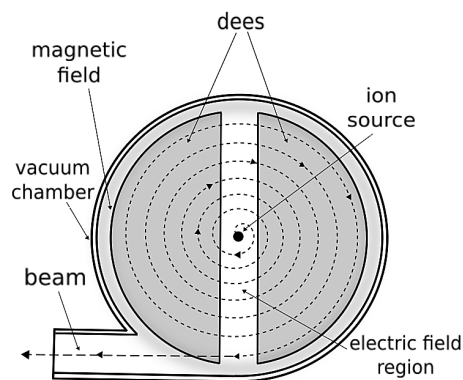


**Figure 1.13:** *Cyclotron accelerator scheme.*

The particles cross the gap twice per revolution and, since the voltage frequency is the same as that of the circular motion, the acceleration potential is alternatively inverted. Thanks to this synchronism the particles undergo two accelerations for each revolution they make and their trajectory will result in a spiral extending from the center of the cylinder.

It is emphasized that the energy that can be supplied to the particles is limited by the relativistic increase in mass while velocity rises, which causes a reduction in the orbital frequency and leads to an asynchronism between the particle motion and the voltage oscillation. This effect can be mitigated by applying a higher voltage and reducing the overall acceleration time. In any case, the maximum energy available is less than 25 MeV, even applying hundreds of kilovolts to the dees.

It is emphasized that the energy that can be supplied to the particles is limited by the relativistic increase in mass while velocity rises, which causes a reduction in the orbital frequency and leads to an asynchronism between the particle motion and the voltage oscillation. This effect can be mitigated by applying a higher voltage and reducing the overall acceleration time. In any case, the maximum energy available is less than 25 MeV, even applying hundreds of kilovolts to the dees.

## 1.3 Proton acceleration driven by superintense laser pulses

Nowadays, ion acceleration driven by superintense laser pulses is one of the most promising areas in the development of alternative systems to particle accelera-

tors.

When a laser pulse hits a plasma, very intense electric fields can be generated, leading to the formation of acceleration gradients of the order of  $10^5 \div 10^6$  MeV/m, compared to 10-100 MeV/m in accelerators. This opens up the possibility of building a laser-based experimental apparatus for particle acceleration that is more compact and less expensive than conventional particle accelerators. The provided ion beams are characterized by short duration (initially comparable with the laser pulse duration), small divergence angle (in the order of some degrees), high laminarity of the flux and large number of ions accelerated (up to  $10^{13}$  part/MeV). These interesting properties have suggested numerous applications [47], including proton radiotherapy, production of warm dense matter, fast ignition, hadron therapy, nuclear and particle physics research.

The continuous increase in the intensity of lasers revealed different interaction regimes (e.g. TNSA, plasma expansion, dipole vortex acceleration, radiation pressure, coulomb explosion, etc.). Whether a particular type of interaction occurs depends primarily on the properties of the laser pulse (intensity and duration) and on the characteristics of the target.

Given the complexity of the physical phenomena involved, it is not possible to consider the whole process as described by a single acceleration scheme, but it is only possible to identify which one of these can be considered dominant.

As regards the work performed in this thesis, the most significant interaction regime is Target Normal Sheath Acceleration (TNSA), qualitatively described in this section.

### 1.3.1 Basics of interaction of laser pulses with overdense targets

Consider a linearly polarized laser pulse with an intensity  $I$  higher than  $10^{18}$  W/cm<sup>2</sup> and a "dimensionless" amplitude  $a_0$ <sup>1</sup> greater than 1.

When the pulse is made to impinge on a solid target a rapid ionization on the front side is observed due to the action of the prepulse. There is therefore the formation of a plasma that begins to expand in the opposite direction with respect to the laser propagation one. If the electronic density of the plasma  $n_e$  is equal to or less than the critical one  $n_c$  (i.e. the density for which the plasma and laser frequency are equivalent), the refractive index of the plasma  $n$  becomes real and the laser pulse is partially absorbed into the plasma itself:

$$n = \left(1 - \frac{n_e}{n_c}\right)^{1/2} \longrightarrow \text{condition for transparency: } n_e \leq n_c \quad (1.18)$$

Considering the presence of relativistic effects, the refractive index becomes non-linear and the condition for transparency also changes (relativistic self-induced

---

<sup>1</sup>Parameter related to the intensity  $I$  and equal to  $a_0 = 0.85 \frac{I \lambda^2}{10^{18} \text{Wcm}^2}$  where  $\lambda$  is the wavelength of the laser expressed in  $\mu\text{m}$ , as reported in [47].

transparency):

$$n_{nl} = \left(1 - \frac{n_e}{\gamma n_c}\right)^{1/2} \longrightarrow \text{condition for transparency: } n_e \leq \gamma n_c \quad (1.19)$$

$$\gamma = \sqrt{1 + a_0^2/2} \quad (1.20)$$

For the laser parameters reported above there are many phenomena responsible for the absorption of the laser pulse:

- **Ponderomotive force:** It is the effective force describing the motion of a charged particle in an oscillating non-uniform field, averaged over the oscillations and acting as the result of radiation pressure effects:

$$\mathbf{f}_p = -mc^2 \nabla (1 + \langle \mathbf{a} \rangle^2)^{1/2} \quad \mathbf{a} = \frac{e\mathbf{A}}{mc^2} \quad (1.21)$$

In eq. 1.21,  $\mathbf{A}$  is the vector potential,  $e$  is the electron charge,  $m$  is the electron mass and  $c$  is the light speed. This force acts more effectively on the electrons and pushes them inside the plasma leading to charge separation. As a result the electron density decreases and, combined with the relativistic effects, it promotes the transition to transparency reducing  $n_e$ .

- **Vacuum heating:** in presence of a steep plasma density gradient, P-polarization (the laser electric field vector lies in the incidence plane) and oblique incidence, the combined effect of the electric field of the laser pulse and the reflected field attracts the electrons toward the laser source and, after a half oscillation, they are injected inside the target with high energy. This process was first discussed by Brunel and so it is also called Brunel effect.
- **$\mathbf{j} \times \mathbf{B}$  heating:** in case of S-polarization, or possibly normal incidence, there is no orthogonal electric field to the surface, but electron oscillation along the density gradient can still be driven by the magnetic component of the field. The origin of this mechanism lies in the  $\mathbf{v} \times \mathbf{B}$  component of the Lorentz force and, at normal incidence, can be treated as a sort of vacuum heating. The only differences are that the electromagnetic force oscillates at a doubled frequency, so the same applies to the generation of the electron bunches, and the oscillations vanishes for circular polarization. Moreover, the influence of this phenomenon becomes important for  $I \gg 10^{18} \text{W/cm}^2$ .
- **Resonant absorption regime:** in case of P-polarization, the component of the field directed along the density gradient of the plasma excites an electron plasma wave, which accelerates electrons in the opposite direction with respect to the laser pulse propagation way.

Therefore, because of the aforementioned processes, there is the formation of a plasma on the front side of the target and the acceleration of the hot electrons toward the rear side.

### 1.3.2 Sheath field formation at the rear side and ion acceleration

The heating process generates high-energetic electrons that are pushed inside the target. These electrons flowing to the back side should be counterbalanced by a return current to the opposite face resulting in a net current equal to zero. In fact, the limited conductivity of a cold solid target strongly reduces the return current. This would result in an unbalance of charge that would induce an electric field that could inhibit the flow of warm electrons, which would travel for a shorter distance with respect to the mean free path inside the material. To overcome this effect, a target thin enough to ensure that a portion of the electrons from the rear side of the target would be released is chosen. On the rear side of the target, a cloud of electrons emerges in the vacuum and a consequent electric field due to the unbalance of the charge is formed.

The electric field immediately ionizes the atoms on the surface, which are

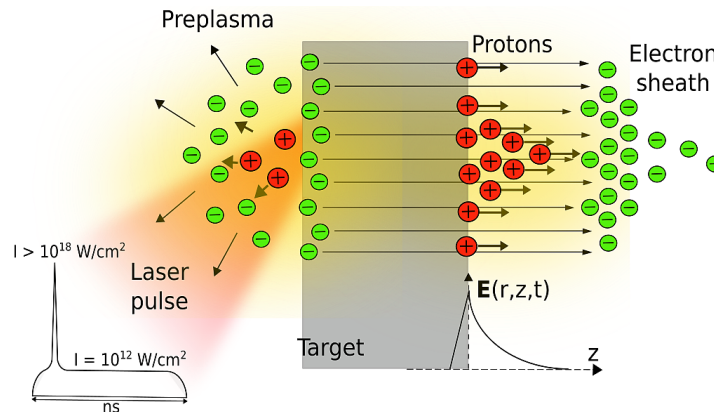


**Figure 1.14:** TNSA scheme.

stripped and accelerated. An electron and ion plasma is then generated and begins to expand towards the vacuum in the orthogonal direction to the target, until it reaches the energy of tens of MeVs per nucleon. This process is called Target Normal Sheath acceleration (TNSA) and it is schematically reported in fig. 1.14.

The sheath field is mainly responsible for the acceleration that vanishes on a length scale of few micrometers inside the target, so only a small thickness on the rear target side is ionized. The ions coming from this layer constitute the highest part of the energy spectrum. By proceeding with the expansion, a rarefaction wave is formed and it propagates into the target reaching the front



side. This field is strong enough to ionize other layers and to accelerate the ions, which will constitute the low energetic part of the spectrum.

As a final result, a bunch of ions is emitted from the target, characterized by an exponential energy spectrum with a well-defined cut-off energy, as it is reported in fig. 1.15 for different laser facilities. You can appreciate how the number of protons can vary between  $10^9$  and  $10^{12}$  part/MeV/str.

Another interesting parameter is the maximum proton energy. It is shown in fig. 1.16, considering again different laser facilities, as a function of the laser irradiance  $I\lambda^2$  and for different laser pulse duration. As reported in [47], two possible proton energy scaling can be suggested:  $\sim (I\lambda^2)^{1/2}$  and  $\sim I\lambda^2$ .

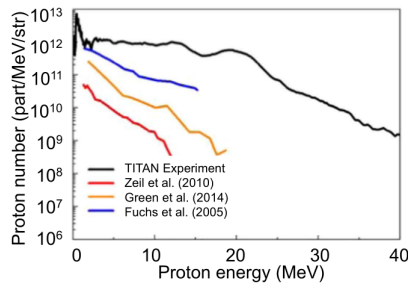


**Figure 1.15:** Four proton energy spectra from different laser facilities (reproduced from [1]).

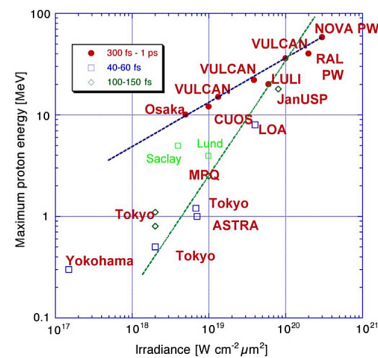


**Figure 1.16:** Maximum proton energy as a function of the irradiance for three possible ranges of laser pulse duration (reproduced from [47]).

## Chapter 2

# PIXE and PIGE Spectroscopy

In this Chapter, two techniques are described in detail, as they are the subject of study of this thesis work: Particle Induced X-ray Emission and Particle Induced Gamma-ray Emission.

In particular, Sec. 2.1 treats in detail the PIXE experimental configuration and the detectors employed to run it. After that, the formalism necessary to describe theoretically PIXE will be presented in Sec. 2.2, focusing on the various versions of this technique.

As far as PIGE is concerned, the main interactions between  $\gamma$ -rays and matter and the available detectors will be described in Sec. 2.3. This part deals also with the theoretical model used to describe PIGE, which is very similar to that of PIXE analysis.

Sec. 2.5 is devoted to highlight the disadvantages of conventional PIXE and PIGE and to suggest a possible alternative for the primary particle generator: a laser-driven protons source. The innovations involving this choice and the way to study its feasibility will be discussed. Then, the goals of the thesis will be presented.

### 2.1 Experimental apparatus for PIXE

The experimental apparatus typically employed to perform PIXE involves a particle accelerator (generally Van de Graaff generators or cyclotrons), a scattering chamber and a detection system. In some cases the measurement are done also in-air and in this case no scattering chamber is used. Having already discussed the aforementioned accelerator systems in Sec. 1.2, only the scattering chamber and the detectors will be described here.

#### 2.1.1 Scattering chamber

An example of scattering chamber (or vacuum chamber) is shown in fig. 2.1. The sample is placed in its center. On the walls there are several ports [5]). Two

of these are dedicated to the proton beam: on one side the beam is injected into the chamber and it strikes the target, generally oriented at  $45^\circ$ , while on the opposite side there is a Faraday cup.

The ion beam entrance window is equipped with a gate valve, whose function is to separate the vacuum in the beam line and in the scattering chamber. There is also a collimator for the particle beam. If the sample is thin enough it can be crossed by the ion beam, which in this case is collected by the Faraday cup, which provides a measurement of the ion beam current.

Generally, in order to retrieve information about the primary particle current, a surface barrier detector is placed at  $45^\circ$  with respect to the beam. This detector provides information on energy of the backscattered projectiles.

In order to detect the X-rays, a suitable detector (e.g. Si(Li)) is placed at  $90^\circ$  with respect to the beam direction.

Samples are placed on a rotating target holder, which can be handled from the outside in order to perform multiple analysis without venting the vacuum chamber.

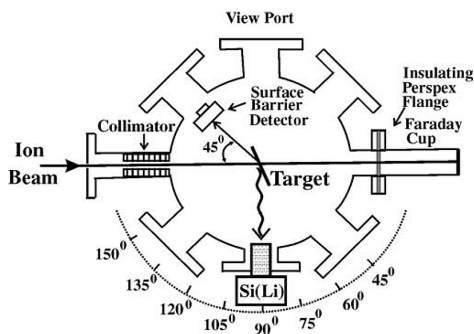


**Figure 2.1:** *Scattering chamber scheme (reproduced from [5]).*

### 2.1.2 In-air PIXE

In an external beam system the primary particle beam is brought into the atmosphere through a thin foil separating the vacuum inside the particle accelerator and the air. This experimental configuration allows to analyze volatile materials and samples which can not be inserted inside the vacuum chamber (e.g. paintings or large archaeological artifacts).

An advantage of the in-air measurements is the effective heat dissipation from the sample surface, which allows for a safer analysis. On the other hand, the presence of the atmosphere causes the beam to be no longer exactly monoenergetic when it strikes the sample, because of the energy straggling. The appearance of the characteristic peak of Ar at 3 keV in the X-ray spectrum is another effect.

### 2.1.3 Detection system

The X-ray energy dispersive detection system generally employed to perform PIXE includes a Si(Li) detector, a pre-amplifier, an amplifier, an analog to dig-

ital converter (ADC) and a multichannel analyzer (MCA).

Si(Li) semiconductor detectors are “energy dispersive” because they sort the X-rays on the basis of their energy. In particular, when a photon of energy  $E$  is absorbed in the active medium, the total charge  $Q$  associated to the (e-h) pairs formed is:

$$Q = \frac{E [\text{keV}]}{3.81} \times 1.6 \times 10^{-16} \text{ Coulomb} \quad (2.1)$$

where 3.81 eV is the energy taken from the X-ray necessary to ionize Si once at a temperature of 77 K. The charge  $Q$ , which will be integrated in a current pulse, is proportional to the energy  $E$ . The intrinsic resolution of Si(Li) detectors can be expressed in terms of full width at the half maximum (FWHM) [5]:

$$\text{FWHM} = 2.35(2.81 \frac{\text{eV}}{\text{e-h pair}} \times F \times E_x)^{1/2} \quad (2.2)$$

where  $F = 0.12$  is the Fano factor and  $E_x$  is the X-ray energy. This reaction gives an energy resolution of 110 eV at  $E_x = 5 \text{ keV}$ .

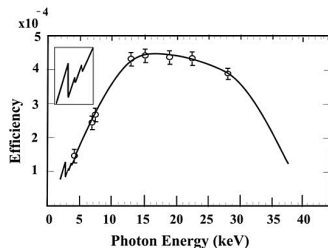


**Figure 2.3:** Absolute Si(Li) detector efficiency (reproduced from [5]).

Overall, the efficiency is a function of the X-ray energy because the absorption coefficients  $\mu(E_x)$  of the detector materials are energy-dependent. Considering also the solid angle subtended by the detector, an example of absolute efficiency as a function of energy can be found in fig. 2.3. The detail shows the effect of the K-absorption edge of Si in the dead layer.

#### 2.1.4 PIXE with heavy ions

Protons are not the only projectiles used in PIXE. When heavier ions are employed, the first observed effect is an increase in the complexity of the spectrum. This is due to the fact that the projectiles have a greater charge and mass, and they interact strongly with the target. In addition, the ions have their own

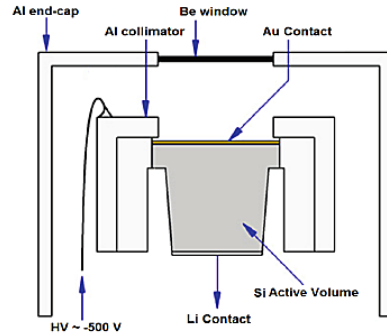


**Figure 2.2:** Scheme of Si(Li) detector (reproduced from [48]).

atomic structure that can produce multiple ionizations. Overall, a line broadening and a shifting of the peaks in the spectrum is observed.

The advantage of using heavier ions is found for  $Z_1 < 6$  (where  $Z_1$  is the projectile atomic number), for which the ionization cross section scales as  $Z_1^2$  with respect to the same quantity for protons. Therefore, there is a consequent increase in the X-ray yield and in the analytical capability. This dependence is lost for  $Z_1 > 6$  for which the cross section becomes so small that it does not produce appreciable yields.

Conversely, the main disadvantages of employing heavy ions are the destructive effect on the target and greater complexity in the interpretation of the spectrum, also favored by the possible presence of the X-rays of the projectiles and of the quasimolecules that can be formed when  $Z_1 \sim Z_2$ .

### 2.1.5 Fluorescence and yield enhancement effects

When elements with very similar atomic number  $Z$  are present in the sample, the x-rays emitted by the larger  $Z$ -element can induce fluorescence on the smaller  $Z$ -element. This contribution to the measured yield is said to be “secondary”, with respect to the direct ionization contribution due to projectiles, which is said to be “primary” (see fig. 2.4).

In [49] an analytical relationship between primary and secondary yields for  $K\alpha$  transitions is derived, as well as an approximated expression useful to make estimation (eq. 2.3). Here, for reasons of brevity, only the second one is reported:

$$\frac{Y_{K\alpha,A,SEC}}{Y_{K\alpha,A,PR}} = \frac{1}{2} \frac{r_A - 1}{r_A} \frac{M_A}{M_B} \omega_{K,B} \frac{\mu_{K\alpha,B,A}}{\mu_{K\alpha,B,samp}} \frac{\sigma_{K\alpha,B}(E_0)}{\sigma_{K\alpha,A}(E_0)} W_B \quad (2.3)$$

In eq. 2.3,  $r_A$  is the ratio of the mass absorption coefficients of the exciting primary X-rays emitted by element  $B$  in the excited element  $A$  before and after its absorption edge,  $M_A$  and  $M_B$  are the atomic masses of the secondary emitter and of the primary one,  $\omega_{K,B}$  is the fluorescence yield of the primary X-rays,  $\mu_{K\alpha,B,A}$  and  $\mu_{K\alpha,B,samp}$  are the primary X-ray absorption coefficients in the secondary emitter element and in the sample,  $\sigma_{K\alpha,B}(E_0)$  and  $\sigma_{K\alpha,A}(E_0)$  are the ionization cross sections and  $W_B$  is the mass concentration of the primary emitter.

In table 2.1 there are some values reproduced from [49] for the ratio between primary and secondary yields in the case of Fe ( $A$ ) and Ni ( $B$ ), for different concentration of the excited element and for proton energies of 2 MeV. Both the correct and approximated values are reported. It is evident that the secondary fluorescence

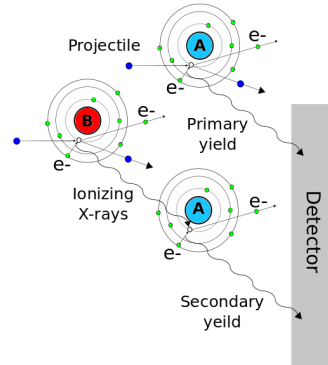


**Figure 2.4:** *Enhancement effect scheme.*

**Table 2.1:** Ratio of secondary over primary yield for Fe and Ni (values from [49]).

$W_{Fe}$ (wt %)	$\left(\frac{Y_{K\alpha,Fe,SEC}}{Y_{K\alpha,Fe,PR}}\right)_{exact}$	$\left(\frac{Y_{K\alpha,Fe,SEC}}{Y_{K\alpha,Fe,PR}}\right)_{approx}$
1	0.54	0.54
5	0.46	0.43
20	0.28	0.22
40	0.16	0.11
80	0.034	0.021

contribution becomes more important as the concentration of the exciter element increases with respect to the secondary emitter one. The same applies also for the accuracy of the approximated relation.

### 2.1.6 Sources of background

In PIXE analysis, the X-ray spectrum can be affected by the presence of a continuous background superimposed to the characteristic X-ray lines. The causes of background can be of different nature:

#### 1. Contributions from the particle source:

- *Compton scattering* of  $\gamma$ -rays produced by nuclear states excited during the irradiation.  $\gamma$ -photons leave the target and undergo Compton scattering inside the detector volume, where only the fraction of energy retained by the electrons is released (for more information about Compton effect, see Sec. 2.3.1). This process is responsible for the high-energy part of the background.
- *Projectile Bremsstrahlung* consists in the emission of electromagnetic radiation during the slowdown of the projectiles inside the sample (this is a minor contribution).
- *Secondary electron Bremsstrahlung* is the main cause of the low-energy part of the background and it is due to the slowdown of the electrons ejected from the atoms of the sample during irradiation.

2. **Contributions from geometry:** the chamber and holder materials can be responsible for the presence of contaminant lines and background in the spectrum, in particular in the case of very thin targets. This is because of the fact that the X-ray yields from the sample itself are very low.

#### 3. Detection system:

- The main contribution is due to the *incomplete collection of the charges* in the Si(Li) detector sensitive volume. This can be due

to the recombination of the electrons and holes before they are collected.

- *Au lines* can be present in the spectrum because the gold detector contacts are irradiated by the X-rays coming from the sample and secondary fluorescence can be induced. The intensity of these lines (K and L) depends upon the thickness of the gold contacts.

## 2.2 Theoretical description of PIXE

The objective of PIXE is to perform a surface analysis of samples whose elemental composition is unknown. As explained in Sec. 1.1.2, the elements in the target are recognized by the energy of the characteristic peaks in the spectrum. The quantitative analysis is performed considering the intensity of the lines and applying procedures based on theoretical models, which are specific for each kind of sample.

Taking into account the various types of samples which can be studied, a first crucial distinction is between homogeneous and non-homogeneous targets. In the first case, the elements are characterized by the same unknown concentrations along the sample thickness, so the goal of the analysis is simply to evaluate their values. In the second case, in the case of non-homogeneous targets, the elemental concentrations are not constant along the sample thickness. For example, a multilayer structure in which the compositions of each layer is known a priori can be considered. In this case, the unknowns are the layer thicknesses.

Finally, the target structure can be completely generic and unknown. Here, the elemental concentration distributions as a function of the sample depth can be derived employing a PIXE variant known as *Differential PIXE*.

Another distinction is between thin targets, for which the composition is always considered as homogeneous, and thick targets. As it will be shown, this splitting implies some fundamental differences in PIXE modeling for the two cases.

It is stressed that all the quantities which appear in the following models can be retrieved from the databases reported in Sec. C.0.2.

### 2.2.1 Thin targets

In the case of thin samples (fig. 2.5), the goal of the analysis is to determine the mass concentrations for the elements. Considering a small target thickness  $t$ , the projectile range inside the material is large compared with the linear thickness of the target. The position dependency of the self-absorption of the secondary

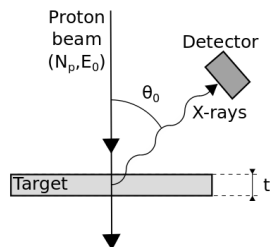


**Figure 2.5:** Scheme of PIXE analysis with thin targets.

radiation can be neglected and the ionization cross section can be considered constant, equal to the value associated to the proton initial energy  $E_0$ . This allows to strongly simplify the theoretical model.

As reported in [5] the X-ray yield in the case of thin targets  $Y_j$  can be expressed as the products of different terms:

- the number of protons incident on the sample  $N_p$ ;
- the fraction of solid angle subtended by the detector  $\Delta\Omega/4\pi$ ;
- the intrinsic detector efficiency  $\varepsilon_j$  for the characteristic X-ray energy;
- the Avogadro number  $N_{av}$ ;
- the sample density  $\rho_{comp}$ ;
- the atomic weight  $M_j$  of the element;
- the mass concentration  $W_j$  of the element of atomic number  $Z$  emitting the X-ray;
- the ionization cross section  $\sigma_j$  of the transition associated with the  $j$ -th emission;
- the fluorescence yield  $\omega_j$ .
- the effective thickness  $t'_j$ ;

The index  $j$  refers to the X-ray line or, equivalently, to the emitting element.

$$\frac{Y_j}{N_p} = \frac{\Delta\Omega}{4\pi} \varepsilon_j W_j \frac{N_{av}}{M_j} \rho_{comp} t'_j \sigma_j(E_0) \omega_j \quad (2.4)$$

In eq. 2.4 the effective thickness  $t'_j$  is evaluated from the real thickness  $t$ , the mass attenuation coefficient for the  $j$ -th X-ray in the compound  $(\mu/\rho)_j$  and the angle of the emitted X-rays with respect to the normal to the target  $\theta_0$ :

$$t'_j = t \cdot e^{-\left(\frac{\mu}{\rho}\right)_j \frac{t \sec \theta_0}{2}} \quad (2.5)$$

Relation 2.4 can also be written in this way:

$$Y_j = N_p \frac{\Delta\Omega}{4\pi} \varepsilon_j (n_j t'_j) \sigma_j(E_0) \quad (2.6)$$

Where  $n_j = W_j \rho_{comp} N_{av} / M_j$  is the element number density and  $\sigma_j(E_0) = \omega_j \sigma_j(E_0)$  is the X-ray production cross-section.

Neglecting the proton slowdown inside the material, the ionization cross section is evaluated only at the projectile initial energy  $E_0$ , while the X-ray attenuation is simply accounted considering the effective thickness  $t'$  instead of the real one



*t.*

Generally, the photon energies associated to the mass attenuation coefficients do not necessarily coincide with the characteristics X-ray energies required in the analysis. In this case, the interpolated value at a specific energy  $E_j$  between  $E_1$  and  $E_2$  can be calculated using the relation:

$$\left(\frac{\mu}{\rho}\right)_{i,j} = \left(\frac{\mu}{\rho}\right)_i(E_2) \times (E_j/E_2)^\eta \quad (2.7)$$

$$\eta = \frac{\log\left(\left(\frac{\mu}{\rho}\right)_i(E_1)\right) - \log\left(\left(\frac{\mu}{\rho}\right)_i(E_2)\right)}{\log(E_1) - \log(E_2)} \quad (2.8)$$

Finally, the mass attenuation coefficient in the compound, evaluated for the  $j$ -th X-ray energy  $(\mu/\rho)_j$ , is given by [5]:

$$\left(\frac{\mu}{\rho}\right)_j = \sum_{i=1}^J \left(\frac{\mu}{\rho}\right)_{j,i} \times W_i \quad (2.9)$$

where  $(\mu/\rho)_{j,i}$  and  $W_i$  are the mass attenuation coefficients and mass concentration for the  $i$ -th element present in the sample and  $J$  is the total number of elements.

The set of equations described above allows to relate the X-ray yields  $Y_j$  with the thin sample composition  $W_j$ . Once the number of detected X-rays  $Y_{j,exp}$  is measured experimentally, it is possible to write a system of eq. 2.4, one equation for each element, where the only unknowns are  $W_j$ . Of course, the elemental concentrations also enters in eq. 2.5 because the X-rays attenuation depends on the material composition. So the solution of the system has to be found with an iterative procedure by searching the minimum of a parameter like:

$$\chi = \left( \sum_{j=1}^M \left( \frac{Y_{j,exp}}{\langle Y_{j,exp} \rangle_{max}} - \frac{Y_{j,th}}{\langle Y_{j,th} \rangle_{max}} \right)^2 \right)^{1/2} \quad (2.10)$$

where  $Y_{j,th}$  are the calculated X-ray yields for each element,  $\langle Y_{j,th} \rangle_{max}$  and  $\langle Y_{j,exp} \rangle_{max}$  are the maximum ones among  $Y_{j,th}$  and  $Y_{j,exp}$ . Considering the iterative procedure, in eq. 2.10, the yields are normalized with respect to maximum values because in this way the incident number of protons  $N_p$  and the detector solid angle  $\Delta\Omega$  cancel out. The mass concentrations  $W_j$  are also constrained between 0 and 1.

### 2.2.2 Thick homogeneous target

Consider now the case of a thick homogeneous target. Here again, the goal of the analysis is to retrieve the sample elemental composition in terms of the mass concentrations of the elements.

If the sample is thick, the projectiles lose all their energy, or at least a non negligible part, traveling inside the material. So, the formalism has to take into account also the stopping power of the protons and the consequent variation of the ionization cross section. Moreover, the attenuation of the X-rays changes as a function of the depth inside the material and a simple “mean” effective thickness can no longer be considered. The equation for the X-ray yield  $Y_j$  of the  $j$ -th element must take into account all the aforementioned effects.

With reference to fig. 2.6, it is possible to express the number of x-rays generated in the infinitesimal mass thickness  $\rho dr$  for the  $j$ -th element as follows:

$$dY_j = N_p W_j \frac{N_{av}}{M_j} \sigma_j(\rho r) \omega_j d(\rho r) \quad (2.11)$$

Considering the contribution of a finite layer, the attenuation and the presence of the detector, the number of photons emerging from the sample and recorded  $Y_j$  is:

$$Y_j = N_p \frac{\Delta\Omega}{4\pi} \varepsilon_j W_j \frac{N_{av}}{M_j} \int_0^{\rho R} \sigma_j(\rho r) \omega_j \exp^{-\left(\frac{\mu}{\rho}\right)_j \frac{\rho r}{\cos\theta}} d(\rho r) \quad (2.12)$$

where again the index  $j$  refers to the  $j$ -th element. The quantities present in the integral are the X-ray ionization cross section  $\sigma_j$  expressed as a function of the mass thickness  $\rho r$ , the fluorescence yield  $w_j$  and an exponential term which takes into account the X-ray attenuation, both integrated across the entire mass range  $\rho R$ . All the other terms have already been defined in Sec. 2.2.1.

In the exponential term,  $\left(\frac{\mu}{\rho}\right)_j$  is the mass attenuation coefficient for the characteristic X-rays of the  $j$ -th element in the sample and it is evaluated as described in the case of a thin sample (eq. 2.9).

The distance a particle travels inside a material is connected to its energy through the linear stopping power  $\rho S(E) = -\frac{dE}{dr}$ . So the path as a function of the energy  $\rho r(E)$  can be evaluated from:

$$\rho r(E) = \int_{E_0}^E \frac{dE'}{S(E')} \quad (2.13)$$

In eq. 2.13,  $S(E)$  is the projectile mass stopping power in the sample, which is given by the mass stopping powers of the single elements  $S_i$  and the mass concentrations  $W_j$  combined with the additive rule:

$$S(E) = \sum_{j=1}^J W_j S_j(E) \quad (2.14)$$

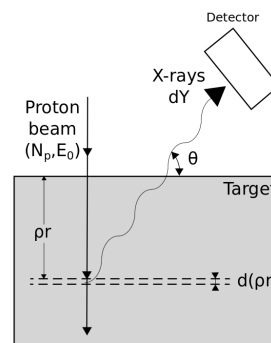


**Figure 2.6:** Scheme of PIXE analysis with thick targets.

where  $J$  is the total number of elements.

It is worth to mention that the dependency on the sample composition appears not only in the X-ray attenuation coefficients (eq. 2.9), but also in the stopping power for the projectiles (eq. 2.14). This is quite obvious because the energy loss of primary particles must depend upon the medium composition.

Finally, an iterative procedure analogous to the one described in Sec. 2.2.1 can be applied in order to retrieve the sample composition from the experimental yield. Once the particle path as a function of energy  $\rho r(E)$  has been evaluated for a certain set of concentrations  $W_j$ , it can be inverted in order to find  $E(\rho r)$ , which in turn can be substituted inside  $\sigma_j(E)$ . This procedure allows to find the cross section as a function of path  $\sigma_j(\rho r)$  and the integral in eq. 2.12 can be evaluated.

Eventually, also the secondary X-ray production yield can be taken into account, applying the equation reported in [49].

### 2.2.3 Multilayer targets

It is assumed that the sample is made of  $L$  different homogeneous layers of known elemental concentrations, as shown in fig. 2.7, and the goal is to obtain their thicknesses. Such kind of analysis was first proposed in [50].

Assuming that a certain element can be present in different layers, the expression for the X-ray yield  $Y_j$  associated to that element can be written as:

$$Y_j = N_p \frac{\Delta\Omega}{4\pi} \varepsilon_j \frac{N_{av}}{M_j} \sum_{l=1}^{L-1} W_{j,l} P_{j,l} \int_{\rho R_l}^{\rho R_{l+1}} \sigma_j(\rho r) \omega_j e^{-\left(\frac{\mu}{\rho}\right)_{j,l} \frac{\rho r}{\cos\theta}} d(\rho r) \quad (2.15)$$

$$P_{j,l} = \sum_{t=1}^{l-1} e^{-\left(\frac{\mu}{\rho}\right)_{j,t} \frac{\rho R_l - \rho R_{t-1}}{\cos\theta}} \quad (2.16)$$

where  $W_{j,l}$  is the  $j$ -th element concentration in the  $l$ -th layer,  $\left(\frac{\mu}{\rho}\right)_{j,l}$  is the attenuation coefficient for the X-ray emitted by  $j$ -th element in the  $l$ -th layer,  $\rho R_l$  is the position of the interface between the  $l$ -th and  $l+1$ -th layers measured from the surface.

In eq. 2.15, the argument of the first summation represents the contribution to the X-ray yield coming from each layer. The exponential inside the integral takes into account the X-ray attenuation in the  $l$ -th layer.  $P_{j,l}$  represents the overall X-ray attenuation in the preceding layers (from the surface to the  $l$ -th one).

All the other terms are specified in Sec. 2.2.1.

It is important to point out that the evaluation of  $(\rho r)(E)$  must consider the different layer compositions

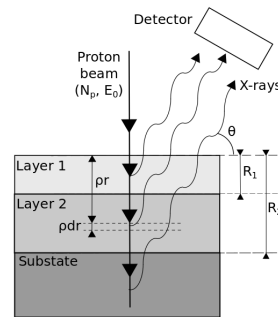


**Figure 2.7:** Scheme of PIXE analysis with multilayer targets.

and thicknesses  $(\rho R_{l+1} - \rho R_l)$ :

$$(\rho r)(E) = \int_{E_l}^E \frac{dE'}{S_l(E')} \text{ for the } l\text{-th layer} \quad (2.17)$$

where  $E_l$  is the proton energy when it crosses the interface  $R_{l-1}$  between the  $l - 1$ -th and  $l$ -th layer, while  $S_l(E)$  is the proton stopping power for the  $l$ -th layer.

Here, the X-ray attenuation coefficients  $(\mu/\rho)_{j,t}$  for the different photon energies (eq. 2.9) and layers are known, as well as the projectiles stopping powers  $S_l(E)$  (eq. 2.14), because the layers' composition are known a priori. The only unknowns are the interfaces  $R_l$  between layers, and they can be always found with the iterative method already described. In order to obtain a closed system of equations, the number of measured yields  $J$  has to be higher or at least equal to the number of unknown thicknesses  $L$ .

In any case, the evaluation of the path as a function of the energy  $\rho r(E)$ , and the substitution inside  $\sigma_j(E)$  in order to find  $\sigma_j(\rho r)$ , has to be done at any iteration because the thicknesses of the layers influence the projectile energy loss.

## 2.2.4 Generic non-homogeneous target

Consider now the case of a generic target structure, for which the distribution of the elements along the thickness is completely unknown. In such a condition, the goal of the analysis is to retrieve the concentration profiles of the elements starting from the surface up to a thickness of a few  $\mu\text{ms}$ . The procedure described in this paragraph was proposed for the first time in [2] and it is called *Differential PIXE*.

Let assume to have a sample composed of  $J$  elements (index  $j$ ) distributed in an unknown way along the thickness.  $N$  proton beams of different energy (index  $k$ ) are made to impinge on the sample. The sample is split into  $L$  sublayers (index  $l$ ) for which a uniform and unknown concentration is assumed. The goal of the analysis is to find a discrete approximation of the real concentration profile. The equation for the measured X-ray yield associated to the  $j$ -th element  $Y_j^k$  is practically identical to the one already reported for the multilayer target case

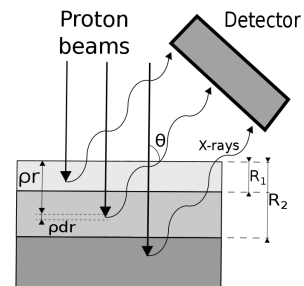


**Figure 2.8:** Scheme of PIXE analysis with generic non-homogeneous targets.

(eq. 2.15), but with a dependence on the ion beam energy (the  $k$ -index term):

$$Y_j^k = N_p^k \frac{\Delta\Omega}{4\pi} \varepsilon_j \frac{N_{av}}{M_j} \sum_{l=1}^L W_{j,l} P_{j,l} \int_{\rho R_l}^{\rho R_{l+1}} \sigma_j(\rho r) \omega_j e^{-\left(\frac{\mu}{\rho}\right)_{j,l} \frac{\rho r}{\cos\theta}} d(\rho r) \quad (2.18)$$

$$P_{j,l} = \sum_{t=1}^{l-1} e^{-\left(\frac{\mu}{\rho}\right)_{j,t} \frac{\rho R_t - \rho R_{t-1}}{\cos\theta}} \quad (2.19)$$

Here,  $N_p^k$  is the number of primary particles for the  $k$ -th beam, while the other terms in the expression have already been described in Sec. 2.2.3.

A system of equations can be written, where the unknowns are the  $J \times L$  concentrations  $W_{j,l}$  in the layers for the different elements. Performing  $N$  measurements with different proton energies,  $N \times J$  values for the X-ray yields will be recorded. For  $N = L$  the system is closed and the set of discrete  $W_{j,l}$  which better approximate the continuous concentration profile can be found.

In [2], the author introduces “generalized quantities” to simplify the discussion:

$$Y_j^{k*} = Y_j^k \frac{M_j}{\varepsilon_j} \quad (2.20)$$

$$A_k = \frac{\Delta\Omega}{4\pi} N_p^k N_{av} \quad (2.21)$$

$$T_{j,l}^k = P_{j,l} \int_{\rho R_l}^{\rho R_{l+1}} \sigma_j(\rho r) \omega_j e^{-\left(\frac{\mu}{\rho}\right)_{j,l} \frac{\rho r}{\cos\theta}} d(\rho r) \quad (2.22)$$

So, the system can be written in this more compact form:

$$Y_j^{k*} = A_k \sum_{l=1}^L T_{j,l}^k W_{j,l} \quad (2.23)$$

because the  $W_{j,l}$  are present in the expression of  $T_{j,l}^k$ .

The solution of eq. 2.23 involves an iterative procedure because the  $W_{j,l}$  are present in the expression of  $T_{j,l}^k$ . Assuming that also the proton numbers represented by  $A_k$  are unknown, the elemental concentrations can be found following these steps:

1. Assume a homogeneous elemental composition inside the target.
2. Find a set of concentrations  $W_j(E_k)$  for each initial proton beam energy, assuming that the target is homogeneous. In this way also a first approximation for  $A_k$  is found.
3. Assume that the concentrations  $W_j(E_k)$  are characteristic of certain depths  $h_k$  evaluated as:

$$h_k = \sum_{j=1}^M W_j(E_k) \frac{\int_0^{E_k} r \sigma_j e^{-\left(\frac{\mu}{\rho}\right)_j \frac{\rho r}{\cos\theta}} \frac{dE}{S(E)}}{\int_0^{E_k} \sigma_j e^{-\left(\frac{\mu}{\rho}\right)_j \frac{\rho r}{\cos\theta}} \frac{dE}{S(E)}} \quad (2.24)$$

where  $S(E)$  and  $\left(\frac{\mu}{\rho}\right)_j$  are evaluated for the homogeneous target.

4. Subdivide the target in layers assuming the boundary to be placed at the arithmetic mean of  $h_k$  and  $h_{k+1}$ :

$$R_l = \frac{h_k + h_{k+1}}{2} \quad (2.25)$$

5. Apply an iterative procedure in order to find the values of  $W_{j,i}$  which minimizes the  $\chi^2$ :

$$\chi = \sum_{j,k} \left( \frac{Y_{j,exp}^{k*}}{\langle Y_{j,exp}^{k*} \rangle_{max}} - \frac{Y_{j,th}^{k*}}{\langle Y_{j,th}^{k*} \rangle_{max}} \right)^2 \quad (2.26)$$

where *exp* and *th* stand for experimental and theoretical respectively.

6. Once the concentrations  $W_{j,l}$  have been found, a new set of  $A_k$  can be calculated from:

$$A_k = \frac{\sum_j Y_j^{k*}}{\sum_{j,l} T_{j,l}^k W_{j,l}} \quad (2.27)$$

7. Resume from point 5 with the new values of  $A_k$  and  $W_{j,l}$ .

The procedure stops when the difference between the  $\chi$ -parameter values for two consequent iteration steps falls below a certain threshold value.

The constraints that can be applied to the elemental concentrations are that they must be always between 0 and 1, and that the sum on the same layer must be equal to 1. With this procedure, a set of discrete values for  $W_{j,l}$ , approximating the unknown concentration profiles, can be derived.

## 2.3 PIGE analysis

Similarly to what has been done in Sec. 2.1 regarding PIXE, here PIGE analysis will be described in detail. PIGE is a complementary technique with respect to PIXE showing strong similarities with the latter. Indeed, PIGE is employed to determine the elemental composition of samples, as for PIXE primary particles are protons and the secondary particles are again photons. But now, the measure no longer involves X-rays, but  $\gamma$ -rays induced in nuclear reactions by the protons incident on the target. Accordingly, the subject of this Section is how  $\gamma$ -rays interact with matter and which type of detectors have to be employed.

### 2.3.1 $\gamma$ -rays Spectrometry

The experimental apparatus used to perform PIGE analysis is quite similar to that of PIXE, except for the detector employed to measure the photon energies. The distinction between X-rays and  $\gamma$ -rays is due to their different origin: in the first case, the starting process involves an electronic transition, while in the

second one, the transition is between excited nuclear states. As a consequence, the  $\gamma$ -ray energies are much higher with respect to the X-ray ones, so the radiation is more penetrating and this requires the use of different detectors from Si(Li), in particular NaI(Tl) scintillators or Ge semiconductors detectors.

### Interaction of $\gamma$ -rays with matter

In order to correctly interpret PIGE spectra, it is necessary to consider the various processes involved in the interaction between  $\gamma$ -photons and matter:

- **Photoelectric effect** is a phenomenon in which electrons are released when the electromagnetic radiation is absorbed inside the material. During the process, almost the entire photon energy  $h\nu - E_b$ , where  $h\nu$  is the  $\gamma$ -ray energy and  $E_b$  is the electron binding energy, is transferred to the electron which starts to move inside the medium. There is also the formation of a vacancy in the atomic shell and the subsequent emission of an Auger electron or an X-ray. The electron quickly releases all its energy to the active medium due to the high stopping power and so the recording signal is proportional to the initial photon energy. As the result of this process, the photopeak directly associated with the emitting element appears in the spectrum. The important dependencies for the cross section  $\sigma_p$  of photoelectric effect are:

$$\sigma_p \propto \frac{Z^4}{(h\nu)^3} \quad (2.28)$$

where  $Z$  is the atomic number of the medium.

- **Compton scattering** consists of an inelastic collision between a photon and an electron. Thus, the photon is deviated from the initial direction and the electron acquires kinetic energy. The photon transfer part of its energy to the electron. As the result, a continuous spectrum is formed by the fact that the electron is easily absorbed into the active medium, while the scattered photon is able to escape without releasing energy. Here, the probability  $\sigma_c$  is proportional to

$$\sigma_c \propto \frac{Z}{(h\nu)^2} \quad (2.29)$$

- **Pair production** is a process which involves only photons with energy higher than 1.022 MeV and which takes place only when they are in the vicinity of a nucleus. It consists in the creation of an electron-positron pair and the disappearance of the photon. The presence of the energy threshold is motivated by the fact that the emitted particles have both a rest mass equal to 0.511 MeV.

If the  $\gamma$ -ray energy is higher than the minimum amount to create the pair,

the excess is acquired by the electron and positron as kinetic energy (they are emitted in opposite directions). Generally the electron releases its energy to the medium and then stops, while the positron, after slowing down, annihilates with another electron. The annihilation results in the emission of two  $\gamma$ -rays of energy equal to 511 keV. These photons can be absorbed inside the detector through the other two processes, or they can escape generating a “single escape” peak (only one photon is absorbed inside the medium) or a “double escape” peak (both photons escape from the medium). The probability for this process is:

$$\sigma_{pp} \propto Z^2 \ln(h\nu[\text{n.u.}]^1) \quad (2.30)$$

### Semiconductors vs. Scintillation detectors

The choice for a  $\gamma$ -ray energy dispersive detector falls into two categories: scintillators and semiconductors. Among them, the most significant are the NaI(Tl) detectors and the Germanium detectors. The choice is based on a trade-off between efficiency and resolution.

Scintillators are characterized by very high densities and active volumes, which are likely to absorb the radiation completely, also thanks to the high  $Z$  number of Iodine. However, the energy resolution is very low compared to the Ge detectors. On the other hand, semiconductors are characterized by smaller dimensions and lower atomic number  $Z$  and this results in a lower efficiency.

Because of this, Ge detectors are preferred in bulk analysis with complex spectra for which a good resolution is required. Conversely, when a good energy resolution is not crucial, NaI(Tl) are preferred. This is particularly important when depth profiling is performed, for which the variation in  $\gamma$ -ray intensities for different initial energies of the projectile provides information about the non-homogeneity of the sample.

## 2.4 Theoretical description of PIGE

As reported in [42], the theoretical formalism necessary to describe PIXE and PIGE are very similar. In both the techniques there are monoenergetic particles which slowdown inside a medium causing the emission of photons. In the case of PIXE, atomic transitions are involved and the detected radiation is in the form of X-rays, while for PIGE the reactions are between projectiles and nucleus. In this second case, photons are emitted in the form of  $\gamma$ -rays. So in both cases, for thick targets, the slowdown of the projectile has to be taken into account, as well as the energy dependent cross section for ionization or nuclear reaction. As far as the thick target case is concerned, the main differences with respect to eq. 2.11 are:

---

<sup>1</sup>n.u. = normalized units



- The absence of the exponential term inside the integral, because  $\gamma$ -ray absorption inside the target can be neglected (the proton range in water is of the order of tens of  $\mu\text{m}$  considering  $E_0 \sim \text{MeV}$ , while  $\gamma$ -rays can travel for cm).
- The presence of the isotopic abundance  $f_i$ , because the emitted  $\gamma$ -rays are isotope- specific.
- The presence of the nuclear reaction cross section  $\sigma_\gamma$  instead of the ionization one.

Therefore, the expression for the  $\gamma$ -ray yield  $Y_\gamma$  can be written in this way:

$$Y_\gamma(E_0) = N_p \frac{\Delta\Omega}{4\pi} \varepsilon_\gamma W \frac{N_{av}}{M} f_i \int_0^{E_0} \sigma_\gamma(E) \frac{d(E)}{S(E)} \quad (2.31)$$

where  $E_0$  is the initial proton energy,  $N_p$  is the number of incident protons,  $\Delta\Omega$  and  $\varepsilon_\gamma$  are the detector solid angle and efficiency,  $W$  is the element mass concentration,  $N_{av}$  is the Avogadro's number,  $M$  is the atomic mass,  $f_i$  is the isotopic abundance,  $\sigma_\gamma$  is the nuclear reaction cross section and  $S(E)$  is the projectile mass stopping power.

### 2.4.1 PIGE analysis with standards

In the case of PIGE, nuclear cross sections are reported only for fixed angles between the primary particle beam and the  $\gamma$ -rays emission direction. Furthermore, they cover a small range of energies. Solving eq. 2.31 using an iterative procedure like in the case of PIXE would imply the precise knowledge of  $\sigma_\gamma(E)$  and this is feasible only in particular cases. Then, the adoption of a different strategy is necessary: the use of standards of known composition in order to bypass the knowledge of the cross sections. The fundamental hypothesis is that the energy loss in the standard  $S_{st}(E)$  and in the sample  $S_{samp}(E)$  are linked by a linear relationship [3]:

$$k = \frac{S_{samp}(E)}{S_{st}(E)} \quad (2.32)$$

Writing eq. 2.31 both for the sample and the standard, substituting eq. 2.32 and calculating the ratio we get:

$$W_{samp} = W_{st} \frac{Y_{samp}(E_0)}{Y_{st}(E_0)} k \quad (2.33)$$

So, from the knowledge of the mass concentration in the standard  $W_{st}$  and measuring the  $\gamma$ -ray yield for the standard  $Y_{st}(E_0)$  and for the sample  $Y_{samp}(E_0)$ , the unknown mass concentration  $W_{samp}$  can be retrieved from eq. 2.33. Assuming  $k \sim 1$ , the evaluation of the concentrations will be as precise as the standard and sample have a much similar composition.

### 2.4.2 PIGE bulk analysis without standards

PIGE analysis without standards is performed essentially adopting an iterative procedure similar to the one described in Sec. 2.2 for PIXE. The integration of the ionization cross sections is straightforward because they are smooth functions of the projectile energy. On the other hand, nuclear cross sections are characterized by strong resonances. In any case, taking an integration path sufficiently narrow to resolve the various resonances, the numerical integration becomes trivial.

A procedure of this kind was applied for the first time by Mateus in ref. [42], where the  $\gamma$ -ray yield for four different elements ( ${}^7\text{Li}$ ,  ${}^{10}\text{B}$ ,  ${}^{19}\text{F}$  and  ${}^{23}\text{Na}$ ) were calculated and compared with the experimentally measured one. The discrepancy obtained was always lower than 7.5%.

Over the years, many information have been accumulated in the literature about PIGE and the related nuclear cross sections. Most of the datasets were collected compiled in the Experimental Nuclear Reaction Data (EXFOR) library [51, 52], including differential cross sections and yields. As reported in [53], until a few years ago, a large number of published data were present in literature, but they were not clearly organized in order to be useful for IBA purposes. There was a significant discrepancy between different papers and a strong lack of data in many energy ranges useful for PIGE analysis.

Starting from 2010, the situation has improved thanks to a 5-years project (Coordinated Research Project) coordinated by Atomic Energy Agency (IAEA). It was aimed at organizing and updating a database of nuclear cross sections. A review of the current situation is presented in [53]. As the result, the most complete collection of experimental data is available in the Ion Beam Analysis Nuclear Data Library (IBANDL) and a computer code Emitted Radiation Yield Analysis, ERYA, has been developed. As reported in the paper, the updating is still going on and further experimental measures are needed in order to validate the data already uploaded.

### 2.4.3 Resonance depth profiling

PIGE does not allow to perform depth profiling through the energy attenuation of the products, as other NRA techniques do. However, it is possible to probe the composition of the material according to the thickness using the presence of resonances in the cross sections. When the nuclear cross section presents an isolated resonance, it becomes possible to scan the sample composition as a function of depth, pushing the resonance inside the material by increasing the proton initial energy. The  $\gamma$ -ray yield will be representative of the local composition where the resonance lies, as it is shown in fig. 2.9. Alongside, an example of nuclear cross section suitable to perform this kind of analysis is also reported (fig. 2.10) .

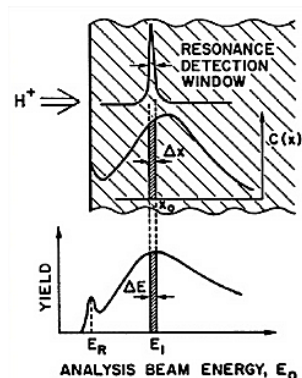


**Figure 2.9:** *PIGE resonance depth profiling scheme*

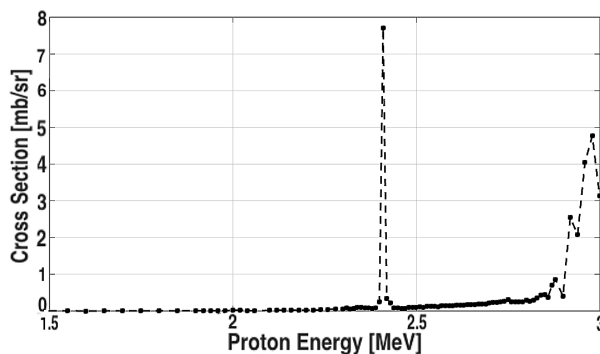


**Figure 2.10:** *Example of cross section from IBANDL database:  $^{24}\text{Mg}(p, p\gamma)^{24}\text{Mg}$ ,  $90^\circ$  between beam direction and detector,  $E_\gamma = 1369 \text{ keV}$*

## 2.5 Open issues and goals of the thesis work

The general purpose of the thesis work is to study the possibility to perform Particle Induced X-ray Emission and Particle Induced  $\gamma$ -ray Emission with laser-driven proton sources.

As stated in Chapters 1 and 2, Ion Beam Analysis is a group of unique techniques for elemental analysis characterized by a series of properties: they are non-destructive, and they allow retrieving stratigraphic information about the elemental composition of the sample.

In particular, in particular PIXE and PIGE stand out for their extraordinary versatility in terms of the possible variants with which they can be run. Essentially, the greater limitation of these techniques lies in the nature of their primary ion source.

Cyclotrons and Van de Graaff generators are currently employed to generate monoenergetic protons to perform IBA studies in almost 300 research centers worldwide, including PIXE and PIGE analysis. Despite the continuous evolution and optimization of these machines, they still present some disadvantages.

- First of all, particle accelerators are very expensive both in terms of purchase and maintenance.
- Another important limitation lies in their large dimensions, which make them not portable and useless in order to perform on-site measurements. IBA is often employed to analyze samples of artistic and historical importance which can not always be transported, for example large paintings, statues and frescoes. These features prevent the large-scale diffusion of Ion Beam Analysis techniques.
- The ion current provided by Van de Graaff and cyclotrons commonly

employed to perform IBA ranges from tens of pA up to tens nA, and this means that a few minutes will be required to complete a measurement. Moreover, these machines are not easily tunable, so changing the particle energy can require tens of minutes or more. Altogether, performing an analysis that requires to irradiate the sample with different energies (e.g. *Differential PIXE*) would result in a very long procedure.

- Finally, the primary particle energy is generally of the order of few MeV which allows probing sample thicknesses only in the order of some  $\mu\text{m}$ .

In the light of the above mentioned limitations, finding an alternative source more versatile than conventional accelerators could make the IBA more appealing.

Laser-driven proton sources could provide a viable alternative, as they are currently capable of producing protons in the IBA energy range of interest, and they are able, at least in principle, to overcome all the above mentioned limitations. A radical change of technology could result in a significant reduction in the size of the experimental apparatus and of the associated costs. Not only, having a faster tunable source would make the overall analysis faster and the possibility to dispose of more energetic particles would increase the analytical capability of these techniques. In principle, a system based on a laser would be more compact and less expensive than particle accelerators, the energy can be modified simply by changing the parameters of the laser pulse, they allow disposing of kA for each bunch. This would produce a better signal-to-noise ratio, and hence a better quality of the measurement. Furthermore, laser-driven proton sources are characterized by strong laminarity at the source and the maximum available energy can be extended up to tens of MeV. Considering the need for extensive surface analysis, they would be very beneficial, since proton beam spot size is of the order of  $\text{cm}^2$ . Regarding PIXE, the availability of such high currents, in conjunction with the high values of the ionization cross sections, could allow for ultra-high-speed analysis at the limit with a single shot. With reference to *Differential PIXE*, the use in succession of particle beams with different energies could be replaced by the employment of bunches characterized by different cut-off energies.

So, the primary goal is to properly modify the models currently available to describe PIXE, when monoenergetic protons are employed, in order to include the presence of a non-monoenergetic primary particle source. Subsequently, the adapted models need to be applied to verify their functionality. So, they must be tested considering all the possible cases described in Sec. 2.2, initially adopting an idealized approach as far as the detector and spectrum of the incident protons are concerned. To this aim, a comparison with the results generated by the conventional analysis based on monoenergetic protons is also required. Then, the final test will be to consider a more realistic situation both for the experimental set-up, considering cases present in literature, and concerning samples

of interest in the field of cultural heritage.

In order to accomplish all these intents, it is necessary to define clearly the methodology that must be followed. First of all, testing the developed models necessarily implies the elaboration of numerical codes which, starting from the X-ray yields experimentally measured, provide the unknown sample composition. Without disposing of real PIXE experimental data, the models validation has been done exploiting "synthetic experiments" performed with Monte Carlo simulations, in particular employing the Geant4 toolkit. The use of simulations will then allow to generate data of the X-ray yields for all the possible kinds of targets already described, which will be passed as input to the numerical codes. If the sample compositions resulting from the analysis are consistent with those inserted in the Monte Carlo, the analysis has been successful and the validity of the models is proven. This will be done both considering monoenergetic protons and with a simple exponential energy spectrum.

Finally, as mentioned earlier, the Monte Carlo and the models will be applied to test a more complex analysis case, considering a real possible detector configuration and using a more realistic proton spectrum in the simulation. The latter will be provided by another numerical instrument, the Particle In Cell (PIC) method, generally employed for kinetic simulations of plasma.

It is emphasized that a useful by-product of this work, aimed to validate the developed models, will be numerical codes which can be used to interpret future experimental data.

In conclusion, the structure of the thesis will be as follows: in Chapter 3 the numerical codes Geant4 and PIC simulation will be presented from a general point of view, while Sec. 4.2 will get more into detail about the PIXE simulation. Sec. 4.1 will be dedicated to describe the new models for the analysis of PIXE spectra obtained from non-monoenergetic protons. Then, the simulations and the analysis of the results for the four cases, both with monoenergetic and exponential proton spectra, will be presented in Sec. 4.3. Finally, Chapter 5 will treat the simulation of a more realistic experiment and the analysis of paintings with PIXE/PIGE, respectively in Sec. 5.1 and 5.2.

## Chapter 3

# Numerical simulation tools

This Chapter introduces the numerical tools needed to simulate the PIXE technique, as well as the protons bunch generation through the interaction between super-intense laser pulses and solid targets. Two different types of numerical instruments are involved:

- **Particle in Cell (PIC) simulation** [54, 55, 56] is a technique for kinetic simulations of plasma, performed with the Piccante code. Through a combined Eulerian and Lagrangian approach, it provides a solution to the Maxwell-Vlasov system of equations. In this work, a two-dimensional PIC simulation will be used to obtain the energetic and angular distribution of a proton bunch generated by the interaction of a super-intense laser pulse and a solid target.
- **Monte Carlo simulation** is a numerical instrument which can be employed to simulate the transport of particles into matter. More specifically, the numerical code used in this work is Geant4 [59, 60, 61]. Once the code needed to simulate the PIXE technique has been implemented, different primary particles spectra will be used as input to the program: before simple exponential energy spectra and then, that obtained by the PIC simulation.

### 3.1 Geant4 Monte Carlo simulation toolkit

In this section, the aim is to provide an overview of Geant4, taking the user manual [62] as a point of reference in the dissertation, while some more detailed aspects about the PIXE simulations will be treated in the Sec. 4.2.

Geant4 (Geometry and Tracking) is an abstract base classes' toolkit for simulating the transport of particles into matter, released for the first time in 1998. This toolkit allows the programmer to implement the transport physics of electrons, ions, photons etc. inside matter and the creation of secondary particles, covering a wide range of energies (from eV to TeV). It is currently used to perform Monte

Carlo simulations for various applications, such as high energy physics, space and radiation, medical and technology transfer [59, 60]. It is written in C++ and it was the first Monte Carlo code to employ object-oriented programming. An abstract class can be considered as an interface which serves as a starting point for generating specific classes. Essentially, an abstract class can not be instantiated by itself, but it can act as a "type" for the declaration of a concrete class that will inherit all the properties of the abstract class.

So, the programmer can write his own code building concrete derived classes from the abstract classes provided by the toolkit. From the concrete classes, instances (objects) can be created in turn. In the object-oriented programming, class abstraction aims to simplify the basic structure of a program and thus facilitates its management and expansion.

In Geant4 toolkit, abstract classes are grouped into 17 main categories, or in-

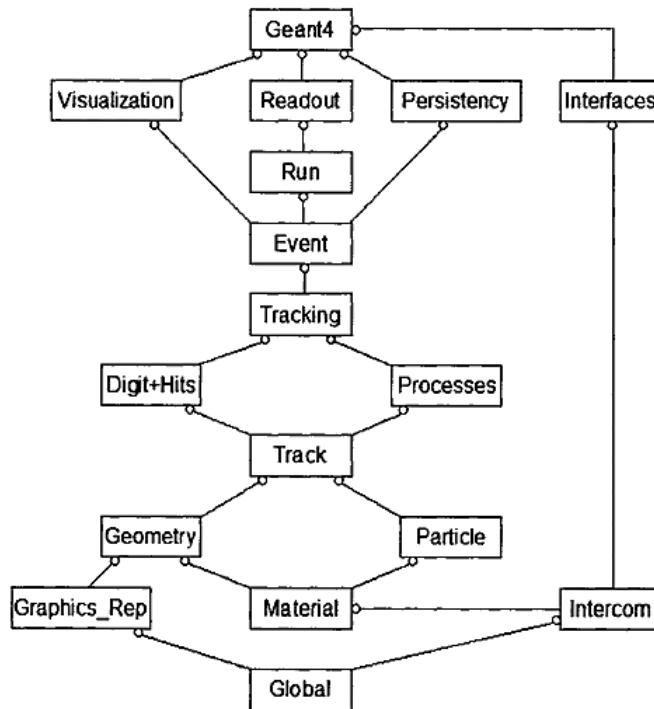


**Figure 3.1:** *Geant4 class category diagram.*

dependent logic units, as shown in the block diagram in the fig. 3.1. Lines connecting blocks (class categories) represent relationships between classes which belong to different categories. The block that has the empty point at the end of the line uses the classes of the linked category. Notice that the categories below are the foundations of the toolkit and are used by the top categories.

### 3.1.1 *main()* program

Geant4 does not provide a *main()* virtual method, so it must be declared by the user because its content should change from simulation to simulation. Here a simple example of *main()* function is reported and the basic instructions will be explained in the following.

```

1  int main()
2  {
3      G4RunManager* runManager = new G4RunManager;
4
5      //Mandatory classes
6      runManager -> SetUserInitialization(new ExDetectorConstruction);
7      runManager -> SetUserInitialization(new ExPhysicsList);
8      runManager -> SetUserAction(new ExPrimaryGeneratorAction);
9
10     //Optional Classes
11     runManager -> SetUserAction(new ExRunAction);
12     runManager -> SetUserAction(new ExEventAction);
13     runManager -> SetUserAction(new ExSteppingAction);
14
15     runManager -> initialize();
16
17     G4UImanager* UI = G4UImanager::GetUIpointer();
18     UI -> ApplyCommand("/run/verbose_1");
19     UI -> ApplyCommand("/event/verbose_1");
20     UI -> ApplyCommand("/tracking/verbose_1");
21
22     int numberOfEvent = 10;
23     runManager -> BeamOn(numberOfEvent);
24
25     delete runManager;
26     return 0;
27 }

```

Inside the *main()*, the instances to two classes must be created:

- ***G4RunManager*** controls the flow of the program and it is necessary to provide with it all the information needed to run the simulation. Essentially, this is the only mandatory manager class that needs to be explicitly instantiated by the user (line 3).

Once created, the programmer needs to pass to this class the pointers to the classes in which all the information necessary to perform the simulation is defined. This is done with the instructions at lines 5, 6 and 7. Here, a pointer to the concrete class *ExDetectorConstruction* is created (*new ...*) and passed as argument to the *SetUserInitialization* method. In this case, *ExDetectorConstruction* is the concrete class created from the abstract *G4VUserDetectorConstruction* class and it contains the definition of the geometry.

The instruction at line 13 creates the physics processes, the geometry, etc. The final instruction at line 21 starts to run 10 subsequent events. Note that the *runManager* object must be deleted at the end of the simulation (line 23).



- *G4UIManager* is another manager class that allows the user to pass commands to the program and to set the verbosity at various levels of the simulation. In the example, at line 15, the pointer to the class is instantiated and in the subsequent three lines it is used to fix the verbosity levels at 1.

So in essence, the management of the program is entrusted to the run manager, which must be provided, through the pointers to the appropriate classes, with all the information needed to set up the simulation. Each class can fulfill the function of providing fundamental information (**Mandatory User Classes**), or it can be used to extract information on different levels of the simulation (**Optional User Classes**<sup>1</sup>).

### 3.1.2 Mandatory user classes

There are three mandatory classes the user has to instantiate from the corresponding abstract classes provided in the Geant4 toolkit: the *G4VUserDetectorConstruction*, *G4VUserPhysicsList* initialization classes and the *G4VUserPrimaryGeneratorAction* action class. In these classes the minimum requirements for launching a simulation are defined: the geometry of the system, the materials, the particles involved and their properties, the physical processes a particle can undergo, etc.

#### Geometry definition: the *G4VUserDetectorConstruction* class

The *G4VUserDetectorConstruction* initialization class is the abstract class from which the user can instantiate the concrete class (in the example *ExDetectorConstruction*) containing all the information about the geometry:

```

1 class ExDetectorConstruction : public G4VUserDetectorConstruction
2 {
3     public:
4         ExDetectorConstruction ();
5         virtual ~ExDetectorConstruction ();
6
7         virtual G4VPhysicalVolume* Construct ();
8
9     private:
10        void DefineMaterials ();
11        G4VPhysicalVolume* DefineVolumes ();
12 };

```

All the information regarding the experimental setup must be defined inside the body of the function *Construct()*. In fact, in the following example of code, two other methods are called within the body of the function:

```

1 G4VPhysicalVolume* ExDetectorConstruction::Construct ()
2 {
3     DefineMaterials ();
4     return DefineVolumes ();
5 };

```

<sup>1</sup>Also the pointers to these classes must be passed to the *runManager*.

The method *DefineMaterials()* is used to define all the materials present in the geometry. An example of its shape is shown:

```

1 void ExDetectorConstruction::DefineMaterials()
2 {
3     G4NistManager* nistManager = G4NistManager::Instance();
4     nistManager -> FindOrBuildMaterial("G4_O");
5 };

```

here, the Nist database is used in order to include Oxygen. The geometry is fixed through the definition of a finite number of volumes, the largest of which is the World. Once the World has been created, all other volumes are in turn defined and positioned in relation to it. This is done inside the function *DefineVolumes()*. The following shows a simple example where only one volume (the World) is defined:

```

1 G4VPhysicalVolume* ExDetectorConstruction::DefineVolumes()
2 {
3     G4VSolid* worldEx
4     = new G4Box("WorldEx",           //its name
5               10*cm, 10*cm, 10*cm); //its size
6     G4LogicalVolume* worldLV
7     = new G4LogicalVolume(
8           worldEx,           //its solid
9           worldMaterialEx,   //its material
10          "World");          //its name
11    G4VPhysicalVolume* worldPV
12    = new G4PVPlacement(
13          0,                  //no rotation
14          G4ThreeVector(),    //at (0,0,0)
15          worldLV,            //its logical volume
16          "World",           //its name
17          0,                  //No mother volume (the only)
18          false,              //no boolean operator
19          0,                  //copy number
20          fCheckOverlaps);    //overlaps checking
21    return worldPV;
22 }

```

As shown in the example, the definition of the geometry is made passing through three steps:

1. The creation of a **solid** involves the definition of a geometric shape and its dimensions (line 3). Among the solids there are boxes (*G4Box*), cylinders (*G4Tubs*), cones (*G4Cons*), spheres (*G4Sphere*), etc.
2. The creation of a **logical volume** involves the assignment of a material to a solid already created (line 6).
3. The creation of a **physical volume** involves the placement of a logical volume inside an already-existing volume (i.e. the new volume is placed with respect to the center of the "mother" volume). Essentially all the volumes need to be placed in a mother volume except the World, which is the largest one.

### Particles and physics: the *G4VUserPhysicsList* class

The user has to create a derived class from the abstract *G4VUserPhysicsList* initialization class, where all particles and processes involved in the simulation must be registered:

```

1  class ExPhysicsList: public G4VUserPhysicsList
2  {
3      public:
4          ExPhysicsList ();
5          virtual ~ExPhysicsList ();
6
7          void ConstructParticle ();
8          void ConstructProcess ();
9          void SetCuts ();
10
11         private:
12             G4VPhysicsConstructor* emPhysicsList ;
13
14             G4double cutForGamma ;
15             G4double cutForElectron ;
16             G4double cutForProton ;
17     };

```

The user must implement the following virtual methods:

- ***ConstructParticle()***

In this method, all particles involved in the simulation must be called, for example:

```

1  void ExPhysicsList::ConstructParticle ()
2  {
3      G4Gamma::GammaDefinition ();
4      ...
5  }

```

As far as the particles are concerned, their definition is made on the basis of classes (specific for each particle type) derived from the generic class *G4ParticleDefinition*. This class contains all the static properties of a particle (its name, mass, spin, etc.). The class *G4DynamicParticle* describes the properties of a particle in motion (its energy, momentum, etc.) and it takes a pointer to the corresponding *G4ParticleDefinition* class. The class *G4Track* describes the status of a particle at the end of a step and it takes a pointer to associated *G4ParticleDefinition* and *G4DynamicParticle* classes.

- ***ConstructProcess()***

In this method, all physical processes must be registered, for example:

```

1  void ExPhysicsList::ConstructProcess ()
2  {
3      AddTransportation (); //particle transport
4      ConstructEM (); //electromagnetic physics
5      ...
6  }

```

As in the case of particles, each process is derived from the *G4VProcess* base class, which provides three "doIt" virtual methods and three "GPIL" methods. The doIt methods describe the interaction (along the step, at the end of a step or when the particle stops) in terms of products and state of the primary particle at the end of the process, while the GPIL methods determines when the interaction takes place on the basis of its probability of occurrence. In Geant4, processes are divided into seven categories: electromagnetic, hadronic, decay, photolepton-hadron, optical, parametrization and transportation.

- *SetCuts()*

In this function all the range thresholds for particles are defined. The ranges are converted into energy thresholds for individual materials, below which no secondary particles are produced.

In Geant4, particles are tracked down to zero kinetic energy or until they reach the limits of the World. In any case, secondary electrons and photons are generated only above the threshold in order to avoid an excess of secondary particles that need to be simulated. If not, there would be a deterioration in simulation performance.

```

1 void ExPhysicsList::SetCuts()
2 {
3     // set cuts for gamma at first and for e- second and next for
4     // e+, because some processes for e+/e- need cut values for gamma
5     SetCutValue(1*cm, "gamma");
6     SetCutValue(1*cm, "e-");
7     SetCutValue(1*cm, "e+");
8 }

```

### Generate primary particles: the *G4VUserPrimaryGeneratorAction* class

In the *G4VUserPrimaryGeneratorAction* class it is specified which kind of primary events need to be generated. In the constructor of the concrete class, the primary generator has to be instantiated (line 8). For example *G4particleGun* is a generator supplied by Geant4 which provides primary particles with a fixed energy, momentum and direction (they are supplied by the programmer at lines 20-23).

The *GeneratePrimaries()* method of the *G4VUserPrimaryGeneratorAction* class is called at the beginning of each event and it must contain a call to the *G4VUserPrimaryGeneratorAction* concrete class, invoking the method *generatePrimaryVertex()* (at lines 31-34).

Additionally, inside the *GeneratePrimaries()* concrete method also a series of additional methods can be called before the invocation of *generatePrimaryVertex()*, in order to randomize the energy, momentum, etc. of the primary particles (for example, at lines 33-34, the energy has been randomized between 0 and 1 MeV).

```

1 class ExG4PrimaryGeneratorAction01 : public G4VUserPrimaryGeneratorAction
2 {
3     public:
4         ExG4PrimaryGeneratorAction01();
5         ~ExG4PrimaryGeneratorAction01();

```

```

6     virtual void GeneratePrimaries(G4Event*);
7     private:
8         G4ParticleGun* fParticleGun;
9     };
10    ////////////////////////////////// Constructor //////////////////////////////////
11    ExG4PrimaryGeneratorAction01::ExG4PrimaryGeneratorAction01()
12    : G4VUserPrimaryGeneratorAction(),
13    fParticleGun(0)
14    {
15        G4int nofParticles = 1;
16        fParticleGun = new G4ParticleGun(nofParticles);
17        G4ParticleTable* particleTable = G4ParticleTable::GetParticleTable();
18        G4ParticleDefinition* particle = particleTable->
19        FindParticle("proton");
20        fParticleGun -> SetParticleDefinition(particle);
21        fParticleGun -> SetParticleEnergy(1*MeV);
22        fParticleGun -> SetParticlePosition(G4ThreeVector(0,0,0));
23        fParticleGun -> SetParticleMomentumDirection(G4ThreeVector(0,0,1));
24    }
25    ////////////////////////////////// Destructor //////////////////////////////////
26    ExG4PrimaryGeneratorAction01::~ExG4PrimaryGeneratorAction01()
27    {
28        delete fParticleGun;
29    }
30    ////////////////////////////////// Method //////////////////////////////////
31    void ExG4PrimaryGeneratorAction01::GeneratePrimaries(G4Event* anEvent)
32    {
33        G4double Energy = G4UniformRand()*1*MeV;
34        fParticleGun -> SetParticleEnergy(Energy);
35        fParticleGun -> GeneratePrimaryVertex(anEvent);
36    }

```

### 3.1.3 Optional user classes

Geant4 provides five optional Action Classes which give access to information at various levels of the simulation:

- ***G4UserRunAction***

A run is the largest unit of a simulation and it is represented by the abstract class *G4Run*. Essentially, it is a collection of events which share the same geometry and physics. The *G4UserRunAction* class contains methods which are invoked at the beginning and at the end of a simulation and allow initializing and save the histograms containing the data extracted.

- ***G4UserEventAction***

At the beginning of processing, a certain number of primary particles are generated, and they are pushed into a stack. Then, each particle is extracted from the stack and tracked. Eventually, if created, the secondary particles are also pushed into the stack. When the stack is empty, the processing of the event is finished. The methods belonging to the *G4UserEventAction* class are called at the beginning and at the end of each primary particle history, and they can be used to retrieve and process data regarding the event.

- ***G4UserStackingAction***

The methods belonging to this class are invoked at the start of each history, when a new track is pushed onto the stack and when the stack becomes empty. They allow the user to control the various track stacking mechanisms.

- ***G4UserTrackingAction***

A track is not a collection of steps, but it is a snapshot of the state of a particle and it contains information about its current state, accessible through the methods of the *G4UserTrackingAction* class at the beginning or at the end of each trajectory. No information about the previous states can be retrieved from the *G4Track* object. A track is deleted when the particle loses all its kinetic energy and no at rest processes can occur, either when it goes out of the World or when it is artificially killed by the user.

- ***G4UserSteppingAction***

The step is the basic unit of the simulation and it consists of two points (a pre-step point and a post-step point), represented by the *G4Step* class. At the beginning of each step, all the processes the particle has access to are interrogated and the one which occurs on the shortest distance takes place. This is done by extracting random values from a series of probability distributions describing the likelihood for each process. The values can be expressed in terms of a distance to run before the process takes place.

The invocation of the *G4UserSteppingAction* class methods allow accessing to information about local values of energy, momentum, position, current volume, etc. related to the current step.

### 3.1.4 Executing the simulation

Geant4 provides three ways for executing a simulation:

- **"Pure hard-code" batch mode:** the parameters are fixed and in order to change them the simulation needs to be recompiled.
- **Batch mode with macro file:** A macro contains the parameters and it is passed to the simulation when the program is called. In this way, the parameters can be changed in the macro file and the simulation does not need to be recompiled.
- **Interactive mode:** It provides a graphic interface for the geometry, equipped with a command line where the parameters can be passed to the simulation. The commands are the same as those written in the macro file. This mode can be used in order to test the geometry and the progress of a simulation during the run.

These three modes must be specified with appropriate instructions in the *main()* function.

### 3.2 Particle In Cell (PIC) simulation

In this Section, one of the most popular numerical tools for the description of plasma is briefly presented: the Particle-in-Cell (PIC) method. The interested reader can find a more comprehensive description in [57, 58].

The Particle-in-Cell is a method to solve simultaneously the equation governing the evolution of the distribution function  $f_i(\mathbf{x}, \mathbf{v}, t)$  and the Maxwell equations for the electromagnetic field. So the starting point is the introduction of the so-called phase space distribution function  $f_i(\mathbf{x}, \mathbf{v}, t)$ , defined as the number density per unit element in phase space (or equivalently, the probability to find a particle in the infinitesimal volume  $d\mathbf{x}d\mathbf{v}$  around the  $(\mathbf{x}, \mathbf{v})$  point). The subscript  $i$  refers to the  $i$ -population of particles (electron, protons, etc.).

Under the hypothesis of collisionless plasma, the evolution of the distribution function is given by the relativistic Vlasov equation:

$$\frac{\partial f_i}{\partial t} + \mathbf{v} \cdot \frac{\partial f_i}{\partial \mathbf{x}} - q_i \left( \mathbf{E} + \frac{1}{c} \mathbf{v} \times \mathbf{B} \right) \cdot \frac{\partial f_i}{\partial \mathbf{p}} = 0 \quad (3.1)$$

where  $q_i$  and  $m_i$  are the electric charge and mass of the particles belonging to the  $i$ -population,  $\mathbf{v}$  is the velocity,  $\mathbf{p} = m\gamma\mathbf{v}$  is the momentum with  $\gamma = \sqrt{1 + \mathbf{p}(t) \cdot \mathbf{p}(t)/m^2c^2}$ ,  $\mathbf{E}$  and  $\mathbf{B}$  are the electric and magnetic fields.

The PIC method is based on the idea of representing the distribution function  $f_i$  of each population by a collection of *macro-particles*, each of which is representative of a certain number of real particles. Alongside this Lagrangian approach for particles, the electromagnetic field is calculated with an Eulerian approach on a finite grid.

The current density associated with the macro-particles is deposited at grid points, on which the magnetic field is then calculated. From the grid points, the Lorentz force acting on each superparticle is evaluated by interpolation and it is used to solve the equation of motion. This procedure is repeated iteratively. In a PIC simulation, the distribution function of each species is approximated with a sum of macro-particles  $f_j(\mathbf{x}, \mathbf{v}, t)$ :

$$f_i(\mathbf{x}, \mathbf{v}, t) \approx \sum_{j=1}^M f_j(\mathbf{x}, \mathbf{v}, t) \quad (3.2)$$

Each superparticle represents several physical particles, very close in the phase space. The approximation 3.2 is more valid as the volume occupied by the superparticle in the phase space  $\Delta\mathbf{x}\Delta\mathbf{v}$  is smaller.

The PIC method is based on the assignment to each superparticle of a certain functional form that depends on a set of time dependent and unknown parameters. Solving the Vlasov equation means finding this temporal dependence. If two parameters are used for each spatial dimension, they will be the position  $\mathbf{x}_j(t)$  and the speed  $\mathbf{v}_j(t)$  of the superparticle.

In general,  $f_j(\mathbf{x}, \mathbf{v}, t)$  is assumed to be punctual in the velocity space (so  $\Delta \mathbf{v} = \delta \mathbf{v}$ ), while, in the configuration space, it has a finite extension (in order to reduce the numerical noise in the simulation) described by the shape function  $S$  (see fig. 3.2):

$$f_j(\mathbf{x}, \mathbf{v}, t) = f_0 \delta(\mathbf{v} - \mathbf{v}_j(t)) S(\mathbf{x} - \mathbf{x}_j(t)) \quad (3.3)$$

where  $f_0$  is a normalization constant. A possible form for  $S$  is a triangular function in 1-D, while in 3-D is the product of three triangular functions.

Substituting 3.3 in 3.1 and making some manipulations, the final results are the equations of motion for the macro-particles:

$$\frac{\partial \mathbf{x}_j(t)}{\partial t} = \frac{\mathbf{v}_j(t)}{\gamma_j(t) m} \quad (3.4)$$

$$\frac{\partial \mathbf{p}_j(t)}{\partial t} = q \int S(\mathbf{x} - \mathbf{x}_j(t)) \left[ \mathbf{E}(\mathbf{x}, t) + \frac{\mathbf{p}_j(t)}{\gamma_j m c} \times \mathbf{B}(\mathbf{x}, t) \right] d\mathbf{x} \quad (3.5)$$

So, each macro-particle moves under the effect of the Lorentz force averaged over its volume and as if it had a mass  $m$ .

In order to solve the motion of the macro-particles an iterative algorithm is needed. The most widely used is the so called Boris Pusher algorithm, a leapfrog method in which positions and momenta of the macro-particles are known respectively at integer and half-integer times.

On the other side, in order to solve numerically the Maxwell equations and find the electromagnetic field, a Maxwell solver is employed. A very popular solver is second order FDTD (Finite Difference Time Domain) method on free lattice. Finally, it is emphasized that every PIC simulation can be considered as a sequence of steps in which the main quantities are updated at each step, both for plasma (positions and momenta of all macro-particles) and electromagnetic field at the grid nodes.

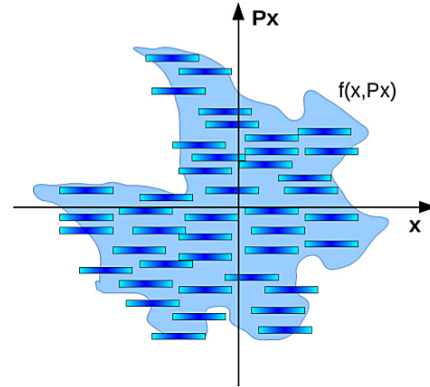


**Figure 3.2:** Sampling of the distribution function with macro-particles. Each macro-particle has a definite momentum, but is extended in space.



## Chapter 4

# PIXE analysis with laser-driven proton sources

The formalism described in Sec. 2.2 is suitable to model PIXE when monoenergetic protons are employed. These models are the conceptual basis for the development of the iterative codes necessary to perform the analysis.

This Chapter, in particular Sec. 4.1, describes the extension of the models presented in Sec. 2.2 for laser driven proton sources (characterized by a broad exponential spectrum). The resulting new models are employed to develop iterative codes with Matlab (in Appendix C, block diagrams of the codes are reported). Also in this case, their purpose is to provide the sample composition starting from the values of the X-ray yields.

In Sec. 4.2.5 a series of Monte Carlo simulations have been carried out aimed to produce results of "synthetic Laser-driven PIXE experiments". The outputs, in terms of the X-ray yields, will be employed to test the developed models. The simulations and the analysis of the outputs are performed both for monoenergetic protons and for protons with an exponential spectrum. The goal is to compare the results obtained through the two different sources.

### 4.1 PIXE modeling for non-monoenergetic protons

Different kinds of samples have been considered, starting from the simplest and arriving to the more complex one. In the case of thin targets (Sec. 2.2.1) and thick homogeneous (Sec. 2.2.2) targets, the evaluation of the elemental concentrations is the goal of the analysis. Also, the case of the multilayer target (Sec. 2.2.3) has been treated, in which the layer thicknesses are the unknowns. The fourth case involves the derivation of the concentration profiles of a completely generic sample (Sec. 2.2.4).

It is recalled that all the quantities which appear in the following models can be retrieved from the databases reported in Sec. C.0.2.

### 4.1.1 Thin target

The starting point of this procedure is to consider a generic shape for the incident proton spectrum. This will allow the model to be more generic as possible and, in principle, applicable to any kind of non-monoenergetic proton source.

The terms in the expression of the yield which are proton energy-dependent are the number of incident protons  $N_p(E_p)$  and the value of the ionization cross section  $\sigma_j(E_p)$ . The number of X-rays  $dY_j$  associated to the presence of the  $j$ -th element and generated by the incident protons with energy between  $E_p$  and  $E_p + dE_p$  is

$$dY_j(E_p) = n(E_p) \frac{\Delta\Omega}{4\pi} \varepsilon_j \frac{W_j N_{av}}{M_j} \rho_{comp} t'_j \sigma_j(E_p) \omega_j dE_p \quad (4.1)$$

Most of the terms that appear in eq. 4.1 were specified for eq. 2.4 of Sec. 2.2.1, except for  $n_p$ .  $n_p$  is the number of protons per unit energy, expressed as the product of the total number of protons  $N_p$  multiplied by a *shaping function*  $f_p(E_p)$ :

$$n(E_p) = \frac{dN_p(E_p)}{dE_p} = N_p f_p(E_p) \quad \text{with} \quad \int f_p(E_p) dE_p = 1 \quad (4.2)$$

A first quantity of interest in the analysis is the differential yield  $\frac{1}{N_p} \frac{dY_j}{dE_p}$  normalized with respect to the total number of protons. It can be derived combining eq. 4.1 and eq. 4.2:

$$\frac{1}{N_p} \frac{dY_j(E_p)}{dE_p} = f_p(E_p) \frac{\Delta\Omega}{4\pi} \varepsilon_j \frac{W_j N_{av}}{M_j} \rho_{comp} t'_j \sigma_j(E_p) \omega_j \quad (4.3)$$

The total yield, normalized with respect to the total number of protons  $N_p$  and associated to the whole proton energy spectrum, is given by the integration of eq. 4.3 from the minimum  $E_{p,min}$  to the maximum  $E_{p,max}$  energy of the spectrum:

$$\frac{Y_j}{N_p} = \frac{\Delta\Omega}{4\pi} \varepsilon_j \frac{W_j N_{av}}{M_j} \rho_{comp} t'_j \int_{E_{p,min}}^{E_{p,max}} f_p(E_p) \sigma_j(E_p) \omega_j dE_p \quad (4.4)$$

Starting from this expression and considering eq. 2.5 of Sec. 2.2.1 for the effective thickness  $t'$ , it is now possible to elaborate a procedure to retrieve the composition of a thin target from experimental x-ray yields.

In the case of a laser-driven proton energy spectrum,  $f_p(E_p)$  can be modeled, as a first approximation, as a normalized exponential function characterized by a given *temperature*  $\alpha > 0$ :

$$f_p(E_p) = \begin{cases} \frac{e^{-\alpha E_p}}{\int_{E_{p,min}}^{E_{p,max}} e^{-\alpha E_p} dE_p} & \text{for } E_{p,min} \leq E_p \leq E_{p,max} \\ 0 & \text{for } E_p < E_{p,min} \cup E_p > E_{p,max} \end{cases}$$

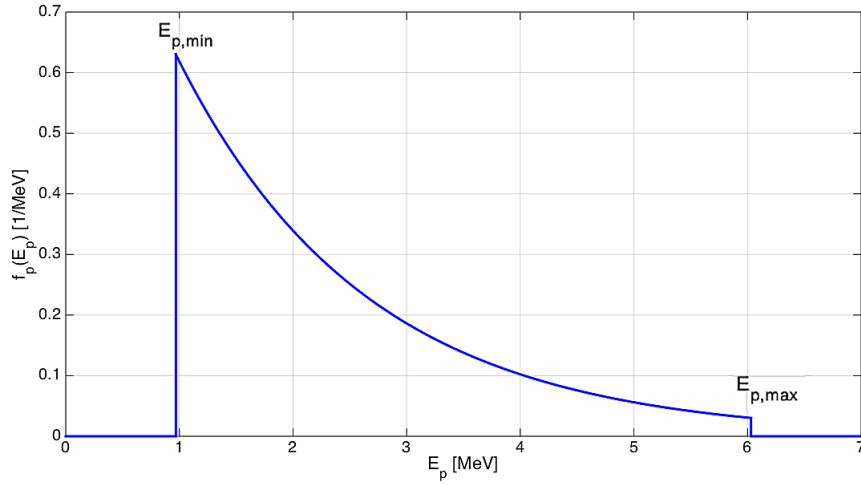


**Figure 4.1:** Example of shaping function with temperature  $\alpha = 0.6 \text{ MeV}^{-1}$ ,  $E_{p,min} = 1 \text{ MeV}$  and  $E_{p,max} = 6 \text{ MeV}$ .

where  $E_{p,max}$  and  $E_{p,min}$  are the maximum (cut-off) and minimum energies in the spectrum (an example is reported in fig. 4.1).

The iterative process is essentially the same as the one described in Sec. 2.2.1. At each iteration, a new set of concentration values  $W_j$  is considered and the associated effective thickness  $t'$  is updated. From eq. 4.3, the differential yield is evaluated and an example is reported in fig. 4.2. Next, the differential yield  $dY_j$  is integrated in order to obtain the total yield  $Y_j$ . The experimental

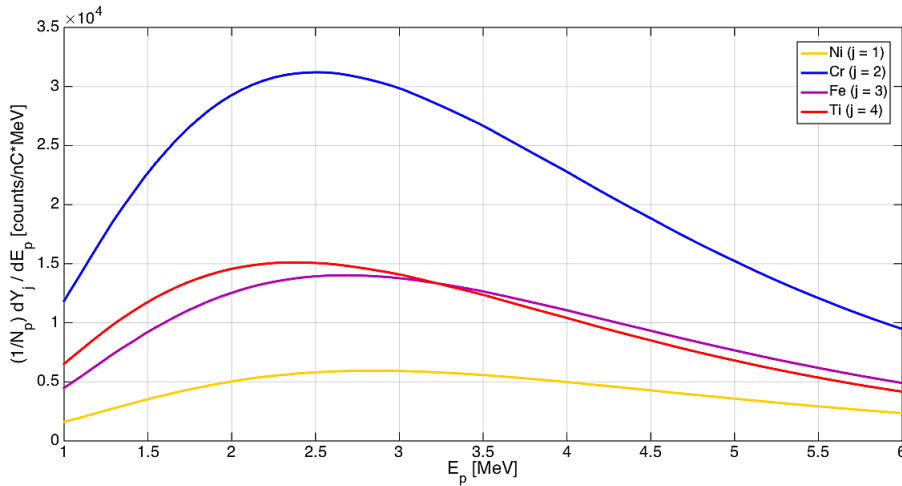


**Figure 4.2:** Differential yields for a thin target ( $1\mu\text{m}$ ) composed by 20% of Ni, 40% of Cr, 30% of Fe and 10% of Ti. The shaping function is the same reported in the fig. 4.1 and the X-ray lines considered are 7.46 keV for Ni, 5.41 keV for Cr, 6.4 keV for Fe and 4.51 keV for Ti.

measurements provide the values of the X-ray yields for each element, so a system of equations like 4.4 can be written and solved iteratively. This implies searching for the values of the elemental concentrations  $W_j$  that minimize the  $\chi$ -parameter:

$$\chi = \left( \sum_{j=1}^J \left( \frac{Y_{j,exp}}{\langle Y_{j,exp} \rangle_{max}} - \frac{Y_{j,th}}{\langle Y_{j,th} \rangle_{max}} \right)^2 \right)^{1/2} \quad (4.5)$$

where  $Y_{j,exp}$  and  $Y_{j,th}$  are the experimental and theoretical values of the X-ray yields, while  $\langle Y_{j,exp} \rangle_{max}$  and  $\langle Y_{j,th} \rangle_{max}$  are the corresponding maximum values among those available.

It is worth to remind that the values of  $t'_j$  need to be re-evaluated at each iteration because they depend upon the elemental composition through the X-ray mass attenuation coefficients, as explained in Sec. 2.2.1. The research of the minimum of the  $\chi$ -parameter is done employing Matlab function *fmincon* [67].

#### 4.1.2 Thick homogeneous target

Here, the model describing the case of a thick homogeneous target (Sec. 2.2.2) is extended in order to include the presence of a non-monoenergetic proton spectrum. Again, the starting point is the equation for the number of X-rays generated by the incident protons with energy between  $E_p$  and  $E_p + dE_p$ :

$$dY_j(E_p) = n_p(E_p) \frac{\Delta\Omega}{4\pi} \varepsilon_j W_j \frac{N_{av}}{M_j} \times \int_0^{\rho R(E_p)} \sigma_j((\rho r)_{E_p}) \omega_j \exp^{-\left(\frac{\mu}{\rho}\right)_j \frac{(\rho r)_{E_p}}{\cos\theta}} d(\rho r)_{E_p} dE_p \quad (4.6)$$

As reported in Sec. 2.2.2 for eq. 2.12, the proton slowdown is accounted by the integral along the path of the cross section and the X-ray attenuation. All terms which appear in eq. 4.6 are defined in Sec. 2.2.1. Substituting eq. 4.2 inside eq. 4.6, the differential yield normalized with respect to  $N_p$  can be expressed as:

$$\frac{1}{N_p} \frac{dY_j(E_p)}{dE_p} = f_p(E_p) \frac{\Delta\Omega}{4\pi} \varepsilon_j W_j \frac{N_{av}}{M_j} \times \int_0^{\rho R(E_p)} \sigma_j((\rho r)_{E_p}) \omega_j \exp^{-\left(\frac{\mu}{\rho}\right)_j \frac{(\rho r)_{E_p}}{\cos\theta}} d(\rho r)_{E_p} \quad (4.7)$$

From eq. 4.7, integrating over the proton spectrum energy  $E_p$ , the total yield  $Y_j$  reads as follow:

$$\frac{Y_j}{N_p} = \frac{\Delta\Omega}{4\pi} \varepsilon_j W_j \frac{N_{av}}{M_j} \int_{E_{p,min}}^{E_{p,max}} f_p(E_p) \times \int_0^{\rho R(E_p)} \sigma_j((\rho r)_{E_p}) \omega_j \exp^{-\left(\frac{\mu}{\rho}\right)_j \frac{(\rho r)_{E_p}}{\cos\theta}} d(\rho r)_{E_p} dE_p \quad (4.8)$$

Note that both the total range  $\rho R(E_p)$  and, more in general, the proton path  $(\rho r)_{E_p}$  depend on the initial proton energy  $E_p$  and they can be evaluated with eq. 2.13 through the stopping power  $S(E)$ . As far as X-rays attenuation is concerned, the attenuation coefficients  $(\mu/\rho)_j$  are calculated with eq. 2.9.

The iterative procedure employed to retrieve mass concentrations  $W_j$  starts considering the initial proton energy spectrum (fig. 4.1) and a sufficiently fine discretization of the shaping function  $f_p(E_p)$ . Then, each discrete value of the energy  $E_p$  between  $E_{p,max}$  and  $E_{p,min}$  is used as starting point to evaluate the energy of the primary particles  $E(\rho r)$  as a function of the position inside the material over the whole range inside the target. This can be done inverting the function  $(\rho r)_{E_p}(E)$  evaluated from eq. 2.13 assuming an arbitrary initial set of concentrations  $W_j$ . An example of the function  $E(\rho r)$  considering five different discrete values of  $E_p$  is shown in fig. 4.3.

Now, for each value of  $E_p$ , the function  $E(\rho r)$  is employed to derive the expres-

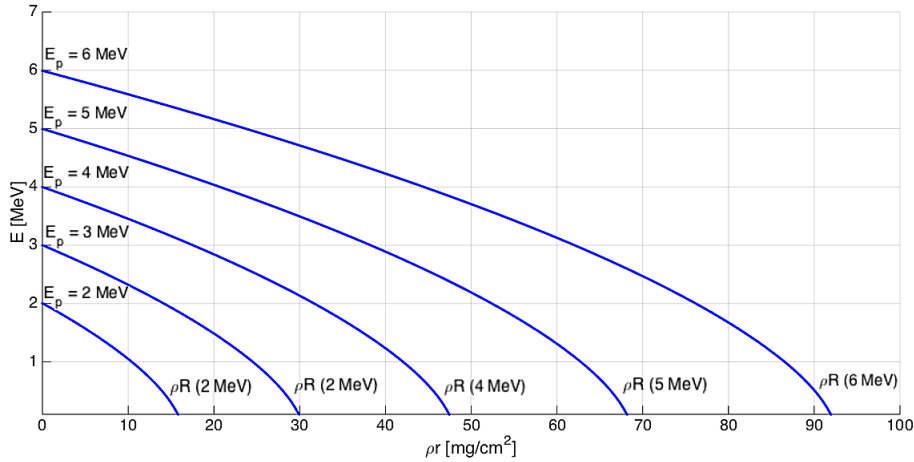


**Figure 4.3:**  $E(\rho r)$  for  $E_p = 2, 3, 4, 5$  and  $6$  MeV slowing down in a thick target composed by 40% of Ni, 30% of Cr and 30% of Mo.

sion of the ionization cross section  $\sigma((\rho r)_{E_p})$  from  $\sigma(E)$ . Then, the second term of eq. 4.7 is evaluated. This procedure allows to find a discrete set of values reproducing the differential yield  $\frac{1}{N_p} \frac{dY_j(E_p)}{dE_p}$  (an example is shown in fig. 4.4). Finally, integrating the differential yield over the proton energy spectrum  $E_p$  from the minimum value  $E_{p,min}$  to the maximum one  $E_{p,max}$ , the total yield  $\frac{Y_j}{N_p}$  can be obtained.

This procedure describes how the theoretical values  $Y_{j,th}$  are calculated. Then, the iterative process which provides the values of  $W_j$  is identical to that described for the monoenergetic case (Sec. 2.2.2).

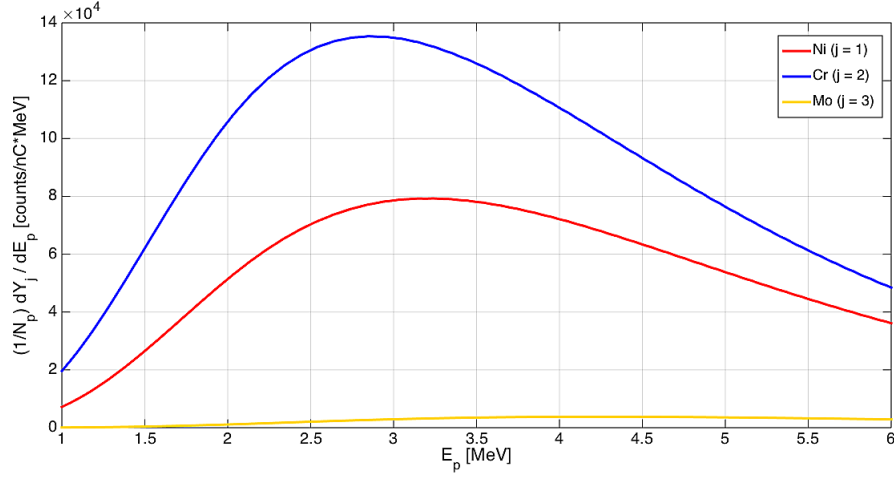


**Figure 4.4:** Differential yields for thick target composed by 20% of 40% of Ni, 30% of Cr and 30% of Mo. The shaping function is the same reported in 4.1 and the X-ray lines considered are 7.46 keV for Ni, 5.41 keV for Cr and 17.4 keV for Mo.

#### 4.1.3 Multilayer target

Here, the model describing the case of a multilayer target (Sec. 2.2.3) is extended in order to include the presence of a non-monoenergetic proton spectrum. The expression for  $dY_j(E_p)$  must consider the presence of the different layers:

$$dY_j(E_p) = n_p(E_p) \frac{\Delta\Omega}{4\pi} \varepsilon_j \frac{N_{av}}{M_j} \times \sum_{l=1}^{L-1} W_{j,l} P_{j,l} \int_{\rho R_l}^{\rho R_{l+1}} \sigma_j((\rho r)_{E_p}) \omega_j e^{-\left(\frac{\mu}{\rho}\right)_{j,l} \frac{(\rho r)_{E_p}}{\cos\theta}} d(\rho r)_{E_p} dE_p \quad (4.9)$$

$$P_{j,l} = \sum_{t=1}^{l-1} e^{-\left(\frac{\mu}{\rho}\right)_{j,t} \frac{\rho R_t - \rho R_{t-1}}{\cos\theta}} \quad (4.10)$$

Again, most of the terms in the equation are described in detail in Sec. 2.2.1 and Sec. 2.2.3. So, as for the monoenergetic case, the yield  $dY_j(E_p)$  is given by the sum of the different contributions over each layer (index  $l$ ). These contributions are represented by the direct X-ray production (the integral of the cross section between the layer interfaces  $\rho R_l$  and  $\rho R_{l+1}$ ) and by the X-ray attenuation in the previous layers (the  $P_{j,l}$  term given by eq. 4.10). It is worth to remind that the exponential term inside the integral takes into account the X-ray attenuation in the current layer.

Substituting eq. 4.2 inside eq. 4.9, the differential yield normalized with respect

to the total number of protons  $N_p$  can be expressed as:

$$\frac{1}{N_p} \frac{dY_j(E_p)}{dE_p} = f_p(E_p) \frac{\Delta\Omega}{4\pi} \varepsilon_j \frac{N_{av}}{M_j} \times \sum_{l=1}^{q-1} W_{j,l} P_{j,l} \int_{\rho R_l}^{\rho R_{l+1}} \sigma_j((\rho r)_{E_p}) \omega_j e^{-\left(\frac{\mu}{\rho}\right)_{j,l} \frac{(\rho r)_{E_p}}{\cos\theta}} d(\rho r)_{E_p} \quad (4.11)$$

Integrating over the proton energy spectrum, the total yield can be written as follows:

$$\frac{Y_j}{N_p} = \frac{\Delta\Omega}{4\pi} \varepsilon_j \frac{N_{av}}{M_j} \int_{E_{p,min}}^{E_{p,max}} f_p(E_p) \times \sum_{l=1}^{q-1} W_{j,l} P_{j,l} \int_{\rho R_l}^{\rho R_{l+1}} \sigma_j((\rho r)_{E_p}) \omega_j e^{-\left(\frac{\mu}{\rho}\right)_{j,l} \frac{(\rho r)_{E_p}}{\cos\theta}} d(\rho r)_{E_p} dE_p \quad (4.12)$$

In order to account for the proton slowing down  $(\rho r)_{E_p}(E)$  inside the sample, the different composition  $W_{j,l}$  and interfaces  $\rho R_l$  of the layers must be considered. This can be done with eq. 2.17.

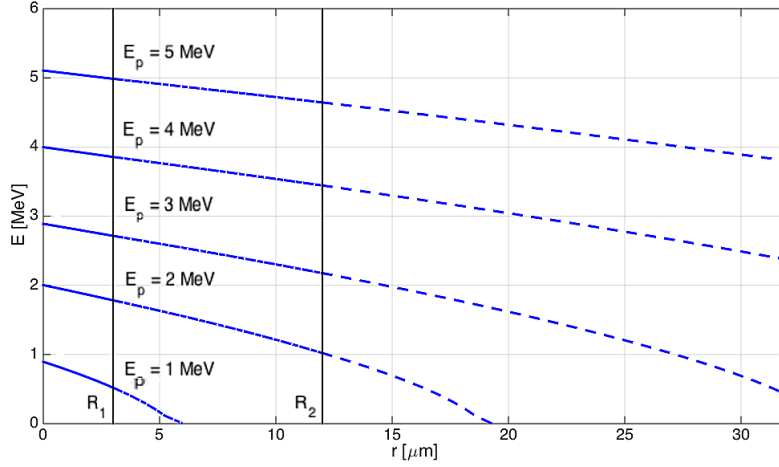


**Figure 4.5:**  $E(\rho r)$  for  $E_p = 1, 2, 3, 4$  and  $5$  MeV protons slowing down in a multilayer target composed by 20% of Ni and 80% of Mo for the first  $3 \mu\text{m}$  layer, 40% of Ni and 60% of Cr for the second  $9 \mu\text{m}$  layer, 30% of Cr and 70% of Mo for the third  $17 \mu\text{m}$  layer. The shaping function is the same reported in fig. 4.1 and the considered X-ray lines are 7.46 keV for Ni, 5.41 keV for Cr and 17.4 keV for Mo.

As far as the numerical implementation is concerned, the procedure in order to find the total yield normalized with respect to the total number of protons is almost the same described at the end of the Sec. 4.1.2: given a set of values for the layer interfaces  $\rho R_l$  (the densities  $W_{j,l}$  are assumed to be known a priori) and

starting from a sufficiently fine discretization for the incident proton spectrum energies  $E_p$ , it is possible to evaluate the total yields  $Y_j/N_p$ .

Fig. 4.5 shows an example of  $(\rho r)_{E_p}(E)$  for a three layer structure considering five different initial proton energies.

The iterative procedure is intended to find the set of unknowns, in this case the layer interfaces  $\rho R_l$ , which minimizes the  $\chi$ -parameter expressed as eq. 4.5, starting from the experimental yields.

#### 4.1.4 Generic non-homogeneous target

The models developed in sections Sec. 4.1.1, 4.1.2 and 4.1.3 are concerned to PIXE scenarios with laser-driven protons that require in principle a single proton bunch (or a sequence of identical bunches to improve the signal). Similarly, the corresponding monoenergetic cases described in Sec. 2.2.1, 2.2.2 and 2.2.3 require the use of only one proton beam with fixed energy.

Consider now the fourth case described in Sec. 2.2.4. In order to obtain the concentration profiles for the elements in a completely generic and unknown sample, it is necessary to employ a certain number of proton beams characterized by different proton energies. The purpose of this section is to extend the model for this kind of analysis, to include the presence of a non-monoenergetic spectrum. Conceptually, this can be done following two different strategies:

- As in the monoenergetic case, more than one measurement can be done. But instead of changing the proton energy, the proton spectrum parameters (maximum energy and temperature) can be modified. This is experimentally possible by changing the laser energy. So, for each proton bunch, a different X-ray spectrum is recorded.
- In order to open up to the possibility of performing the analysis with a single shot, the proton energy spectrum must be divided into different energy intervals and the X-rays associated to each slice must be recorded separately. This in principle could be done by exploiting the peculiar properties of a bunch of laser-driven protons.

The protons are emitted approximately at the same time from the source but, since they have a broad energy spectrum (and thus a broad velocity distribution), the bunch undergoes a temporal broadening (the faster projectiles will arrive before, the slower ones will arrive later). Considering distances of cm there is a delay in the order of ns, which very long compared to the time necessary for the atoms to emit the X-rays. Thus X-rays emitted in a given time window corresponds to protons within a given energy window. Of course, this requires a detection system sufficiently fast to collect separately the X-rays coming during different intervals of time. In practice, it would be necessary an array of detectors with a very fast gating so that they can be activated in sequence.



The first scenario is the simplest from an experimental point of view, although it requires good control of the proton source. We start by considering the first case. Assume to have a sample composed of  $J$  elements (index  $j$ ) distributed following an unknown concentration profile. The  $N$  proton energy spectra (index  $k$ ) are characterized by different cut-off values  $E_{p,max}^k$ , temperatures  $\alpha^k$  and total number of protons  $N_p^k$ . The sample is split into  $L$  sub-layers (index  $l$ ) of thickness  $R_l - R_{l-1}$  for which a uniform and unknown elemental composition is assumed.

The yield  $dY_j^k$  associated to a certain element and generated by protons with energy between  $E_p$  and  $E_p + dE_p$  belonging to the  $k$ -th proton bunch is:

$$dY_j^k(E_p) = n_p^k(E_p) \frac{\Delta\Omega}{4\pi} \varepsilon_j \frac{N_{av}}{M_j} \times \sum_{l=1}^{L-1} W_{j,l} P_{j,l} \int_{\rho R_l}^{\rho R_{l+1}} \sigma_j((\rho r)_{E_p}) \omega_j e^{-\left(\frac{\mu}{\rho}\right)_{j,l} \frac{(\rho r)_{E_p}}{\cos\theta}} d(\rho r)_{E_p} dE_p \quad (4.13)$$

$$P_{j,l} = \sum_{t=1}^{l-1} e^{-\left(\frac{\mu}{\rho}\right)_{j,t} \frac{\rho R_t - \rho R_{t-1}}{\cos\theta}} \quad (4.14)$$

This relation is essentially equal to eq. 4.9, except for the index  $k$ . Also, the differential yield has exactly the same form as eq. 4.11 and it is the result of the combination of eq. 4.13 and eq. 4.2:

$$\frac{1}{N_p^k} \frac{dY_j^k(E_p)}{dE_p} = f_p^k(E_p) \frac{\Delta\Omega}{4\pi} \varepsilon_j \frac{N_{av}}{M_j} \times \sum_{l=1}^{L-1} W_{j,l} P_{j,l} \int_{\rho R_l}^{\rho R_{l+1}} \sigma_j((\rho r)_{E_p}) \omega_j e^{-\left(\frac{\mu}{\rho}\right)_{j,l} \frac{(\rho r)_{E_p}}{\cos\theta}} d(\rho r)_{E_p} \quad (4.15)$$

Integrating over the  $k$ -th proton energy spectrum, the total yield results:

$$\frac{Y_j^k}{N_p^k} = \frac{\Delta\Omega}{4\pi} \varepsilon_j \frac{N_{av}}{M_j} \int_{E_{p,min}}^{E_{p,max}^k} f_p^k(E_p) \times \sum_{l=1}^{L-1} W_{j,l} P_{j,l} \int_{\rho R_l}^{\rho R_{l+1}} \sigma_j((\rho r)_{E_p}) \omega_j e^{-\left(\frac{\mu}{\rho}\right)_{j,l} \frac{(\rho r)_{E_p}}{\cos\theta}} d(\rho r)_{E_p} dE_p \quad (4.16)$$

which is of course very similar to eq. 4.12. It is only recalled that the only difference is the presence of the  $k$ -th index, which identifies the measurement or, equivalently, the proton energy spectrum.

Now consider the second case and assume to replace the  $N$  proton bunches with a single bunch whose spectrum is subdivided into  $N$  energy bins. Here, the

index  $k$  identifies those energy intervals and the equation for the associated X-ray yields  $\frac{Y_j^k}{N_p^k}$  remains practically unchanged, except for the integration interval over the proton energy:

$$\frac{Y_j^k}{N_p^k} = \frac{\Delta\Omega}{4\pi} \varepsilon_j \frac{N_{av}}{M_j} \int_{\Delta E_p^k} f_p(E_p) \times \sum_{l=1}^{L-1} W_{j,l} P_{j,l} \int_{\rho R_l}^{\rho R_{l+1}} \sigma_j((\rho r)_{E_p}) \omega_j e^{-\left(\frac{\mu}{\rho}\right)_{j,l} \frac{(\rho r)_{E_p}}{\cos\theta}} d(\rho r)_{E_p} dE_p \quad (4.17)$$

Note that the shaping function  $f_p$  no longer has the index  $k$ , because the energy intervals belong to the same proton energy spectrum. An example of spectrum divided into energy intervals is shown in fig. 4.6.

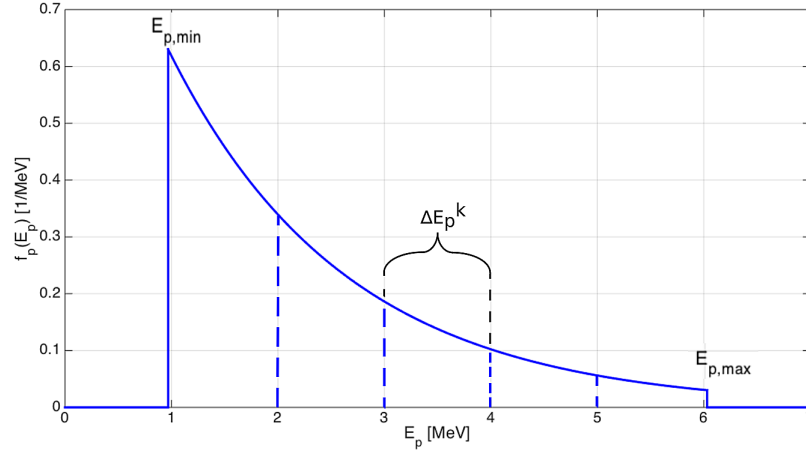


**Figure 4.6:** Exponential proton energy spectrum with temperature  $\alpha = 0.6 \text{ MeV}^{-1}$ ,  $E_{p,min} = 1 \text{ MeV}$  and  $E_{p,max} = 6 \text{ MeV}$ , subdivided into energy intervals.

Summarizing, there are  $J \times N$  eq. 4.16 or 4.17 (one for each  $j$ -th element and each  $k$ -th proton energy spectrum or interval). Subdividing the target into  $L$  sub-layers, there are  $L \times J$  unknown concentrations  $W_{j,l}$ . So, if the number of proton bunches or energy intervals  $N$  is larger to the number of fictitious sub-layers  $L$ , the system can be solved in order to find the values of  $W_{j,l}$  for each layer which best approximate the real profile. The iterative procedure applicable in order to solve the system has already been explained for the monoenergetic case in Sec. 2.2.4 and the extension to the non-monoenergetic case is straightforward. Taking the second case as an example, the system of equations 4.17 can be

written more concise by grouping some terms:

$$Y_j^{k*} = \frac{Y_j^k M_j}{N_p^k \varepsilon_{x_j}} \quad (4.18)$$

$$A = \frac{\Delta\Omega}{4\pi} N_{av} \quad (4.19)$$

$$T_{j,l}^k = P_{j,l} \int_{\rho R_l}^{\rho R_{l+1}} \sigma_{x_j}((\rho r)_{E_p}) \omega_j e^{-\left(\frac{\mu}{\rho}\right)_{j,l} \frac{(\rho r)_{E_p}}{\cos\theta}} d(\rho r)_{E_p} dE_p \quad (4.20)$$

So, the system can be expressed in this concise way:

$$Y_j^{k*} = A \int_{\Delta E_p^k} f_p(E_p) \left[ \sum_{i=1}^Z T_{j,l}^k W_{j,l} \right] dE_p \quad (4.21)$$

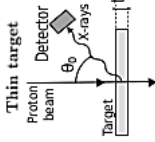
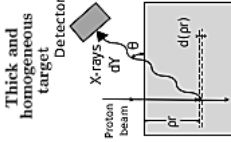
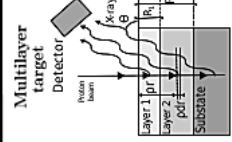
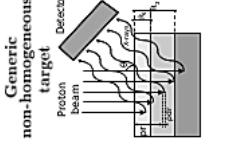
Target type	Goal of the analysis	Known parameters	Yield equation (monoenergetic)	Yield equation (non-monoen.)
 <p>Thin target Proton beam Detector <math>\theta_0</math> x-rays Target t</p>	Mass concentrations $W_j$	Thickness $t$	$\frac{Y_j}{N_p} = \frac{\Delta\Omega}{4\pi} \varepsilon_j W_j \frac{N_{av}}{M_j} \rho_{comp} t^2 \sigma_j(E_0) \omega_j$	$\frac{Y_j}{N_p} = \frac{\Delta\Omega}{4\pi} \varepsilon_j \frac{N_{av}}{M_j} \rho_{comp} t^2 \int_{E_p, min}^{E_p, max} f_p(E_p) \sigma_j(E_p) \omega_j dE_p$
 <p>Thick and homogeneous target Detector x-rays Proton beam <math>\theta</math> <math>\frac{d(p,r)}{dr}</math> r</p>	Mass concentrations $W_j$	Thickness $R$	$\frac{Y_j}{N_p} = \frac{\Delta\Omega}{4\pi} \varepsilon_j W_j \frac{N_{av}}{M_j} \int_0^{pR} \sigma_j(pR) \omega_j \exp^{-\left(\frac{t}{\rho R}\right) \frac{pR}{\cos\theta}} d(pR)$	$\frac{Y_j}{N_p} = \frac{\Delta\Omega}{4\pi} \varepsilon_j W_j \frac{N_{av}}{M_j} \int_{E_p, min}^{E_p, max} f_p(E_p) \times \int_0^{pR(E_p)} \sigma_j((pR) E_p) \omega_j \exp^{-\left(\frac{t}{\rho R}\right) \frac{pR(E_p)}{\cos\theta}} d(pR) E_p dE_p$
 <p>Multilayer target Detector x-rays Proton beam <math>\theta</math> Layer 1 Layer 2 Substrate <math>R_1</math> <math>R_2</math></p>	Layer interface positions $R_l$	Mass concentrations $W_{j,l}$	$\frac{Y_j}{N_p} = \frac{\Delta\Omega}{4\pi} \varepsilon_j W_j \frac{N_{av}}{M_j} \sum_{l=1}^{l-1} W_{j,l} P_{j,l} \int_{\rho R_l}^{\rho R_{l+1}} \sigma_j(pR) \omega_j \exp^{-\left(\frac{t}{\rho R}\right) \frac{\rho R}{\cos\theta}} d(pR)$ $P_{j,l} = \sum_{k=1}^{l-1} e^{-\left(\frac{t}{\rho R}\right) \frac{\rho R_k - \rho R_{k-1}}{\cos\theta}}$	$\frac{Y_j}{N_p} = \frac{\Delta\Omega}{4\pi} \varepsilon_j \frac{N_{av}}{M_j} \int_{E_p, min}^{E_p, max} f_p(E_p) \times \sum_{l=1}^{l-1} W_{j,l} P_{j,l} \int_{\rho R_l}^{\rho R_{l+1}} \sigma_j((pR) E_p) \omega_j \exp^{-\left(\frac{t}{\rho R}\right) \frac{\rho R(E_p)}{\cos\theta}} d(pR) E_p dE_p$
 <p>Generic non-homogeneous target Detector x-rays Proton beam <math>\theta</math> Layer 1 Layer 2 Substrate <math>R_1</math> <math>R_2</math></p>	Mass concentrations $W_{j,l}$ Layer interface positions $R_l$		$\frac{Y_j^k}{N_p^k} = \frac{\Delta\Omega}{4\pi} \varepsilon_j W_j \frac{N_{av}}{M_j} \sum_{l=1}^l W_{j,l} P_{j,l} \int_{\rho R_l}^{\rho R_{l+1}} \sigma_j(pR) \omega_j \exp^{-\left(\frac{t}{\rho R}\right) \frac{\rho R}{\cos\theta}} d(pR)$ $P_{j,l} = \sum_{k=1}^{l-1} e^{-\left(\frac{t}{\rho R}\right) \frac{\rho R_k - \rho R_{k-1}}{\cos\theta}}$	$\frac{Y_j^k}{N_p^k} = \frac{\Delta\Omega}{4\pi} \varepsilon_j \frac{N_{av}}{M_j} \int_{E_p, min}^{E_p, max} f_p(E_p) \times \sum_{l=1}^{l-1} W_{j,l} P_{j,l} \int_{\rho R_l}^{\rho R_{l+1}} \sigma_j((pR) E_p) \omega_j \exp^{-\left(\frac{t}{\rho R}\right) \frac{\rho R(E_p)}{\cos\theta}} d(pR) E_p dE_p$

Figure 4.7: Summary of the analyzed cases for both monoenergetic protons (Sec. 2.2) and with an exponential energy spectrum (Sec. 4.1).

## 4.2 Monte Carlo simulation of PIXE data

The goal is to study the feasibility of PIXE with a laser-driven proton source. The idea is to test, for all the considered scenarios, the possibility to use the developed models to retrieve the characteristics of the targets from the X-ray yields. This must be done by applying the iterative codes, which constitute the implementation of the theoretical models themselves, to experimental data obtained from non-monoenergetic protons and known samples. The obtained results in terms of concentrations, thicknesses, or profiles can be compared to the actual composition of the targets.

For this thesis work, a Monte Carlo code (Geant4) was used to generate "synthetic experimental data". It considers all the physical processes that may occur under the experimental conditions studied. A Monte Carlo code rather than real experimental data was used since experimental investigation of laser-driven PIXE has been extremely limited so far (only a proof-of-principle experiment is reported in the literature [1]).

Moreover, in order to ascertain the accuracy of the Monte Carlo simulations, a case of PIXE analysis with monoenergetic protons present in literature [2] will be reproduced and the results compared.

### 4.2.1 Physics processes

In Geant4, each particle is followed with a sequence of steps characterized by different length depending on the mean free path (calculated considering all the possible physical processes).

As far as PIXE is concerned, the process of interest that can limit the step length is the ionization. If in a given step an ionization event occurs, a de-excitation involving the emission of a X-ray can take place.

Concerning the simulation of PIXE with Geant4, there are several papers in literature [63, 64, 65, 66] aimed to validate the dedicated physics libraries. According to these references, a high accuracy of electrons and hadrons tracking is required for PIXE simulations with Geant4. A suitable accuracy is obtained selecting the *G4EmStandardPhysics\_option3* constructor.

The production cut for all the secondary particles is set to  $0.5 \mu\text{m}$ . This implies that all secondary particles with low energy and whose range does not exceed the value of the cut are not created. This is to avoid unnecessary calculations, since some processes are characterized by infrared divergence causing huge CPU time.

Secondary charged particles are tracked taking into account Bremsstrahlung, ionization and multiple scattering, while photoelectric effect, Compton scattering and pair production are activated for photons.

Concerning the ionization cross sections, the *Energy-Loss Coulomb-Repulsion Perturbation-Stationary-State Relativistic Theory (ECPSSR)* model is employed.

### 4.2.2 Simulated experimental set-up

As regards to the set of simulations presented in this Chapter, the experimental set-up is very simple. A proton beam irradiates the target at normal angle and a detector of cylindrical shape oriented at  $45^\circ$  with respect to the proton beam direction is present.

Assuming a realistic configuration, the distance between the irradiated spot on the target and the face of the detector is 5 cm, while the detector diameter is equal to 4 cm. Then the solid angle subtended by the cylinder is 0.46 sr.

Both the target and the detector are placed in vacuum. The configuration is shown in fig. 4.8. Here the properties of the target (composition and thickness  $t$ ) are not reported, because the targets will be described specifically for each case when they are examined.

Two snapshots of running simulations are reported in the figures: protons (blue) are generated and directed towards the sample. The generated X-rays (green) are emitted isotropically and some of them reach the cylindrical detector. Fig. 4.9 shows the case of a simulation with monoenergetic protons characterized by a very low radial divergence angle, while fig. 4.10 pertains to the case of a simulation of protons with exponential energy spectrum and a larger divergence angle.

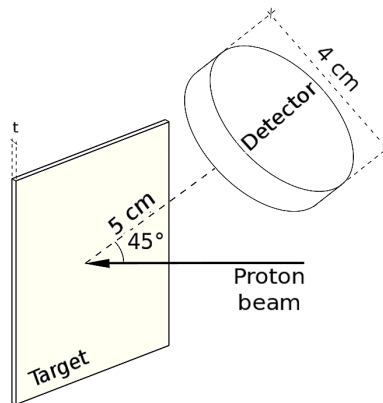


**Figure 4.8:** *Geometry set-up of Monte Carlo simulations.*

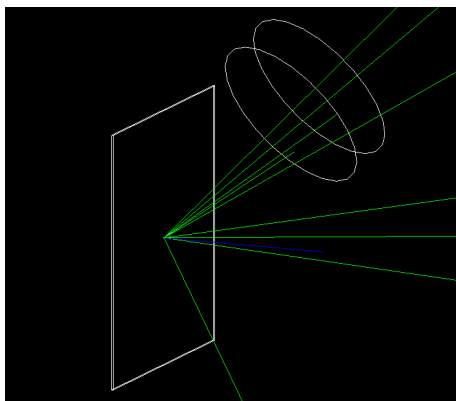


**Figure 4.9:** *Monte Carlo simulation of PIXE with monoenergetic proton beam.*

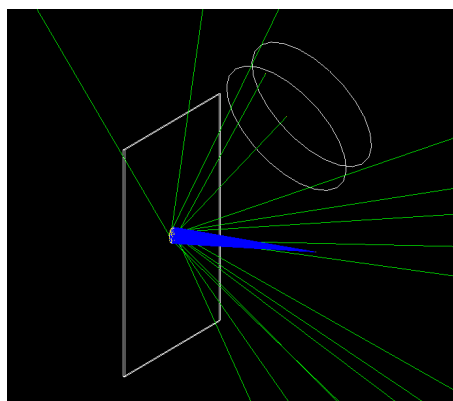


**Figure 4.10:** *Monte Carlo simulation of PIXE with an exponential proton energy spectrum.*

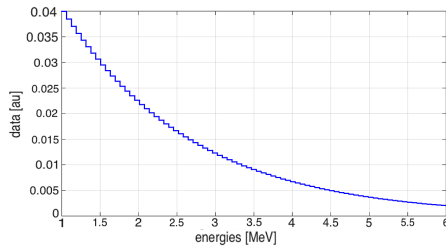


**Figure 4.11:** Example of a discrete probability distribution function for a proton energy spectrum with temperature  $\alpha = 0.6 \text{ MeV}^{-1}$ ,  $E_{p,max} = 6 \text{ MeV}$  and  $E_{p,min} = 1 \text{ MeV}$

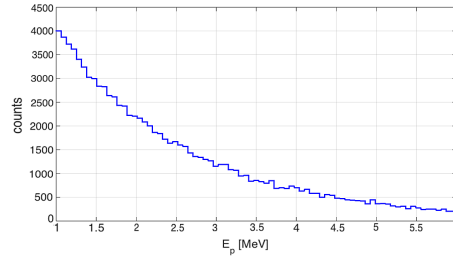


**Figure 4.12:** Example of an energy spectrum of  $10^5$  protons extracted from the distribution reported in fig. 4.11.

### 4.2.3 Primary particles

The primary particles' generation is managed by classes which are already described in Sec. 3.1.2. Here, the Inverse Transform Sampling method and its implementation is described because it is employed to generate primary particles characterized by an exponential energy spectrum.

Consider to start with a set of *energies* and the corresponding *data*, which reproduce the desired spectrum. Then, a random number uniformly distributed between 0 and 1 is generated and multiplied by the sum of the *data* (here called *random*).

Using an iterative procedure, starting from the first, each value of *data* is summed to the previous ones producing a new number (*dat\_sum*) at each iteration. When the value of *dat\_sum* overcomes *random*, the iteration is stopped and a proton having the *energy* corresponding to the current *data* is generated. In fig. 4.11 and 4.12, an example of the discrete probability distribution function (the *energies* and the corresponding *data*) is reported and the associated exponential energy spectrum generated with  $10^5$  incident protons.

A final remark concerns the primary particle direction when the exponential spectrum is involved: protons are generated with a cylindrical symmetry, emitted with an angle normally distributed between  $0^\circ$  and  $3^\circ$  with respect to the target normal (see fig. 4.10). This is coherent with the divergence of common laser-driven proton sources.

### 4.2.4 Detector and data recording

As shown in fig. 4.8, the detector is represented by a cylindrical volume. The program propagates the X-rays until they exit the simulation area, or they meet the detector. Photons that reach the detector are passed to an analysis routine. Practically this is done in the following way:

1. X-rays are followed by the program with the call of the *UserSteppingAc-*

*tion(const G4Step\*)* method at the end of each step. Inside this method, if the pre-step point is inside the *World* and the post-step point is inside the *detector*, the X-ray energy is passed to a so called *AnalysisManager* class through a proper method.

- Employing a SiLi detector, the X-rays incident on the detector are recorded considering the efficiency curve <sup>1</sup> reported in fig. 4.13. This is done by extracting the efficiency value corresponding to the X-ray energy from the curve. A random number between 0 and 1 is generated and compared with the efficiency value: if this random number is less than the efficiency, then the X-ray is considered as recorded by the detector.

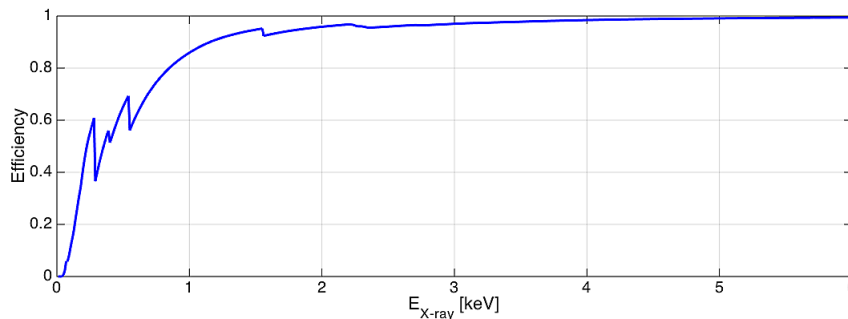


**Figure 4.13:** *Detector intrinsic efficiency curve employed in all the Monte Carlo simulations.*

- In order to consider the detector resolution, as reported in [63], the full width at the half maximum is evaluated with this expression:

$$FWHM = \sqrt{(FWHM_n)^2 + (2.35(F \times E \times \varepsilon)^{1/2})^2} \quad (4.22)$$

where  $E$  is the X-ray energy in [eV],  $F = 0.1$  and  $\varepsilon = 3.9$  eV are constants,  $FWHM_n = 150$  eV represents the electronic noise. Then a Gaussian distribution is generated and the X-ray energy value is corrected according to it.

- The counts of the detected X-ray photons are stored in a histogram. The same can be done also considering the initial proton energy which is involved in the X-ray emission, in addition to the X-ray energy itself. In this way, for each characteristic X-ray, the differential yield can be obtained from the simulation and compared with the one theoretically calculated with the model.

<sup>1</sup>from the Geant4 *xray\_flourescence* advanced example.



### 4.2.5 Comparison with experimental data from literature

Before considering simulations involving new experimental set-ups, it is necessary to start with a case from literature. In this way, from a comparison, the Monte Carlo code will be validated, as well as the implementation of the theoretical model in the case of monoenergetic protons. One of the cases presented in [2] has been selected: the target consists in a copper substrate coated with a nickel surface layer ( $0.55 \mu\text{m}$  thick). The measurement is performed employing monoenergetic proton beams with energies between 0.3 and 1.6 MeV. This case is particularly suitable for our test because the sample composition is very simple and the reported experimental results are independent of the detector solid angle and number of incident protons.

The goal of the analysis reported in [2] is essentially to demonstrate the possibility to perform a *Differential PIXE* employing different monoenergetic proton beams. The detailed description of the numerical procedure proposed in this paper is reported in Sec. 2.2.4.

Here, we will focus only on one of the experimental cases discussed in the article: the target is characterized by the presence of a surface layer made of nickel,  $0.55 \mu\text{m}$  thick and a substrate composed by copper. The measurement is performed employing monoenergetic protons with energy between 0.3 and 1.6 MeV.

As an intermediate step in the analysis, the authors report the ratio between the yields for the two elements as a function of the energy of the incident protons, both measured experimentally and calculated from the model described in Sec. 2.2.4 (with the inclusion of the secondary fluorescence and proton energy straggling). The result is shown in fig. 4.14 where *expt.* refers to the experimental data, *SF* stands for theoretical model including secondary fluorescence, *straggling* means that also the straggling due to the passage of the beam through the exit window and the air gap have been considered. Both the secondary fluorescence and the energy straggling contributions to the X-ray

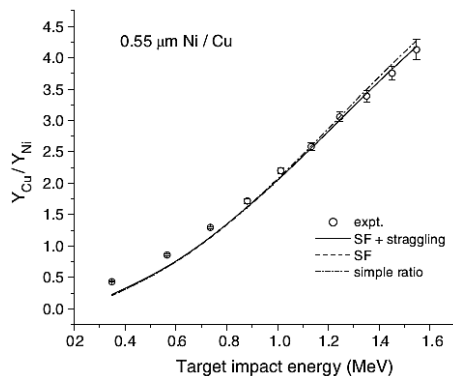


**Figure 4.14:** Ratio of the X-ray yields (reproduced from [2]).

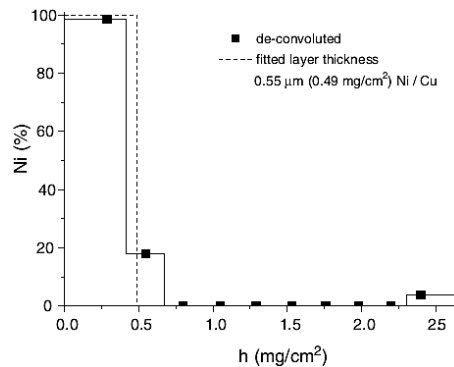


**Figure 4.15:** Nickel concentration profile (reproduced from [2]).

yields are negligible. As shown in the graphs, the authors found excellent agreement between experimental data and those obtained from the model.

Then, assuming an unknown concentration profile, the iterative procedure was applied in order to derive the elemental distribution as a function of the depth. The final result is shown in fig. 4.15.

The Monte Carlo simulation aimed to reproduce the described experiment was carried out using protons characterized by having identical energies to those used in the publication. For each energy,  $2 \times 10^8$  events were simulated. In order to compare the experimental results  $(Y_{Cu}/Y_{Ni})_{expt}$  with the Monte Carlo simulation  $(Y_{Cu}/Y_{Ni})_{MC}$  output, for each proton energy value, the relative error  $|(Y_{Cu}/Y_{Ni})_{expt} - (Y_{Cu}/Y_{Ni})_{MC}| / (Y_{Cu}/Y_{Ni})_{expt}$  has been reported in fig. 4.16.

Except for the first point, the relative error is always in the order of a few per-

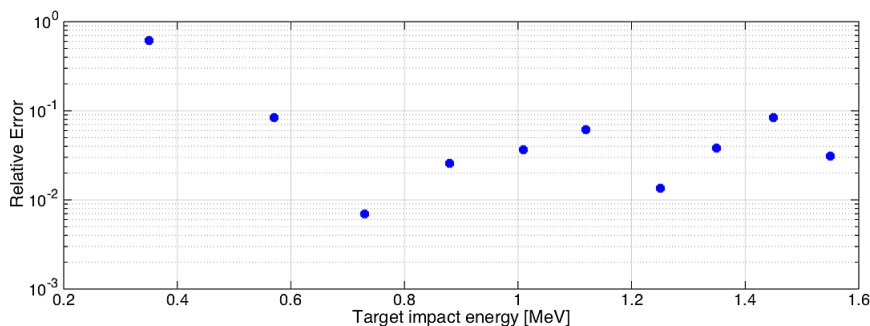


**Figure 4.16:** Comparison between experimental (reproduced from [2]) and simulated results.

centage points. The discrepancy associated with the first point is related to the fact that, for such a value of proton energy, the X-ray yield of both Ni and Cu is very low and therefore there is no statistical validity for the data in question. It can be concluded that the Monte Carlo simulation produces reliable data as the experimental results reported in [2] are well replicated.

As the case under consideration uses monoenergetic proton, it is possible to employ the model described in Sec. 2.2.2 in order to calculate theoretically the quantity  $(Y_{Cu}/Y_{Ni})_{model}$ , as done in the publication. Accordingly, a comparison between the Monte Carlo simulation output  $(Y_{Cu}/Y_{Ni})_{MC}$  and  $(Y_{Cu}/Y_{Ni})_{model}$  is provided. The result is reported in fig. 4.17 and also in this case there is good agreement between the curve and the data points.

The last goal is to test the iterative algorithm taking the Monte Carlo outputs as experimental data and assuming an unknown concentration profile. Then, the application of the iterative procedure to the simulation results produce the profile shown in fig. 4.18. The final results are very satisfactory, since the retrieve concentration profile well approximate the real one.

The overall procedure described in this section starts with an initial comparison between the calculated X-ray yields and the experimentally evaluated (or sim-

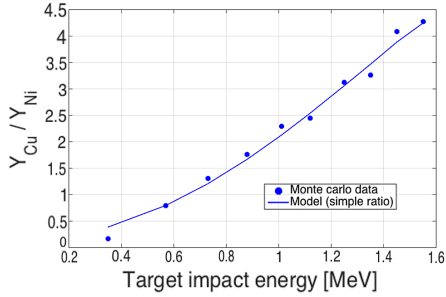


**Figure 4.17:** Ratio between the X-ray yields of Cu and Ni for different proton initial energies from Monte Carlo simulation and theoretical model.

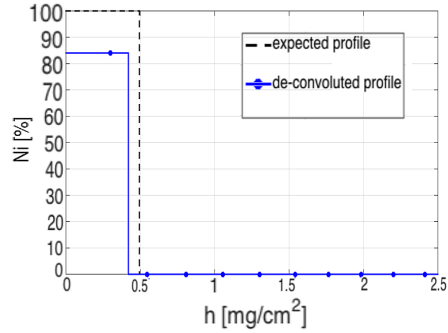


**Figure 4.18:** Nickel concentration profile derived from the analysis of the Monte Carlo simulation outputs (blue) and expected nickel concentration profile (dotted line).

ulated) ones. This provides an initial estimate of model reliability. In a second time, the code based on the model is tested by assuming an unknown sample composition and applying the iterative procedure to the experimental data (or simulation outputs). The result in term of sample properties can be compared with the original composition. This procedure will be applied also to the case of laser-driven PIXE.

### 4.3 Comparison between PIXE analysis with monoenergetic and exponential proton spectra

The aim of this paragraph is to investigate, employing the models presented in Sec. 4.1, how PIXE made with laser-driven protons can work. Different cases of possible targets have been considered for this purpose. For each of them, a Monte Carlo simulation was performed to generate synthetic experimental data. Then, the algorithms based on the models developed in Sec. 4.1 have been applied to the simulation results in order to reconstruct the composition of the samples.

At the same time, the same procedure was carried out using monoenergetic protons in order to have a comparison between PIXE performed with monoenergetic and TNSA protons. The retrieved elemental concentrations will be listed and compared with the original ones inserted as input in the Monte Carlo simulation.

#### 4.3.1 Main assumptions

The set of simulations presented in this Section are subject to a certain degree of ideality:

- The energy spectrum for a TNSA proton bunch is approximated to a perfect exponential between two well-defined maximum and minimum energies. This is coherent with values reported in literature [47]. Anyhow, in Sec. 5.1, a more realistic simulation will be described. As far as monoenergetic protons are concerned, the energies have been selected by choosing realistic values compared to those currently employed for PIXE studies.
- Both the detector efficiency and dimensions are common to the simulations employing monoenergetic and laser-driven protons. In the second case, all the X-rays are emitted in a time window which can go from ns to tens of ns. So a different detector from Si(Li) should be employed, because this is characterized by a dead time equal to  $\mu\text{s}$  (a possible alternative will be proposed in Sec. 5.1).
- The number of protons is selected considering an overall simulation time lower, or at least equal, to 24 hours employing a normal desktop core i7 machine. As a result,  $10^8 \div 10^9$  protons have been considered for both monoenergetic and exponential spectra. Of course, both in the case of traditional PIXE and laser-driven PIXE, the number of primary particles can be higher, but will still allow us to apply the models for the quantitative analysis. This is demonstrated by the agreement between the experimental and simulated data shown in Sec. 4.2.5, where a similar number of protons was employed.

### 4.3.2 Thin target

In the case of a thin target, the sample has been chosen with a thickness equal to  $1 \mu\text{m}$  and it is composed by nickel, chrome, iron and titanium (the mass concentrations are reported in the second column of table 4.1).

#### Monoenergetic protons

$10^8$  protons with an energy of 3 MeV were simulated.

Fig. 4.19 shows the X-ray spectrum recorded using monoenergetic protons. Above each peak, the associated transition is reported. The data necessary to perform the analysis in order to get the concentrations are the X-ray yields of the  $K\alpha$  peaks, one for each element, and they are reported in the third column of table 4.1.

Assuming an initial unknown composition and applying the iterative algorithm described in Sec. 2.2.1, the elemental concentrations are evaluated and reported in the fourth column of table 4.1.

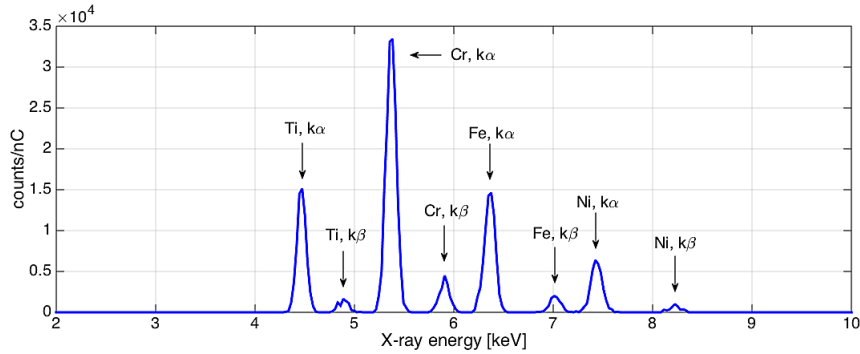


**Figure 4.19:** X-ray spectrum using monoenergetic protons for the thin target case.

### Protons with exponential energy spectrum

As far as non-monoenergetic protons are concerned, the exponential energy spectrum has been chosen with a minimum energy equal to 1 MeV, a maximum energy equal to 6 MeV, a temperature  $\alpha$  of  $0.6 \text{ MeV}^{-1}$  and a total number of protons equal to  $2 \times 10^8$  have been simulated.

Fig. 4.20 represents the differential X-ray spectrum obtained using protons

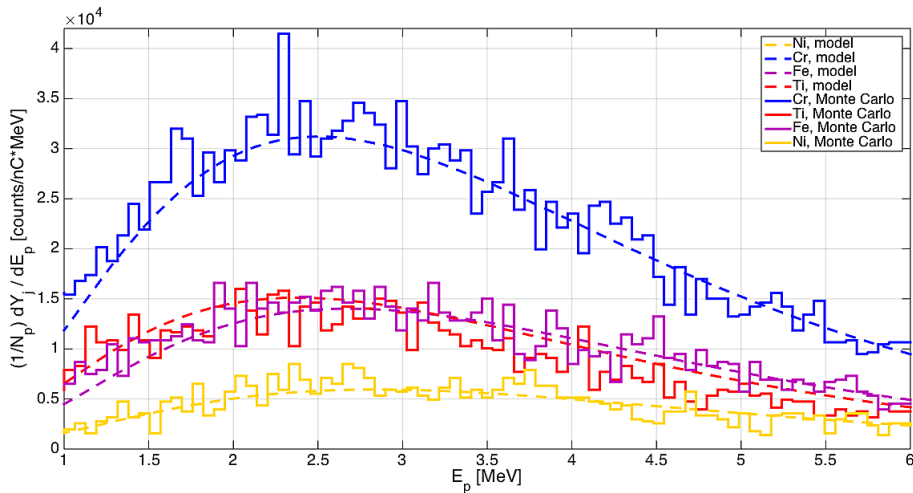


**Figure 4.20:** Differential X-ray yields for the thin target case.

with the exponential energy spectrum, both calculated from the model (dotted lines), assuming the elemental concentrations to be known, and derived from the simulation (histograms). This comparison is a first test to verify the model's reliability.

The next step is to assess the accuracy of the iterative code. Then, assuming an unknown sample composition, the iteration described in Sec.4.1 of this Chapter can be applied in order to get the elemental concentrations (see last column

of table 4.1). The application of the iterative code is performed on quantities which can be only measured in a real experiment. So, the analysis of the Monte Carlo results requires the integral yield for each element, which is reported in the fifth column of table 4.1.

By comparing the values of  $W_{j,real}$ ,  $W_{j,mono}$  and  $W_{j,exp}$ , it can be concluded

**Table 4.1:** *Simulations outputs (counts/nC) and analysis results (%) for the thin target case.*

Element	$Y_{j,mono}$ (counts/nC)	$Y_{j,exp}$ (counts/nC)	$W_{j,real}$ (%)	$W_{j,mono}$ (%)	$W_{j,exp}$ (%)
Ni	$3.29 \times 10^4$	$5.74 \times 10^5$	20.0	23.3	21.0
Cr	$1.58 \times 10^5$	$2.89 \times 10^5$	40.0	38.7	40.5
Fe	$7.23 \times 10^4$	$1.34 \times 10^5$	30.0	30.0	30.2
Ti	$6.39 \times 10^4$	$1.17 \times 10^5$	10.0	8.0	8.3

that both the techniques are equally able to retrieve the initial composition of the target. In fact, the difference between the concentrations obtained and initially set in the simulation differs no more than a few percentage points. Therefore, under the hypothesis and the parameters listed in Sec. 4.3.1, it can be stated that this analysis supports the feasibility of laser-driven PIXE in the case of thin targets.

### 4.3.3 Thick homogeneous target

The target has been chosen with a thickness equal to  $15 \mu\text{m}$  and it is composed by nickel, chrome and molybdenum (the mass concentrations are reported in the second column of table 4.2). In this case the finite thickness of the sample can not be neglected, since protons are completely stopped in the sample and x-rays undergo a non-negligible attenuation, as is described in Sec. 2.2.2 and 4.1.2.

#### Monoenergetic protons

$10^8$  protons with an energy of 5 MeV have been simulated. The data necessary to perform the analysis in order to get the concentrations are the X-ray yields of the  $K\alpha$  peaks, visible in fig. 4.21. The recorded values of the yields are reported in the third column of table 4.2. These simulation outputs can be employed in the algorithm described in Sec. 2.2.2 in order to retrieve the concentrations of the elements (see fourth column of table 4.2).

#### Protons with exponential energy spectrum

The exponential energy spectrum has been chosen with a minimum energy equal to 1 MeV, a maximum energy equal to 6 MeV, a temperature  $\alpha$  of  $0.6 \text{ MeV}^{-1}$ .

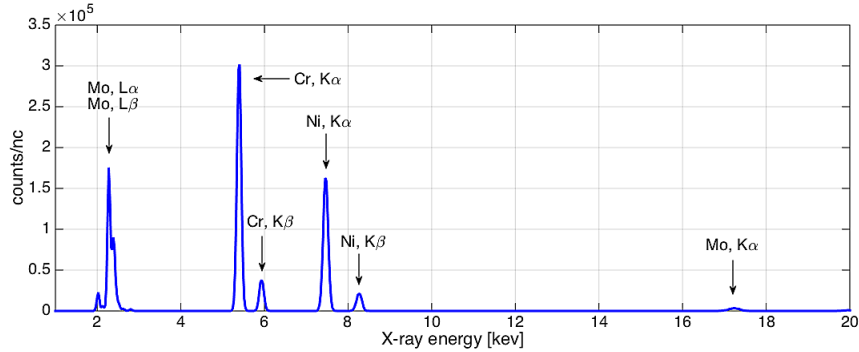


**Figure 4.21:** X-ray spectrum using monoenergetic protons for the thick target case.

The only difference with the case described in Sec. 4.3.2 is the total number of protons employed which is equal to  $3 \times 10^8$ .

Fig. 4.22 reports the differential yield both retrieved by the Monte Carlo

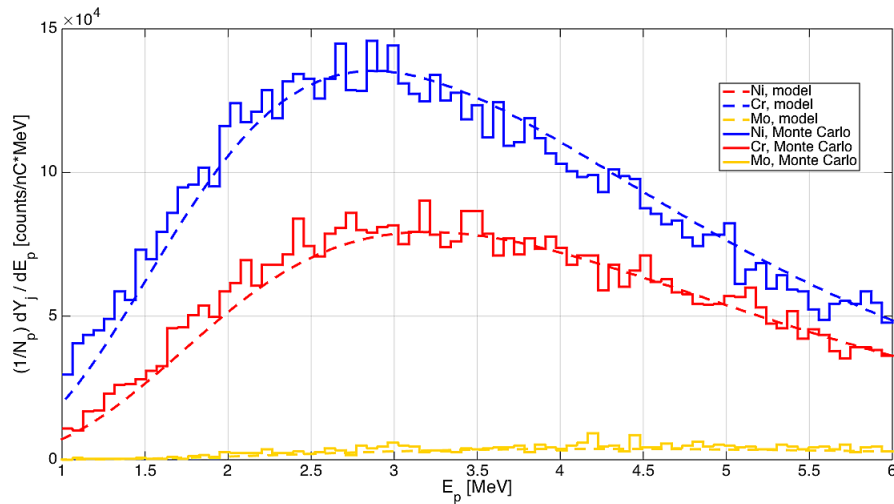


**Figure 4.22:** Differential X-ray yields for the thin target case.

(histograms) and evaluated with the theoretical model described in Sec. 4.1.2 (dotted lines). There is a good agreement between model and simulation. Extracting from the simulation also the total yields of interest for each element (see fifth column of table 4.2) and assuming an unknown elemental composition, the iterative procedure based on the aforementioned model can be tested. The result is reported in the last column of table 4.2.

Also in this case there is good agreement between  $W_{j,real}$ ,  $W_{j,mono}$  and  $W_{j,exp}$  and we can conclude that the iterative models converge to the correct concentration values both in the case of monoenergetic protons and exponential spectrum. So the analysis supports the possibility of using laser-driven protons in order to perform PIXE studies in the case of thick homogeneous targets.

**Table 4.2:** *Simulation outputs (counts/nC) and results of the analysis (%) for the thick target case.*

Element	$Y_{j,mono}$ (counts/nC)	$Y_{j,exp}$ (counts/nC)	$W_{j,real}$ (%)	$W_{j,mono}$ (%)	$W_{j,exp}$ (%)
Ni	$9.36 \times 10^5$	$2.95 \times 10^5$	40.0	40.5	41.6
Cr	$1.25 \times 10^6$	$4.73 \times 10^5$	30.0	29.8	30.3
Mo	$7.81 \times 10^4$	$1.73 \times 10^4$	30.0	29.7	28.1

#### 4.3.4 Multilayer target

For the multilayer analysis, the target is characterized by a three layer structure (the third one is a semi-infinite substrate) containing nickel, chromium and molybdenum distributed as shown in table 4.3.

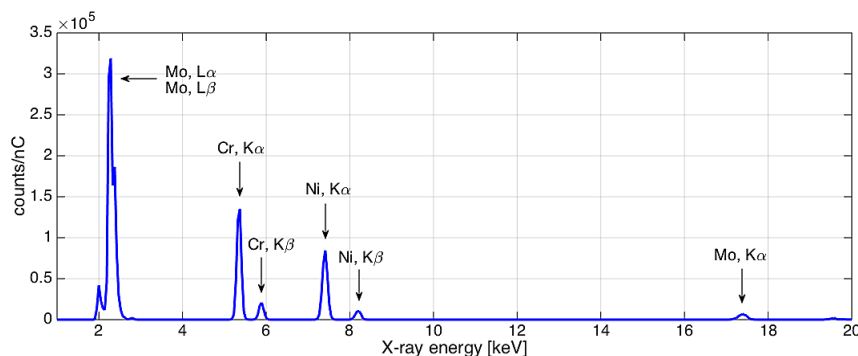
**Table 4.3:** *Multilayer target structure set initially in the simulation.*

Layer	Thickness ( $\mu\text{m}$ )	Ni (%)	Cr (%)	Mo (%)
1	3	20	0	80
2	6	40	60	0
3	$\infty$	0	30	70

#### Monoenergetic protons

$2 \times 10^8$  protons with an energy of 3 MeV have been simulated. Fig. 4.23 reports the X-ray spectrum.

From the X-ray yield reported in the second column of table 4.3.4 (a), applying the iterative model shown in 2.2.3, it is now possible to retrieve the layer thicknesses. The result is reported in the third column of table 4.3.4 (b).

**Figure 4.23:** *X-ray spectrum using monoenergetic protons for the multilayer target case.*



### Protons with exponential energy spectrum

The exponential energy spectrum has been chosen with a maximum and minimum energy equal to 5 MeV and 1 MeV, a temperature  $\alpha$  of  $0.6 \text{ MeV}^{-1}$  and  $2 \times 10^8$  protons are simulated.

The differential yield calculated both with the theoretical model and obtained from the Monte Carlo simulation is shown in fig. 4.24, assuming that the layer thicknesses are known a priori (as well as the mass concentrations). There is a good agreement between model and simulation.

The total yields are reported in the third column of table 4.3.4 (a). Considering an unknown layer structure in terms of thicknesses and applying the iterative procedure based on the model described in the Sec. 4.1.3, the layers' interface can be calculated and compared to the original ones. The results are listed in the fourth column of table 4.3.4 (b).

By observing table 4.3.4 (b), it can be concluded that the two techniques are

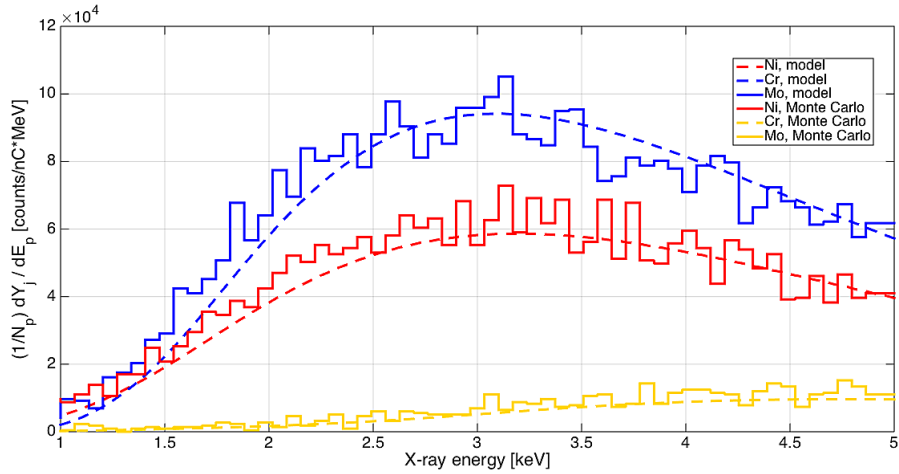


**Figure 4.24:** *Differential X-ray yields for the multilayer target case.*

**Table 4.4:** *Outputs and results for the multilayer target case.*

(a) Simulations outputs (counts/nc).			(b) Analysis results ( $\mu\text{m}$ ).			
El.	$Y_{j,mono}$ (counts/nC)	$Y_{j,exp}$ (counts/nC)	Layer	Real ( $\mu\text{m}$ )	Mono ( $\mu\text{m}$ )	Exp ( $\mu\text{m}$ )
Ni	$1.34 \times 10^5$	$7.16 \times 10^4$	1	3	3.17	3.03
Cr	$1.91 \times 10^5$	$1.06 \times 10^5$	2	6	6.6	5.44
Mo	$1.76 \times 10^5$	$1.63 \times 10^4$	3	$\infty$	-	-

equally able to return the target structure, since the thicknesses obtained by processing the yields with the models well approximate the values initially set

in the simulation. So, also in this case, the results suggest the possibility to use laser-driven protons in order to perform the multilayer target analysis.

In both cases, there is a reduction in precision in predicting the thickness of the layers from the superficial to the underlying. This is a consequence of the fact that the X-ray production degrades as depth increases, resulting in deterioration in analytical capacity. It can be noticed both with monoenergetic protons and employing an exponential energy spectrum source. This effect was observed also in other analogous simulations. Anyway, it was also verified that, by increasing the proton energies, deep layers can be analyzed with higher precision.

### 4.3.5 Generic non-homogeneous target

In this Section the case of the *Differential PIXE* is considered. In Sec. 4.1.4 two possible strategies were presented in order to retrieve the concentration profiles of the elements preset in a generic and completely unknown sample. The first case involves the use of a certain number of proton bunches characterized by different maximum energies in the spectra. In the second case, only one proton bunch is employed, the energy spectrum is divided into intervals and the X-rays associated to each of them are recorded together. Here, this last one methodology is tested, since the simulation time for the first case would be prohibitive.

Having already reproduced a literature case with regard to the use of monoenergetic proton beams, in this section, with reference to the analysis reported in [36], an example of *Differential PIXE* analysis employing protons with exponential energy spectrum is described.

In [36], some Roman military equipment artifacts are analyzed with PIXE technique, including a sword and a silver belt plate. The authors also performed a *Differential PIXE* analysis employing monoenergetic protons with energies between 0.74 and 2.5 MeV on a broach made of brass and tin. The concentration profile for the three elements recorded (tin, copper and zinc) are reported in fig. 4.25.

Starting from the concentration profiles reported in the paper, it is reasonable to assume that the sample is composed by a surface layer of thickness equal to  $1.3 \mu\text{m}$  made of 100 % of tin and by a substrate containing 90 % of copper and 10 % of zinc. So, this is the target composition employed to perform the Monte Carlo simulation. Its function is to provide X-ray spectra which can be passed

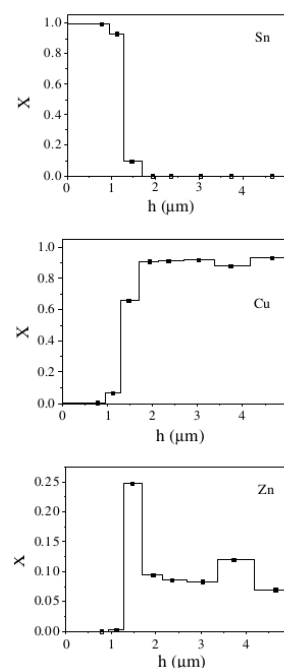


**Figure 4.25:** Concentration profile of the surface layer for a broach (reproduced from [36]).

as input to the iterative code.

The proton exponential energy spectrum has a maximum energy of 4.5 MeV and a minimum one equal to 0.5 MeV, the temperature is 0.6 and the total number of protons is set to  $10^9$ .

As already done in the previous cases, the differential yield, both extracted from the Monte Carlo simulation and evaluated with the theoretical model assuming a known concentration profile, is reported in fig. 4.26.

As described in Sec. 4.1.4, the proton spectrum is partitioned into slices (7 in

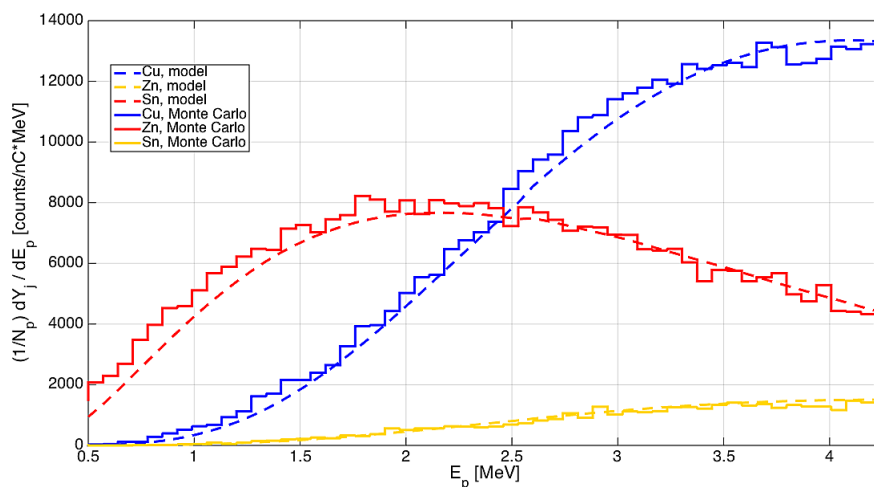


**Figure 4.26:** *Differential X-ray yields for the generic non-homogeneous target case.*

this case) and the X-rays produced by protons associated to the same proton energy band are recorded together. Proton energy intervals and the corresponding X-ray yields are reported in table 4.5. Finally, applying the iterative model

**Table 4.5:** *Simulation outputs (counts / nC) for the Differential PIXE case.*

$\Delta E_p$ (MeV)	$Y_{Cu}$ (counts/nC)	$Y_{Zn}$ (counts/nC)	$Y_{Sn}$ (counts/nC)
0.50 - 1.07	$3.44 \times 10^4$	$5.65 \times 10^5$	$1.76 \times 10^3$
1.07 - 1.64	$1.79 \times 10^5$	$8.17 \times 10^5$	$1.61 \times 10^4$
1.64 - 2.21	$3.67 \times 10^5$	$7.26 \times 10^5$	$3.68 \times 10^4$
2.21 - 2.79	$5.16 \times 10^5$	$5.36 \times 10^5$	$4.52 \times 10^4$
2.79 - 3.35	$5.50 \times 10^5$	$3.46 \times 10^5$	$5.27 \times 10^4$
3.35 - 3.93	$4.53 \times 10^5$	$2.07 \times 10^5$	$4.67 \times 10^4$
3.39 - 4.50	$3.34 \times 10^5$	$1.18 \times 10^5$	$3.42 \times 10^4$

reported in Sec. 4.1.4, the concentration profile can be retrieved and the final result is shown in fig. 4.27. Overall the agreement is remarkable, with a maximum discrepancy always lower than 8 %.

There is a very good agreement between the real profile (dotted black line) and the one derived from the analysis (blue line), since for all three profiles the difference between the actual concentrations and the one resulting from the analysis is always lower than 8 %. Then, it is possible to consider the possibility to perform *Differential PIXE* with a laser-driven proton source.

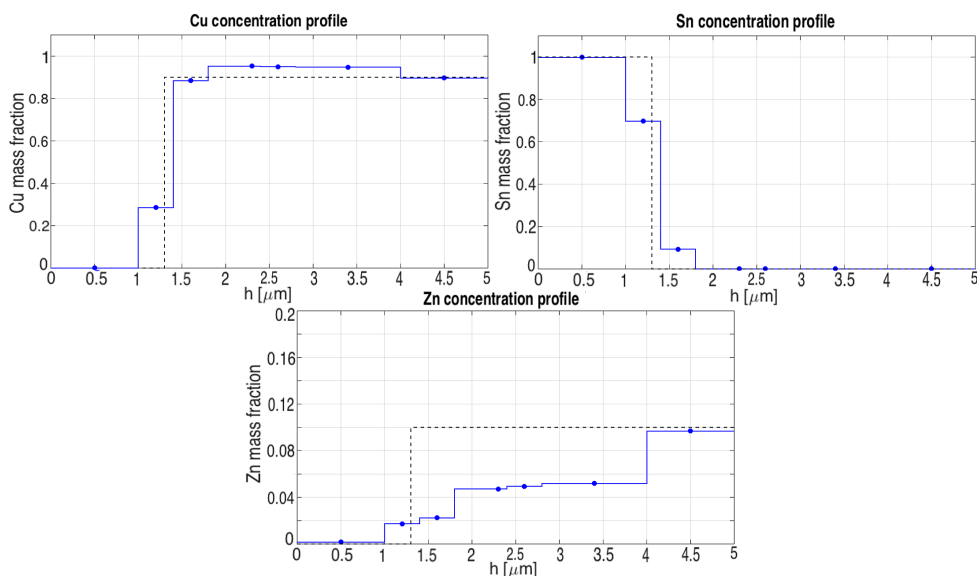


**Figure 4.27:** Comparison between the real broach concentration profiles (dotted black line) and the ones derived from the analysis (blue line).

#### 4.3.6 Final considerations

The results obtained suggest that in principle the use of non-monoenergetic beams does not present any disadvantage for the PIXE technique. Taking the same number of protons for both monoenergetic and laser-driven protons, the accuracy in predicting the sample structure is very similar.

The currents provided by particles accelerators for PIXE analysis can range from tens of pA up to tens of nA. The measuring time generally is of the order of few minutes, so the total number of particles employed can go from  $10^9$  up to  $10^{12}$ . Considering that the number of protons provided by laser-driven proton sources ranges from  $10^9$  up to  $10^{12}$  part/MeV/str (see Sec. 1.3), there would be the possibility of performing a complete analysis employing a single laser shot. In the case of *Differential PIXE* with a laser-driven source (see Sec. 4.3.5), from the experimental point of view, considering to use different proton bunches and changing the maximum spectrum energy would arguably be the simplest solution. On the other side, employing a single proton bunch would imply to be

equipped with a very fast detection system. The detector must be able to collect separately X-rays arriving at different time intervals, each of which lasting few nanoseconds. Another solution can be to place in front of the target a number of detectors equal to the number of required measurements. Then, they can be triggered in sequence at different instants of time.

In the light of the aforementioned comments, and considering the high level of idealization of the simulations presented in Sec. 4.3.1, the next natural step to consider a more realistic case. This will be the goal of Sec. 5.1.

## Chapter 5

# A more realistic analysis: PIXE & PIGE characterization of paint layers

The aim of this Chapter is dual. A first goal is to reduce the level of idealization adopted in the simulations presented in Chapter 4 in order to test a more realistic case. Considering both a less idealized proton spectrum and a possible real experimental apparatus, it is intended to test whether PIXE with laser-driven protons can actually be executed with a single shot and how the models described in Chapter 4 behave when a non-perfectly exponential spectrum is employed. This will be the subject of Sec. 5.1.

Later, given the important role that PIXE and PIGE have in the field of cultural heritage, we will analyze how laser-driven protons can be used in the analysis of paintings. Then, Sec. 5.2.1 is devoted to the study of the stratigraphic structure of a painting using PIXE, while Sec. 5.2.2 addresses the sensitivity of PIGE in the identification of lapis-lazuli. For both analyzes, the only theoretical model developed in Sec. 4.1 will be used.

### 5.1 PIXE analysis using PIC laser-driven proton spectrum and a Von Hamos spectrometer

In this first part of the Chapter, the study proposed in Sec. 4.3.3 for the case of a thick homogeneous target is repeated considering:

1. A more realistic Monte Carlo simulation for which:
  - The laser driven proton energy spectrum is not a simple exponential, but it is the result of a Particle In Cell simulation (see Sec. 3.2).
  - The detection system is based on a Von Hamos configuration (see Appendix B) which provides the X-ray diffraction with a crystal. X-

rays are imaged on a scree, which may consist of an imaging plate (a passive detector not characterized by a dead time) or a fast X-ray CCD camera.

2. To employ the model developed in Sec. 4.1.2 in order to determine the concentrations of the elements, approximating the PIC energy spectrum with a simple exponential.
3. Study the sensitivity of the obtained concentrations with respect to the spectrum temperature value assumed in the model. The spectrum temperature value can oscillate from bunch to bunch, so it is necessary to understand its effect on the analysis.

### 5.1.1 Sample composition and type of analysis

The sample chosen in order to perform this investigation is the sword-scabbard described in [36]. It is characterized by the bulk composition, in terms of elemental mass concentrations, reported in table 5.1.

So, among the four possible cases described in Chapter 4, this has to be

**Table 5.1:** *Sword-scabbard bulk elemental composition.*

	Iron	Copper	Zinc	Lead	Tin
Conc. (%)	1.09	76.61	19.9	0.5	1.9

considered as an example of thick homogeneous target analysis. The more concentrated elements are copper and zinc, while iron, tin and lead are present in traces.

The objective of the analysis is to reconstruct the sample composition in detail for the most concentrated elements (Cu and Zn) and to test the sensitivity for those present in traces (Fe, Pb and Sn).

### 5.1.2 PIC simulation as Monte Carlo input

The output of the 2-D Particle in Cell simulation employed here to describe the laser driven proton source is a discretization of the function  $d^2N_p(E_p, \theta)/dE_p d\theta$ . It is shown in fig. 5.1. Once normalized, it can be interpreted as the probability of emitting a proton with a certain energy  $E_p$  and divergence angle  $\theta$  with respect to the target normal (protons are emitted from the rear of the target). The maximum energy  $E_{p,max}$  is  $\sim 4$  MeV and the maximum divergence angle is  $\sim \pm 6^\circ$ . This function is provided to the Monte Carlo simulation which generates the primary particles by means of the Inverse Transform Sampling method described in Sec. 4.2.3.

The number of simulated primary particles is  $10^9$ . However, normalizing the detector efficiency to its maximum value, the simulation is equivalent to an experiment in which the total number of protons is  $10^{11}$ .

### 5.1.3 Geometry set-up and Von Hamos detector configuration

The Von Hamos spectrometer uses a bent crystal to reflect X-rays on a screen, which usually consists of an X-ray CCD. The crystal diffracts the X-rays with a certain wavelength according to the Bragg law:

$$n\lambda = 2d \sin \theta \quad (5.1)$$

where  $d$  is the distance between the atomic layers of the crystal,  $\theta$  is the angle of grazing incidence and  $n$  is the order of diffraction (see fig. 5.2). The config-

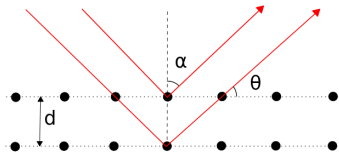


**Figure 5.2:** Bragg reflection scheme.

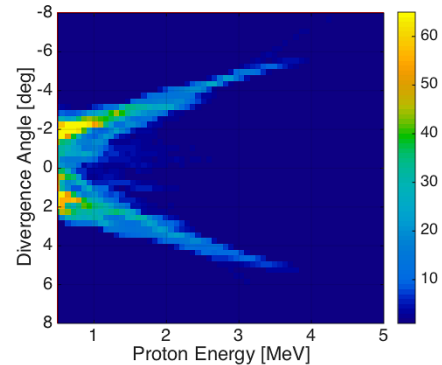


**Figure 5.1:**  $d^2N_p(E_p, \theta)/dE_p d\theta$ , 2D PIC simulation output.

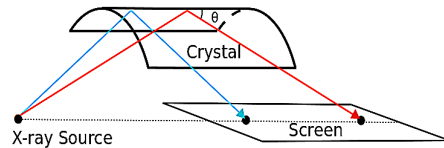


**Figure 5.3:** Planar Von Hamos spectrograph.

uration generally adopted is shown in the fig. 5.3.

In this work an innovative set-up is considered, where the crystal is a full cylinder [71]. In this way a much larger solid angle is subtended by the detector and the total efficiency is maximized. Here the screen is not parallel to the crystal optical axis, but oriented orthogonally to it. This geometry is schematically reported in fig. 5.4.

As shown in the figure, the reflected X-rays are spread along the radial direction, depending on their energy, to form circles. Each circle corresponds to an X-ray peak. Depending on whether the screen is placed after or before the focus position, the energies will be either increasing or decreasing along the radial direction respectively. A snapshot of the simulation showing the geometry is reported in fig. 5.5: protons are made to impinge on the sample (yellow), the X-rays (green) are emitted, and they impinge on the crystals (blue). Also, the screens (grey) are present in the geometry. The presence of more than one screen prevents that the X-rays, after the first reflection on the internal surface of the crystal, must be able to exit without being reflected again



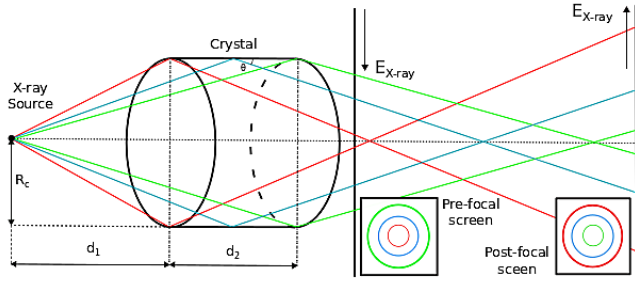


**Figure 5.4:** Full-cylinder Von Hamos geometry.

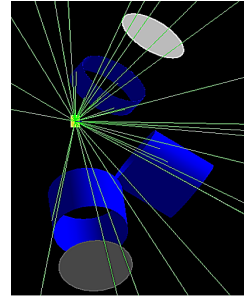


**Figure 5.5:** Running simulation.

This Section do not contain detailed information about the detector. A detailed description about the experimental apparatus and its modeling in the Monte Carlo simulation can be found in Appendix B.

### 5.1.4 Results and considerations

In fig. 5.6, 5.7 and 5.8 are reported the three screens after the end of the analysis: each circle represents a characteristic X-ray peak.

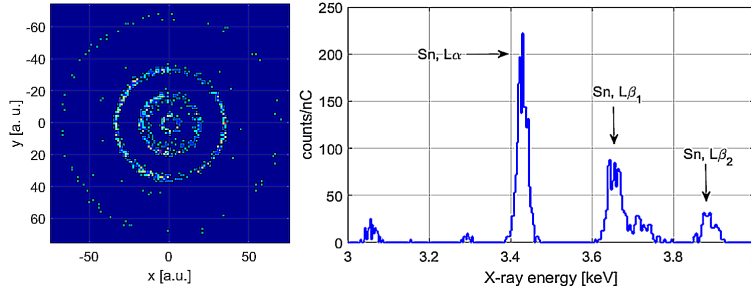


**Figure 5.6:** First screen (pre-focus) and related spectrum.

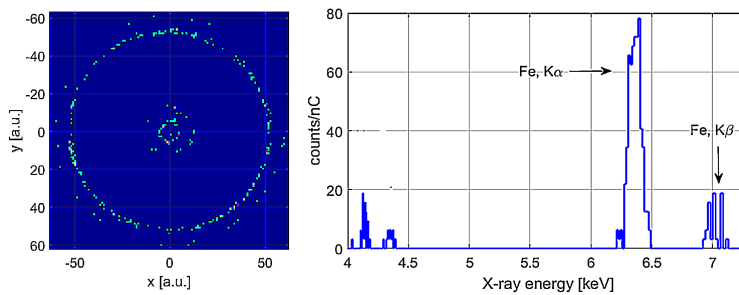


**Figure 5.7:** Second screen (post-focus) and related spectrum.

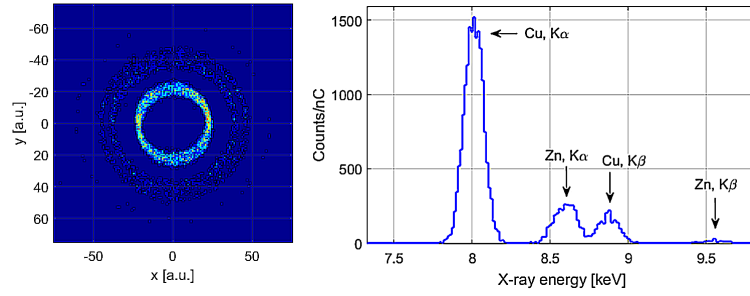


**Figure 5.8:** *Third screen (post-focus) and related spectrum.*

Summing along the angular coordinate and converting the radius into the equivalent energy value for X-rays, you can get the three spectra shown alongside.

### Analysis with the iterative model

Once the results of the simulation in terms of X-rays yields are available, the developed model described in Sec. 4.1.3 can be applied in order to retrieve the sample composition. Here, a simple exponential spectrum is considered, assuming a temperature  $\alpha$  equal to  $1.05 \text{ MeV}^{-1}$ .

Fig. 5.9 shows the comparison between the energy spectrum recorded from the simulation and the idealized one assumed to carry out the analysis.

Both the correct concentrations and those retrieved from the analysis are reported in table 5.2. Among the trace elements, only lead is not detected because its concentration is too low. For the other trace elements (Fe and Sn), the analysis provides good estimations for the mass concentrations, while, for Cu and Zn, the final result is very accurate.

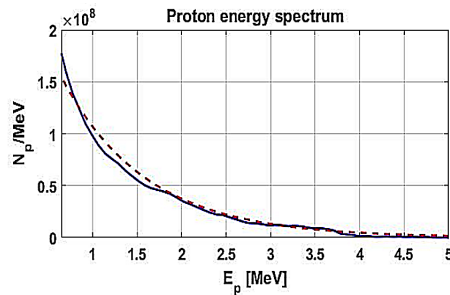


**Figure 5.9:** *Proton spectra from the PIC simulation (continuous line) and chosen for the analysis (dotted line).*

Element	$W_{j,real}$ (%)	$W_{j,analysis}$ (%)
Fe	1.09	1.12
Cu	76.61	77.40
Zn	19.90	19.80
Pb	0.50	~
Sn	1.90	1.66

**Table 5.2:** *Real concentrations vs. retrieved concentrations.*

It is important to emphasize that the analysis was possible employing a total

number of protons equivalent to  $2 \times 10^{11}$ , so compatible with that produced in a single shot by powerful lasers (see Sec. 1.3) or in few tens of shots by table-top lasers.

### Effect of the proton spectrum temperature

In this paragraph we want to make some considerations regarding the choice of the shape of the proton spectrum to be used in the model.

The iterative code employed to retrieve the results shown in the third column of table 5.2 approximates the proton energy spectrum as a pure exponential function. On the other hand, the shape of the proton energy spectrum employed in the Monte Carlo is more realistic, being the result of a 2D PIC simulation. Obviously, the selected temperature  $\alpha$ , equal to  $1.05 \text{ MeV}^{-1}$ , makes the pure exponential very close to the PIC simulation spectrum employed in the Monte Carlo (see fig. 5.9). Then, the iterative procedure converges on the correct concentration values.

The aim is to test how the choice of the spectrum temperature in the iterative code affects the final result in terms of the reliability of the retrieved concentrations. So, starting from the same Monte Carlo simulation results (and so the same PIC energy spectrum), the analysis with the iterative code has been redone using different temperature values, starting from 0.7 up to 1.3. Fig. 5.10 shows the retrieved mass concentrations as a function of the different temperature values adopted in the iterative code. It is clear that the proton spectrum

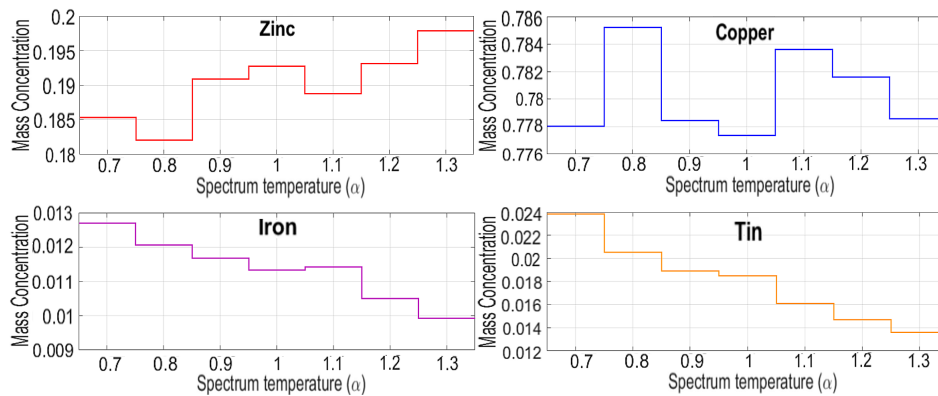


**Figure 5.10:** Retrieved mass concentrations for different values of the spectrum temperature  $\alpha$ .

temperature does not affect significantly the final result. This is true in a considerably wide range of values for  $\alpha$ . Of course, this is very advantageous as it allows splitting the analysis of the experimental results by a precise knowledge of the proton spectrum shape. This is beneficial because the spectrum temperature is often a quantity not precisely measured and subject of fluctuations from bunch to bunch.

## 5.2 Characterization of paint layers with PIXE & PIGE

### 5.2.1 *Differential PIXE* for the characterization of *Madonna dei Fusi* by Leonardo da Vinci

PIXE is currently employed to perform elemental analysis of paintings [37, 4, 38, 39]. It allows to retrieve the stratigraphic composition without damaging the painting, making use of proton beams with different energies.

In the case of PIXE performed with particle accelerators, the analysis of paintings is particularly complex because the number of different elements present in the sample is generally very high, and they are distributed in a complex multilayer structure.

Moreover, elements emitting the detectable X-rays are generally present in trace and amid of an organic matrix (composed by O, H, N, etc. with a density  $\sim 1 \text{ g/cm}^3$ ). As a consequence, the number of detected X-rays is two orders of magnitude lower than for the case of metallic targets.

Finally, the probed thickness is higher than that related to metallic targets (the density is lower and so the projectile range is longer); then the emitted X-rays are generated along a more extended path.

All these considerations make it difficult to perform a real *Differential PIXE* with monoenergetic protons, that is, apply the iterative model described in Sec. 2.2.4 and get real concentration profiles.

In any case, as shown in [4], some considerations about the inhomogeneities of the composition can be made on the basis of the recorded spectra. In [4], the *Madonna dei fusi* (Leonardo da Vinci) [68] shown in fig. 5.11 is analyzed with PIXE: its structure is assumed to be a multilayer one, and the composition and thickness of the layers is estimated starting from the values of the yields experimentally measured.

Therefore, the goal of this section is to demonstrate that the same kind of analysis can be performed also employing a laser-driven proton source. To achieve this goal, performing a Monte Carlo simulation is prohibitive: the low values of the X-ray yields would imply to simulate a very large, and prohibitive, number of protons in order to get statistically valid results (to simulate  $10^9$  protons with a standard PC would require several weeks). In addition, the complexity of the structure does not guarantee that the iterative code converges on the correct concentration profiles. So, the adopted strategy does not involve the use of "synthetic experimental results" obtained with the Monte Carlo and the subsequent application of the developed model in order to retrieve the concen-



**Figure 5.11:** *Madonna dei Fusi* by Leonardo da Vinci.

trations. Only the theoretical models will be used to calculate the yield values, starting from the knowledge of the sample composition.

Here, the starting point are the information reported in [4] concerning the sample, which can be employed in order to reconstruct completely its composition. Anyhow, because of a certain lack of information regarding the organic fraction of the matrix (density, concentration, etc.), also some reasonable assumptions will be necessary. Then, the validity of the simulated sample structure can be tested using the model described in Sec. 2.2.3: from the assumed composition, the X-ray yields are evaluated and compared to the experimental ones reported in [4].

Employing the model developed in Sec. 4.1.3 and the same target composition, the values of the X-ray yield generated using a laser-driven proton source will be evaluated. Finally, it will be discussed whether the conclusions reported in the publication could also be derived using the yields obtained with laser-driven protons.

### **Experimental analysis of *Madonna dei Fusi* in literature**

The aim of the study reported in [4] is to retrieve the *Madonna dei fusi* (see fig. 5.11) stratigraphic structure, in particular considering the *incarnato* areas (hand and cheek of the Virgin, finger and lip of the Child). A single-ended Van de Graaff accelerator and a set of Upilex foils, as energy degraders, were employed in order to generate proton beams with energies from 1.2 to 2.8 MeV. Two Si(Li) detectors were used by the authors (one for the lower energy X-rays, one for the higher).

Like many others canvas paintings, *Madonna dei Fusi* is composed by a three layer structure:

- **A superficial protective varnish** composed mainly of organic material.
- **A layer of pigment** composed by lead white ( $2\text{PbCO}_3 \cdot \text{Pb}(\text{OH})_2$ ), cinnabar ( $\text{HgS}$ ) as red and binder (**organic**).
- **The imprimatura**, which is composed only by lead white (*biacca*) and binder.

The varnish composition is obtained employing protons with initial energy equal to 1.4 MeV. The spectrum is analyzed with the GUPIX software, as the 1.4 MeV protons are completely stopped before reaching the pigment and the analysis of the spectrum can be assimilated to that of a homogeneous sample. Fifteen different elements have been detected (among them are Na, Si, P, Ca, K, Fe, etc.), representing the 1 % inorganic fraction of the varnish. Besides, evaluating the proton range in an organic matrix and considering the initial proton energy for which the pigment characteristic X-rays are no longer present, the thickness of the varnish can be estimated to be about 50  $\mu\text{m}$ .

The characterization of pigment and *imprimatura* was made considering the ratio

between the Hg and Pb peak areas. Essentially the corresponding X-rays are characterized by having almost the same absorption coefficients (the energies at 9.9 keV for the  $L\alpha$  transition of Hg and 10.5 keV for the  $L\alpha$  transition of Pb are very closed to each other). Also, the X-ray production cross sections change in the same way, so the variation of this ratio is representative of the non-homogeneity of the sample.

Fig. 5.12 shows an example of the spectra recorded for the four different initial

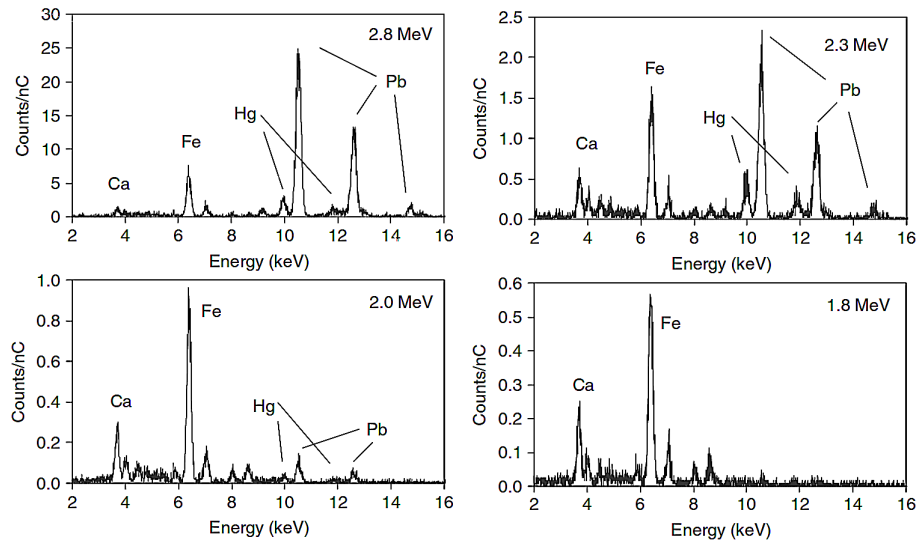


**Figure 5.12:** Spectra collected for four different energies on the hand of the Virgin (reproduced from [4])

**Table 5.3:** Ratio of the Hg over Pb peaks for different incarnato areas, reported in ref. [4].

Beam Energy (MeV)	1. Hand of the Virgin	2. Cheek of the Virgin	3. Finger of the Child	4. Lip of the Child
2.8	$0.10 \pm 0.01$	$0.11 \pm 0.01$	$0.061 \pm 0.002$	$0.23 \pm 0.01$
2.3	$0.23 \pm 0.02$	$0.16 \pm 0.02$	$0.074 \pm 0.003$	$0.26 \pm 0.01$
2.0	$0.25 \pm 0.06$	$0.16 \pm 0.03$	$0.084 \pm 0.012$	$0.33 \pm 0.05$
1.8	~	~	~	~

proton energies. The results listed in table 5.3 suggest the conclusions reported in the paper, which have been summarized here:

- Since up to 1.8 MeV for the initial beam energy the X-rays of Pb and Hg do not appear in the spectrum, from the calculation of the proton range we can deduce that the varnish thickness is about 50  $\mu\text{m}$ .

- In points 3 (finger of the Child) and 4 (Lip of the Child), the ratio decreases monotonously as the initial projectile energy increases. Protons with 2.8 MeV initial energy barely reach the *imprimitura*, so the pigment layer thickness can be estimated around 25  $\mu\text{m}$ . We also deduced that the inorganic pigment fraction is composed of 80-90% of lead white and 10-20% of cinnabar.
- In points 1 (hand of the Virgin) and 2 (Cheek of the Virgin), protons with initial energy equal to 2 and 2.3 MeV are completely stopped inside the pigment layer, while protons with 2.8 MeV initial energy reach the *imprimitura*. This is underlined by the sharp decrease in the ratio between the peaks ranging from 2.3 to 2.8 MeV. Essentially, the pigment contains both Hg and Pb and the ratio of their peaks at 2.3 MeV is representative of their relative concentration inside the pigment. Lead white is concentrated at 80-90 %, cinnabar at 10-20 % of the inorganic fraction. When protons reach the *imprimitura*, composed mainly by *biacca* and binder, the contribution of the *imprimitura* is added to the Pb peak generated by the lead white in the pigment. In other words, there is an increase in the X-ray yield of Pb due to the third layer and so a significant decrease in the ratio between the Hg and Pb peaks. So, the thickness of the pigment layer must be lower than 30  $\mu\text{m}$  and a minimum value, considering the range of 2.3 MeV protons, can be set at 10  $\mu\text{m}$ .

**Table 5.4:** *Modelling the composition of the painting in the four points considered in the analysis.*

Layer	Thickness ( $\mu\text{m}$ )	Upilex (%)	Water (%)	Cinnabar (%)	Lead white (%)
1. Hand of the Virgin					
Varnish	55	100	0	0	0
Pigment	10	0	30	11	59
<i>Imprimitura</i>	~	0	10	0	90
2. Cheek of the Virgin					
Varnish	55	100	0	0	0
Pigment	10	0	30	8	62
<i>Imprimitura</i>	~	0	10	0	90
3. Finger of the Child					
Varnish	50	100	0	0	0
Pigment	25	0	30	4.5	65.5
<i>Imprimitura</i>	~	0	10	0	90
4. Lip of the Child					
Varnish	50	100	0	0	0
Pigment	25	0	30	14	56
<i>Imprimitura</i>	~	0	10	0	90

### Comparison between experimental data and theoretical model results for monoenergetic protons

From the information reported in [4] and making some reasonable assumption, the sample composition in the four points can be reconstructed. It is assumed that the protective varnish can be modeled as Upilex, while the organic fractions of the paint layer and the *imprimitura* is substituted by water. In table 5.4 the assumed layer thicknesses and compositions for the four points are listed in detail.

Now, the model described in Sec. 2.2.3 for the multilayer target analysis can be applied by adopting the sample composition reported in table 5.4. Considering different proton initial energies, the behavior of the ratio between the Hg and Pb peaks can be evaluated and compared with the experimental results reported in table 5.3. This is done in fig. 5.13. For the blue continuous line, the sample composition is exactly equal to that reported in table 5.4, while the dotted line refers to the same kind of analysis, but without considering the additional contribution to the Pb yield given by the *imprimitura*. The experimental results shown in table 5.3 are also reported (red points).

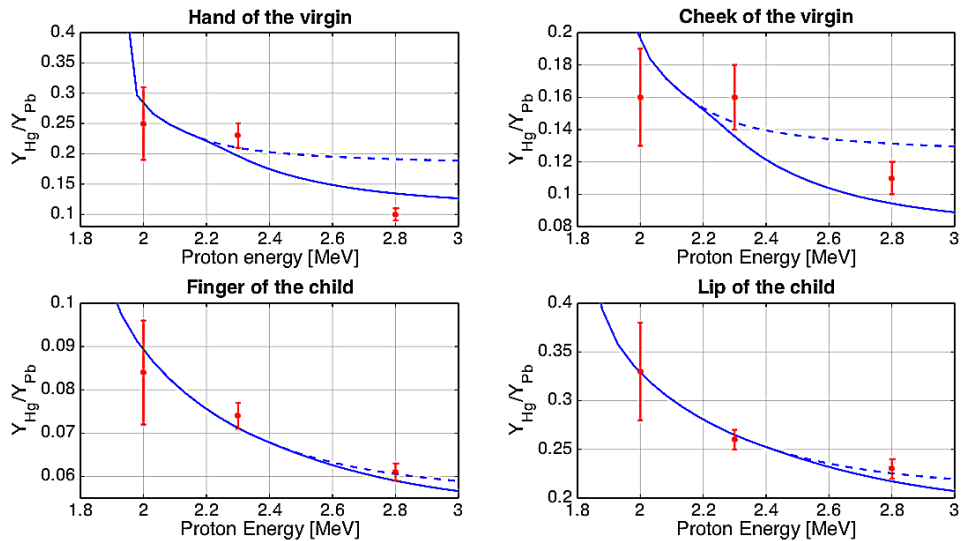


**Figure 5.13:** Comparison between the model result assuming exactly the sample composition reported in table 5.4 (continuous blue line), the model result without the *imprimitura* contribution to the Pb peak (dotted blue line) and the experimental result (red points) for monoenergetic protons.

The goal of this procedure is to show how the author's considerations are consistent with what experimentally observed even from a modeling point of view. In addition, if there is consistency between the model and the experimen-



tal data, the assumed composition could be used for a comparison with what would be obtained using non-monoenergetic protons.

As you can see, there is a reasonable agreement between the experimental data and the theoretical calculations. Of course the agreement is not perfect because of the complexity of the sample and the assumptions about the layers' composition. Considering point 1 and 2, by comparing the trend of the continuous and dashed line, it is possible to identify the energy for which the protons begin to penetrate into the *imprimitura*. This transition is coherent with the inflection shown by the experimental data.

Looking at point 3 and 4, the transition from the pigment to the *imprimitura* is almost imperceptible, in fact the continuous and dashed curve are practically superimposed. This is a consequence of the fact that, in these cases, the thickness of the pigment layer is 25  $\mu\text{m}$  (instead of the 10  $\mu\text{m}$  of points 1 and 2), so the contribution of the *imprimitura* to the Pb peak is less relevant and the transition is no longer evident.

### **Analysis with an exponential proton energy spectrum and comparison with the monoenergetic case**

The above-described analysis is based on the concept that protons with increasing energies will penetrate more into the material, allowing probing greater sample thicknesses. The transition from one layer to another along the protons' path is reflected on the measured yield which can then be used to derive information about the stratigraphic structure of the painting.

The same concept can be applied using laser-drive protons because the exponential energy spectrum is characterized by a well-defined cut-off energy value. So, changing the maximum energy in the spectrum, different layer thicknesses will be reached by the most energetic protons at each shot.

To compare the sensitivity of the analysis with monoenergetic protons and protons characterized by an exponential energy spectrum, the developed model for the case of non-monoenergetic primary particles described in Sec. 4.1.3 has been applied to this case, assuming the composition shown in table 5.4.

Here a simple exponential spectrum with temperature  $\alpha$  equal to 0.6  $\text{MeV}^{-1}$  is adopted and the ratio between the Hg and Pb yields is evaluated as a function of the maximum energy. The final result (red line) is shown in fig. 5.14 and it is compared to the case of monoenergetic protons (blue line).

The ratio of yields with and without the contribution to the lead peak from the third layer is translated upwards, but the difference between the dashed and continuous curves remains clear. So it is possible to assert that, performing the analysis using protons with an exponential energy spectrum and cut-off energy equal to that of the corresponding monoenergetic protons, the conclusions on the composition of the painting would be similar to those already reported for the monoenergetic case.

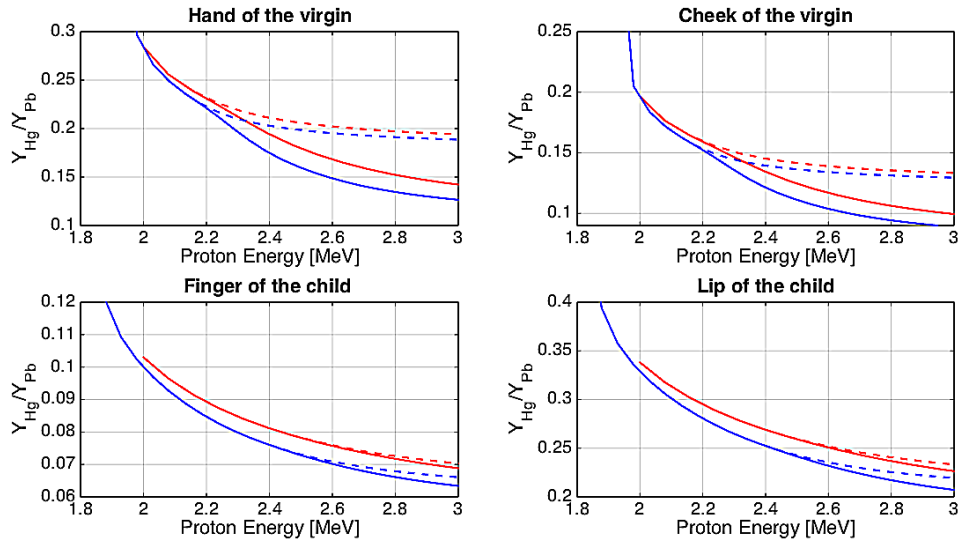


**Figure 5.14:** Comparison between model results for monoenergetic protons (blue lines) and protons with exponential energy spectrum (red lines).

## 5.2.2 PIGE for identification of Lapis-Lazuli in paintings

An example of PIGE complementarity with PIXE is offered by the analysis of paintings, particularly as regards to the identification of lapis-lazuli [69]. lapis-lazuli is a very precious pigment mainly composed by lazurite ( $\text{Na}_2\text{O} \cdot 3\text{Al}_2\text{O}_3 \cdot 6\text{SiO}_2 \cdot 2\text{Na}_2\text{S}$ ) with traces of calcite ( $\text{CaCO}_3$ ) and pyrite ( $\text{FeS}_2$ ). Usually it is mixed with lead white ( $2\text{PbCO}_3 \cdot \text{Pb}(\text{OH})_2$ ).

The  $K\alpha$  X-rays emitted by the light elements present in lapis-lazuli can be detected by PIXE, but unfortunately their peaks are often superimposed to those of the elements present in the varnish. Moreover, the presence of a significant amount of lead results in a high self-absorption of low-energy X-rays. Considering sodium, which can be regarded as a sort of fingerprint for lapis-lazuli, its peak at 1.04 keV is strongly absorbed by the varnish. The other elements can be present also in other kind of pigments.

In this scenario, a clear identification of the presence of lapis-lazuli through PIXE can be extremely difficult. One possible alternative is PIGE, in particular the detection of the  $\gamma$ -rays at 441 keV emitted by sodium in  $(p, p'\gamma)$  reactions.

In [69], the authors test the sensitivity of PIGE to the detection of lapis-lazuli by irradiating specimens characterized by different concentrations of pigment and varnish thicknesses. The goal is to identify the minimum value of pigment concentration which can be observed, measuring the  $\gamma$ -ray yield associated to sodium.

The goal of this paragraph is to test the sensitivity of PIGE performed with a

laser-driven proton source to recognize the presence of lapis-lazuli. A similar procedure to that followed in Sec. 5.2.1 is applied: starting from the data reported in [69], the sample composition is reconstructed. The model described in Sec. 2.4 for PIGE with monoenergetic protons is applied in order to retrieve the  $\gamma$ -ray yields. The calculated values are compared with the experimental results reported in the paper with the aim to check if the assumed sample composition can be considered reliable. This is necessary because of a certain lack of information in the paper about the sample composition.

Finally the same model derived in Sec. 4.1.3 for the description of PIXE with a non-monoenergetic proton source will be applied, but considering the PIGE cross-sections instead of the ionization ones and neglecting the photon attenuation. This procedure provides the  $\gamma$ -ray yields coming from the irradiation of the aforementioned samples with a laser-driven proton source. It is compared to that obtained with the monoenergetic proton source.

### **Analysis with monoenergetic protons**

The irradiated samples employed in [69] were produced specifically for the experiment with the following structure:

1. A superficial layer of Upilex for the simulation of the varnish with variable thickness of 0  $\mu\text{m}$ , 7.5  $\mu\text{m}$  and 15  $\mu\text{m}$ .
2. A second layer of thickness equal to 100  $\mu\text{m}$  and composed by lead white and lapis-lazuli. The blue pigment is characterized by a decreasing concentration in the different samples (5 %, 2 %, 1 % and 0.5 %).
3. A substrate entirely made of lead white.

These targets are irradiated with protons with energy equal to 2.7 MeV with a current of 10  $\div$  100 pA and for 300 s.  $\gamma$ -rays are recorded in a HpGe detector of thickness equal to 23 cm, placed at 135° with respect to the incident proton beam direction and with a subtended solid angle of 0.5 sr.

The final result is reported in fig. 5.17 (black points), where the  $\gamma$ -ray yields are plotted as a function of the percentage of lapis-lazuli and for the three different Upilex thicknesses. It is possible to conclude that the sensitivity of PIGE in detecting lapis-lazuli extends up to a concentration of 0.5 %.

### **Comparison between experimental data and theoretical model results for monoenergetic protons**

As in the case of PIXE for the analysis of paintings, the theoretical model for monoenergetic protons can be applied in order to reproduce the experimental results. The aim is to check the hypothesis made on the sample composition. In order to do that, the aforementioned assumptions need to be clarified:

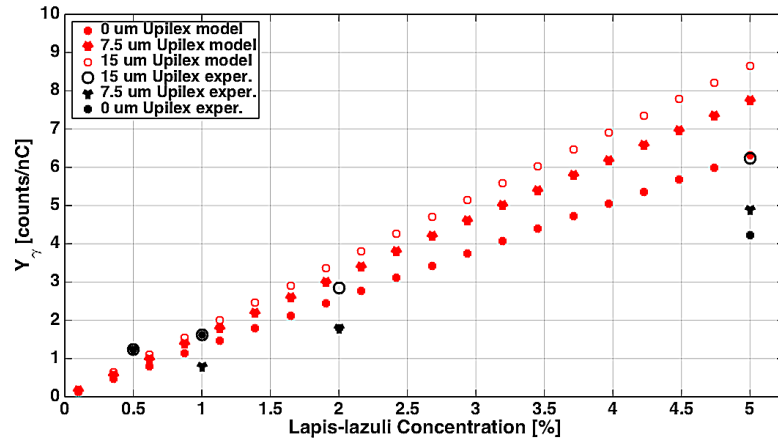


**Figure 5.15:** Comparison between publication results (black points) and theoretical results (red points).

- Sodium is present in the lazurite mineral with a mass fraction of 22 %. In turn, lazurite is diluted in lapis-lazuli at  $20 \div 30$  % (here it is assumed 25 %).
- The concentrations of lead white and binder are not specified. However, this does not affect the yields because they are only influenced by the first thick layer of Upilex and the concentration of lapis-lazuli.
- The detector efficiency is not reported. It can be anyway estimated on the basis of the geometry as shown in [70]. Assuming a radius of 30 mm for the detector and accepting an error of  $\pm 10$  %, the intrinsic efficiency can be evaluated as 60 %.
- The cross section for the  $(p,p'\gamma)$  reaction ( $E_\gamma = 441$  keV) employed is present in the IBANDL database and it is reported in fig 5.16.

Integrating the cross section along the proton range for different concentrations of lapis-lazuli, it is possible to obtain analytically the  $\gamma$ -ray yield (red points of fig. 5.15) and this can be compared with the results shown in the publication (black points). As shown in the graph, there is a good agreement between the experimental data and the theoretical model.

### Analysis with an exponential proton energy spectrum and comparison with the monoenergetic case

Finally, adopting the same sample configuration, it is possible to use the model for the calculation of the  $\gamma$ -ray yield introducing an exponential proton spectrum. The procedure is quite similar to the one described for the PIXE analysis in Sec. 4.1.3.

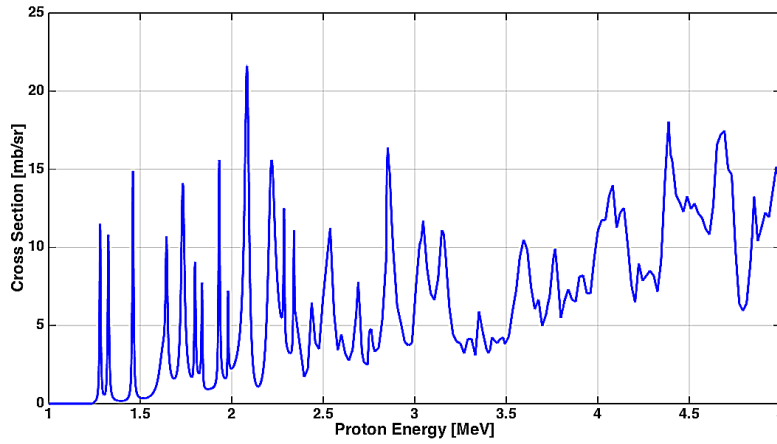


**Figure 5.16:** PIGE cross section for  $\text{Na}(p,p'\gamma)\text{Na}$  reaction,  $E_\gamma = 441 \text{ keV}$  at  $135^\circ$  from the IBANDL database.

Assuming an exponential energy spectrum with minimum energy equal to 1 MeV, a maximum energy of 5 MeV and a temperature  $\alpha$  equal to  $0.6 \text{ MeV}^{-1}$ , the  $\gamma$ -ray yield can be obtained for different lapis-lazuli concentrations. The resulting curve (blue points) is reported in fig. 5.17 and it is compared with the previously calculated data for the case of monoenergetic protons (red points). The  $\gamma$ -ray yields in the two cases, normalized with respect to the total number of incident protons, are practically the same.

It is possible to conclude that the analytical capability of PIGE in the detection of lapis-lazuli remains unchanged when an exponential proton energy spectrum is employed instead of a monoenergetic one.

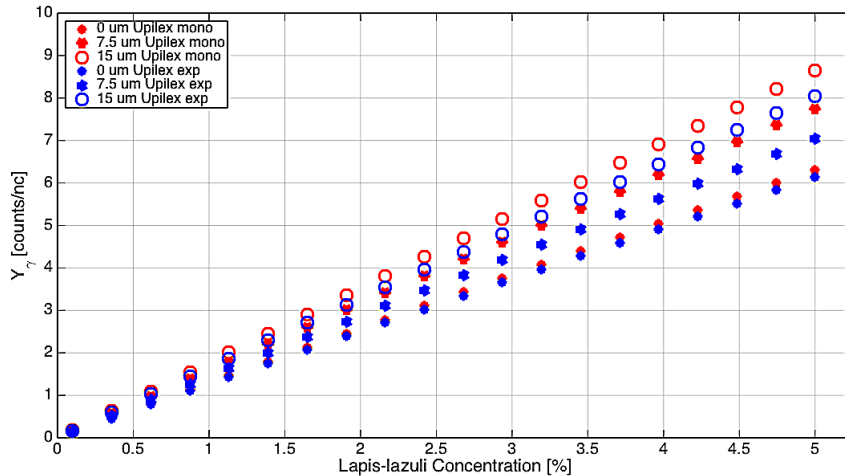


**Figure 5.17:** Comparison between the calculated  $\gamma$ -ray yield in the case of monoenergetic protons (red points) and protons with exponential energy spectrum (blue points).

## Chapter 6

# Conclusions

In this thesis, by means of an extensive numerical investigation, it is shown how the use of a non-monoenergetic proton source allows to retrieve the composition of a sample with the same sensitivity as a source of monoenergetic protons.

PIXE and PIGE are two very powerful Ion Beam Analysis techniques for the non-destructive elemental characterization of samples. They are based on the detection of the X-rays and  $\gamma$ -rays generated during the interaction with a monoenergetic proton beam, generated by a particle accelerator (usually a large and expensive machine). A laser-driven proton source would be more compact and less expensive with respect to a particle accelerator.

The theoretical models currently available in literature for the quantitative interpretation of PIXE measurements are based on the assumption of a monoenergetic proton spectrum (Sec. 2.2). Accordingly, the innovative part of this thesis is the development of suitable models for the analysis of PIXE spectra that consider employing protons obtained with a non-monoenergetic spectrum (Sec. 4.1). This is done in a wide variety of cases, encompassing the main scenarios studied for PIXE. In some cases the goal of the analysis is to retrieve sample elemental composition, in others it is to recover the concentration profiles.

The models are used to write an iterative code able to return the sample composition starting from experimental X-ray spectra. Exploiting "synthetic" spectra obtained with Monte Carlo simulations, the validity of these codes is verified (Sec. 4.3). This also confirms the validity of the models developed in the first part of the thesis.

In all cases, the iterative codes recover the composition used as Monte Carlo input with great accuracy. It is concluded that the developed models and the associated iterative codes are suitable for analyzing PIXE spectra generated using a non-monoenergetic proton source. In this first set of Monte Carlo simulations, the non-monoenergetic proton spectrum is shaped as a pure exponential.

PIXE carried out on the same samples, but considering mononenergetic proton beams, is simulated. A total number of protons comparable to that employed in aforementioned simulations is used. Comparing the results in terms of elemen-

tal concentrations and thicknesses, it can be stated that the analysis performed with monoenergetic protons and with an exponential energy spectrum show the same accuracy.

As reported in Sec. 4.3.6, laser-driven proton sources are able to provide in a single bunch a number of protons comparable to those currently employed to perform PIXE with particle accelerators. Since in the case of laser-driven PIXE the X-rays are emitted in a time window of some nanoseconds, traditional Si(Li) detectors are unsuitable because of their poor temporal resolution. A possible alternative could be a Von Hamos spectrometer, a passive detector based on the presence of a crystal.

A last more realistic case is studied (Sec. 5.1), simulating explicitly with the Monte Carlo the presence of the Von Hamos detector. Moreover, because of the necessity to test the developed models on data generated employing a realistic laser-driven proton source, the proton energy spectrum inserted in the simulation is the result of a Particle in Cell (PIC) simulation in turn.

Also in this case, the analysis of the simulation outputs with the developed models confirms the possibility to perform PIXE with a laser driven-proton source. It is possible to conclude that a Von Hamos spectrometer is suitable to record the X-ray spectra when a laser driven proton source is employed and the analysis can be carried out using a single proton bunch. Moreover, as far as the proton source properties are concerned, the results show a negligible dependency on the proton spectrum details. In particular, by approximating the PIC spectrum with an exponential in the iterative code, the same results are obtained. In addition, at least in terms of the elemental composition, the results have a very weak dependency with respect to the spectrum temperature value.

The final objective of this work is to study the application of laser-driven PIXE to the field of cultural heritage, in particular to assess if a laser-driven proton source can be employed in order to determine the composition of paintings through PIXE and PIGE.

As far as PIXE is concerned, the study of the multilayer structure of *Madonna dei fusi* (Leonardo da Vinci) presented in [4] is taken as a reference. In this paper, the authors irradiate the painting with protons having different energies. The X-ray yields of each spectrum are representative only of the composition of the layers in which protons go through. Besides, the relative concentration of the elements changes passing from one layer to another. So looking at the ratio of the corresponding X-ray peaks as a function of the energy, the authors are able to estimate the thicknesses of the layers, as well as their composition. In Sec. 5.2.1, the *Madonna dei Fusi* multilayer composition is reconstructed starting from the information reported in [4]. Then, the developed model is used to estimate the aforementioned ratio. This is done considering different maximum values in the exponential proton energy spectrum. Also in the case of laser-driven protons, the ratio between the X-ray yields shows a dependency which is representative of the non-homogeneous distribution of the elements in the layers of the painting.

The conclusion is that PIXE, performed with a laser-driven proton source instead of with monoenergetic protons, keeps its analytical capability in the characterization of paintings.

As far as PIGE is concerned, in [69] the sensitivity of PIGE, performed with monoenergetic protons, in the identification of lapis-lazuli is tested. In order to do that, the minimum detectable value of the  $\gamma$ -ray yield is evaluated experimentally as a function of the lapis-lazuli concentration. Then in this work, the corresponding values obtained employing a laser-driven proton source are evaluated using the developed model (Sec. 5.2.2). It is possible to assert that laser-driven PIGE has the same sensitivity in the detection of lapis-lazuli of conventional PIGE performed with monoenergetic protons.

## 6.1 Perspectives and open issues

A natural extension of this work is to perform a real experiment of laser-driven PIXE/PIGE. The models developed in this thesis could be used to retrieve the composition of a sample from the experimental x-ray/gamma-ray spectra. In this framework, an experimental campaign has been proposed at the 100 TW laser facility CLPU (Salamanca, Spain). The goal will be to characterize the multilayer structure of prepared samples and demonstrate for the first time the possibility to perform a *Differential PIXE* analysis with laser-driven protons. On the other hand, another interesting prospective is to test laser-driven PIXE / PIGE using a compact laser source of few 10s TW.

Concerning the open issues, it would be beneficial for laser-driven PIXE to find alternative detection systems, characterized by a higher detection efficiency with respect the Von Hamos configuration proposed in this thesis. Although it has been proved that the Von Hamos spectrometer can be used in order to perform a measurement with a single shot, the low efficiency of the crystal drastically reduce the recorded X-ray yields. As a result, about  $10^{11}$  protons are needed to conduct the analysis of a homogeneous target. This number can be reduced increasing the efficiency of the detection system and this would imply to use less powerful and expensive lasers.

Finally, it will be necessary to study of the possible thermal damage induced on the target by the proton bunch. This is of particular importance when the samples are paintings or historical artifacts. Promising results have been obtained in [1], but will be necessary to further verify the damage irradiating samples which simulate the original archaeological finds.



# Appendix A

## Cross section

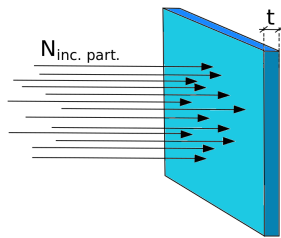


**Figure A.1:** *Particle beam orthogonally incident on a thin target.*

The cross section is a quantity used to describe an interaction process between particles, quantifying the probability that an initial state will be transformed into a different final state. It is a specific quantity for each process and it has the dimension of an area. The unit of measure is the *barn*, which is equal to  $10^{-24}$   $\text{cm}^2$ .

In order to derive the expression of the cross section, the starting point is to consider a thin target of thickness  $t$  (cm), mass density  $\rho$  ( $\text{g}/\text{cm}^3$ ) and mass number  $A$ . A particle beam is made to impinge orthogonal to the surface with total number of particles equal to  $N_{\text{inc. part.}}$ .

The target is "thin" in the sense that only a small fraction of the incident particles will interact with it. If we assume also that the interaction probability depends on the properties of the projectiles and target atoms, we can say that:

1. The number of interactions  $N_{\text{events}}$  is proportional to the number of the incident primary particles  $N_{\text{inc. part.}}$ .
2. The number of interactions  $N_{\text{events}}$  is proportional to the target thickness  $t$ .
3. The number of interactions  $N_{\text{events}}$  is proportional to the target density  $\rho$ .

Under the above hypothesis, we can write:

$$N_{\text{events}} = N_{\text{inc. part.}} \cdot nt \cdot \sigma \quad (\text{A.1})$$

where  $n = \rho N_{\text{Avog}}/A$  (atoms/ $\text{cm}^3$ ) is the target number density,  $nt$  (atoms/ $\text{cm}^2$ ) is the areal density and  $\sigma$  is a constant with a dimension of area (cm), called cross section.

So, the cross section for a particular process is given by the following equation:

$$\sigma = \frac{N_{\text{events}} \cdot A}{N_{\text{inc. part.}} \cdot \rho t \cdot N_{\text{Avog}}} \quad (\text{A.2})$$

Equivalently, assuming that the primary particle flux is uniformly distributed along the width of the beam, the cross section can be defined as:

$$\sigma = \frac{(\text{n}^\circ \text{ of events})}{(\text{n}^\circ \text{ of particle per unit area}) \cdot (\text{n}^\circ \text{ of target particles})} \quad (\text{A.3})$$

The number of events can be restricted to the case that an outgoing particle goes in a certain range of angles in spaces. In this case we can speak of differential cross section, i.e. cross section per unit solid angle:

$$\frac{d\sigma}{d\Omega} = \frac{N_{\text{events in } \Delta\Omega}}{N_{\text{inc. part.}} \cdot nt \cdot \Delta\Omega} \quad (\text{A.4})$$

In A.4,  $d\Omega = \sin\theta d\theta d\phi$  is the infinitesimal solid angle measured in steradians (srd).

## A.1 Rutherford scattering cross section

Here it is reported a very simple example of cross section calculation, in particular the case of Rutherford collision (the scheme is reported in fig. A.2).

Consider a projectile having mass  $M_1$ , charge  $Z_1$  and initial energy  $E_0$  moving with velocity  $v_1$  which scatters with an atom of mass  $M_2$  at rest and charge  $Z_2$ . Assuming to have an elastic Coulomb scattering collision, the distance  $d$  of the closest approach during the interaction is given by:

$$d = \frac{Z_1 Z_2 e^2}{4\pi\epsilon_0 E_0} \quad (\text{A.5})$$

while the impact parameter  $b$  can be simply evaluated from the conservation of energy and momentum, giving:

$$b = \frac{Z_1 Z_2 e^2 \cot(\theta/2)}{4\pi\epsilon_0 M_1 v_1^2} = \frac{Z_1 Z_2 e^2 \cot(\theta/2)}{8\pi\epsilon_0 E_0} = \frac{d}{2} \cot(\theta/2) \quad (\text{A.6})$$

In order to derive the Rutherford scattering cross section we have to start considering the probability to have an impact parameter between  $b$  and  $b + db$ , which is proportional to the area  $d\sigma$  of the ring of thickness  $db$ :

$$d\sigma = 2\pi b(db) \quad (\text{A.7})$$

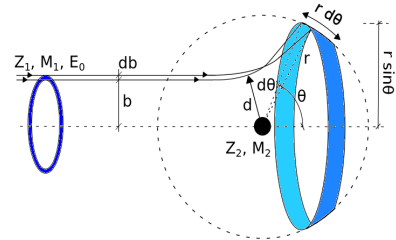


**Figure A.2:** Dependence of scattering on the impact parameter  $b$ .

Considering a primary particle flux  $N$  (n° of particles/cm<sup>2</sup>s) incident on the sample, the number of particles per unit time  $dN$  which is scattered between the angles  $\theta$  and  $\theta + d\theta$  is exactly:

$$\frac{dN}{N} = 2\pi b(db) = d\sigma \quad (\text{A.8})$$

So  $d\sigma$  is by definition the *differential cross section*:

$$\frac{d\sigma}{d\Omega} = \frac{\text{Number of particles scattered per unit time into } d\Omega}{\text{Number of particles incident per unit time and unit area}} \quad (\text{A.9})$$

The impact parameter  $b$  is a one-to-one function of the scattering angle  $\theta$  (see eq. A.6), so we can express also  $d\sigma$  as a function of  $\theta$ :

$$\begin{aligned} d\sigma &= 2\pi b(db) = 2\pi \left( \frac{Z_1 Z_2 e^2}{8\pi\epsilon_0 E_0} \right)^2 \cot(\theta/2) \operatorname{cosec}^2(\theta/2) d\theta \\ &= 2\pi \left( \frac{Z_1 Z_2 e^2}{8\pi\epsilon_0 E_0} \right)^2 \frac{1}{2} \frac{\cos(\theta/2)}{\sin^3(\theta/2)} d\theta \\ &= \left( \frac{Z_1 Z_2 e^2}{8\pi\epsilon_0 E_0} \right)^2 \frac{2\pi}{4} \frac{2 \sin(\theta/2) \cos(\theta/2) d\theta}{\sin^4(\theta/2)} \\ &= \left( \frac{Z_1 Z_2 e^2}{16\pi\epsilon_0 E_0} \right)^2 \frac{d\Omega}{\sin^4(\theta/2)} \end{aligned} \quad (\text{A.10})$$

where  $d\Omega = 2\pi \sin\theta d\theta$  is again the infinitesimal solid angle. From A.10, the differential scattering cross section in the center of mass frame can be derived:

$$\left( \frac{d\sigma}{d\Omega} \right)_{c.m.} = \left( \frac{Z_1 Z_2 e^2}{16\pi\epsilon_0 E_0} \right)^2 \frac{1}{\sin^4(\theta/2)} \quad (\text{A.11})$$

To switch from the center of mass frame to the laboratory frame, we have to consider that a cross-sectional area do not change passing from an inertial reference system to another:

$$\frac{d\sigma(\theta_{lab})}{d\Omega} d\Omega = \frac{d\sigma(\theta_{c.m.})}{d\Omega'} d\Omega' \quad (\text{A.12})$$

This equation can be rewritten as:

$$\frac{d\sigma(\theta_{lab})}{d\Omega} = \frac{d\sigma(\theta_{c.m.})}{d\Omega'} \frac{d\Omega'}{d\Omega} = \frac{\sin\theta_{c.m.}}{\sin\theta_{lab}} \frac{d\theta_{c.m.}}{d\theta_{lab}} \frac{d\sigma(\theta_{c.m.})}{d\Omega'} \quad (\text{A.13})$$

Combining eq. A.11 and A.13 and making some calculations, the Rutherford scattering cross section in the laboratory frame can be expressed as:

$$\left( \frac{d\sigma}{d\Omega} \right)_{lab} = \left( \frac{Z_1 Z_2 e^2}{8\pi\epsilon_0 E_0} \right)^2 \frac{1}{\sin^4\theta} \frac{\left[ M_2 \cos\theta + (M_2^2 - M_1^2 \sin^2\theta)^{1/2} \right]^2}{M_2 (M_2^2 - M_1^2 \sin^2\theta)^{1/2}} \quad (\text{A.14})$$

## Appendix B

# Von Hamos detection system

The Von Hamos detector employed in [71] is composed by a Highly Annealed Pyrolytic Graphite (HAPG) mosaic crystals, the radius  $R_c$  is equal to 150 mm and the distance between layers  $d$  is 3.356 Å. The integral reflectivity is also reported in fig. B.1. In the present work, as well as in [71], only the first order of reflection ( $n = 1$ ) is considered.

Essentially, once it is guaranteed that the crystal covers the spectral band of interest, the position of the cylinder and the screen are evaluated on the basis of Bragg's law (eq. 5.1 of Sec. 5.1.3) and on simple geometric considerations.

The distance between the X-ray source and the cylinder frontal edge  $d_1$  (see fig. 5.4 of Sec. 5.1.3) is fixed by Bragg reflection for the X-rays with the lowest energy.

Another aspect that needs to be taken into account is the fact that the X-rays, after the first reflection on the internal surface of the crystal, must be able to exit without being reflected again.

Accordingly, the maximum longitudinal dimension of the cylinder  $d_2$  is fixed by this condition.

In order to cover an energy range starting from 3 MeV to 11 MeV, three different cylindrical crystals are placed in front of the sample. All three are oriented towards the X-ray source, and they are parallel to the optical axis.

The same applies to the screens. They are positioned at a distance from the cylinder frontal edges so that the X-rays form circles with radii that are not higher than  $R_c$ . Two screens are placed before the focal point and one after it.

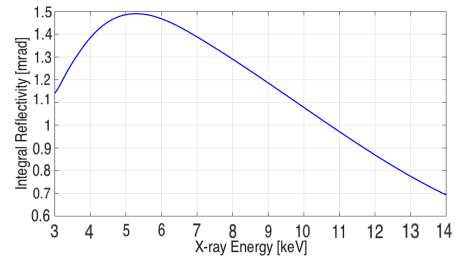


**Figure B.1:** *Integral reflectivity of the crystal.*

## B.1 X-ray registration

Considering in detail the Monte Carlo code, the X-ray measurement process was modeled as follows:

1. The X-ray is emitted from a certain position  $\mathbf{P}$  of radial and angular coordinates  $(r, \phi)$  on the target surface.
2. If the X-ray arrives on the inner surface of the cylinder, both the probability that it impinges on the correct angle and that the reflection occurs need to be evaluated. These two chances are accounted for by the efficiency of the crystal, evaluated from the integral reflectivity  $\rho$  by the following formula (see ref. [72]).

$$eff(E_x) = \frac{\rho}{2} \sin^2(\theta(E_x)) \quad (\text{B.1})$$

Because the angle of incidence can be written as a function of the X-ray energy through the application of the Bragg and Planck laws, the efficiency can be expressed as a function of the X-ray energy  $E_x$  and it can be applied in the simulation using the Inverse Transform Sampling method (see Sec. 4.2.3).

3. The application of the crystal efficiency determines whether the X-ray is reflected successfully. If it is the case, the position on the screen where the photon comes is calculated from  $\theta$ , the coordinates of  $\mathbf{P}$  and  $\beta$  (see fig. B.2).

## B.2 X-ray reflection

After the procedure described in Sec. B.1, the X-ray is considered as detected on the screen. The angle of incidence  $\theta$  and the coordinates of the point from which the photon is emitted from the target surface  $\mathbf{P}$   $(r, \phi)$  are provided to an analysis class. Here the position on the screen where the X-ray is reflected by the crystal is evaluated.

As long as it is possible to consider the source as punctual and placed on the optical axis of the crystal, the procedure needed to calculate the position on the screen after reflection involves only simple goniometric calculations. In our case the X-ray source is not punctual, but it has a finite dimension because the proton beam is characterized by a divergence angle distribution. So the X-ray can also be emitted off-axis.

The procedure necessary to evaluate the reflection point considering the case of a non-point source is not trivial and it was first described in [73]. In that article the author considers a configuration where the screen is parallel to the optical axis of the crystal (like in fig. 5.3 of Sec. 5.1.3) and the source is a segment lying on the same plane of the screen (so  $r \neq 0$  and  $\phi = 0$  in fig. B.2).

In this work, a procedure similar to that described in [73] is developed, in order to consider the more general case of an arbitrary source point reflected by a cylindrical crystal on a vertical screen. Here, only the fundamental points of the process which has been introduced are explained. The X-rays starting from

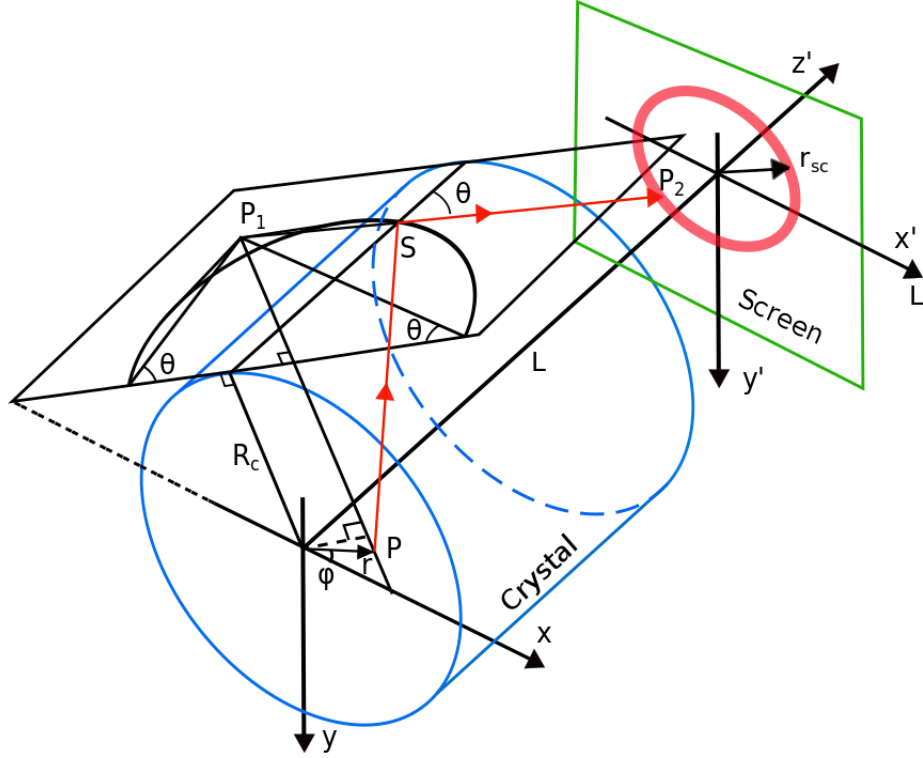


**Figure B.2:** Full-cylinder Von Hamos reflection scheme.

a point  $\mathbf{P}$  and reflected by a crystal (red line) behave as they are originated from  $\mathbf{P}_1$  of coordinates  $(x_1, y_1)$  in the plane with  $z_1 = 0$ :

$$x_1 = r \left[ \cos \phi + \frac{\sin \phi}{\cos \beta} \sin \beta \right] - \left\{ 2 \left[ R_c + r \left( \cos \phi + \frac{\sin \phi}{\cos \beta} \sin \beta \right) \sin \beta \right] - r \frac{\sin \phi}{\cos \beta} \right\} \sin \beta \quad (\text{B.2})$$

$$y_1 = 2 \left\{ R_c + r \left[ \cos \phi + \frac{\sin \phi}{\cos \beta} \sin \beta \right] \sin \beta \right\} \cos \beta \quad (\text{B.3})$$

The coordinates of the reflection point  $\mathbf{S}$  in the  $(x, y, z)$  reference system are:

$$x_s = -R_c \sin \beta \quad (\text{B.4})$$

$$y_s = R_c \cos \beta \quad (\text{B.5})$$

$$z_s = \left\{ \left[ \left( R_c + r \left( \cos \phi + \frac{\sin \phi}{\cos \beta} \sin \beta \right) \sin \beta - r \frac{\sin \phi}{\cos \beta} \right) \cot \theta \right]^2 - \left[ r \left( \cos \phi + \frac{\sin \phi}{\cos \beta} \sin \beta \right) \cos \beta \right]^2 \right\}^{1/2} \quad (\text{B.6})$$

Then, the coordinates of  $\mathbf{P}_2 (x_2, y_2)$  on the screen placed at a distance  $L$  from the emitting surface is found considering the equation of the straight line passing by  $\mathbf{P}_1$  and  $\mathbf{S}$ , and making the intersection with the  $z = L$  plane:

$$\frac{x_2 - x_1}{x_s - x_1} = \frac{y_2 - y_1}{y_s - y_1} = \frac{L - z_1}{z_s - z_1} \quad (\text{B.7})$$

### Detector resolution and calibration

The energy resolution of the crystal, as reported in [71], is of the order of some eV for a point-like X-ray source. For the experimental set up considered, the resolution is mainly influenced by the fact that the source is not punctual: the presence of X-rays not emitted exactly from the crystal axis causes a broadening of the circles and, therefore, also of the peaks, (see fig. 5.6, 5.7, 5.8 of Sec. 5.1.4).

This effect is strictly connected with the dimension of the X-ray source and consequently with the distance between the sample and the proton point-like source: increasing the distance, due to the proton beam divergence, also the spot size on the probed target becomes larger.

In this work, setting a distance of 4 cm between the proton source and the sample, the resolution of the system comes out to be high enough to distinguish the different X-ray lines.

As far as the system calibration is concerned, it is necessary to associate each circle with the corresponding energy of the X-ray peak. First, considering that the center of the circles lies on the crystal optical axes and knowing the geometry of the system, the radius on the screen  $r_{sc}$  can be evaluated for a certain angle of grazing incidence  $\theta$ :

$$r_{sc} = \pm \left( R_c - \tan \theta (L - R_c \tan \theta) \right) \quad (\text{B.8})$$

where  $R_c$  and  $L$  are the crystal radius and its length.

Eq. B.8 is applied with the sign  $+$  if the screen is in the pre-focus or with the sign  $-$  if it is in the post-focus. To a certain value of  $\theta$  corresponds a value of the wavelength  $\lambda$  because of the Bragg law (eq. 5.1), and therefore also of the X-ray energy  $E_x$ .

This simple considerations, bearing in mind that the screen may be located before or after the focal spot, allow you to calibrate the detector.

# Appendix C

## Block diagrams

### C.0.1 Histograms of the codes

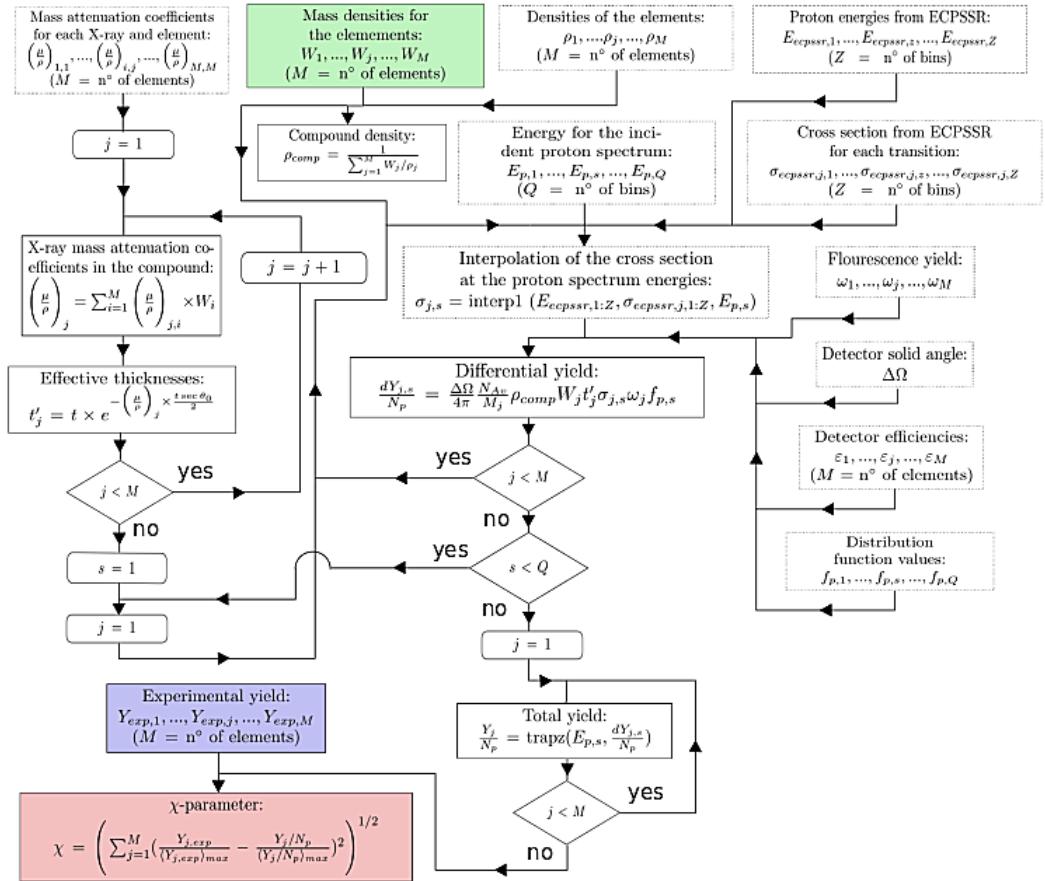


Figure C.1: Block diagram of the code for the thin target analysis.



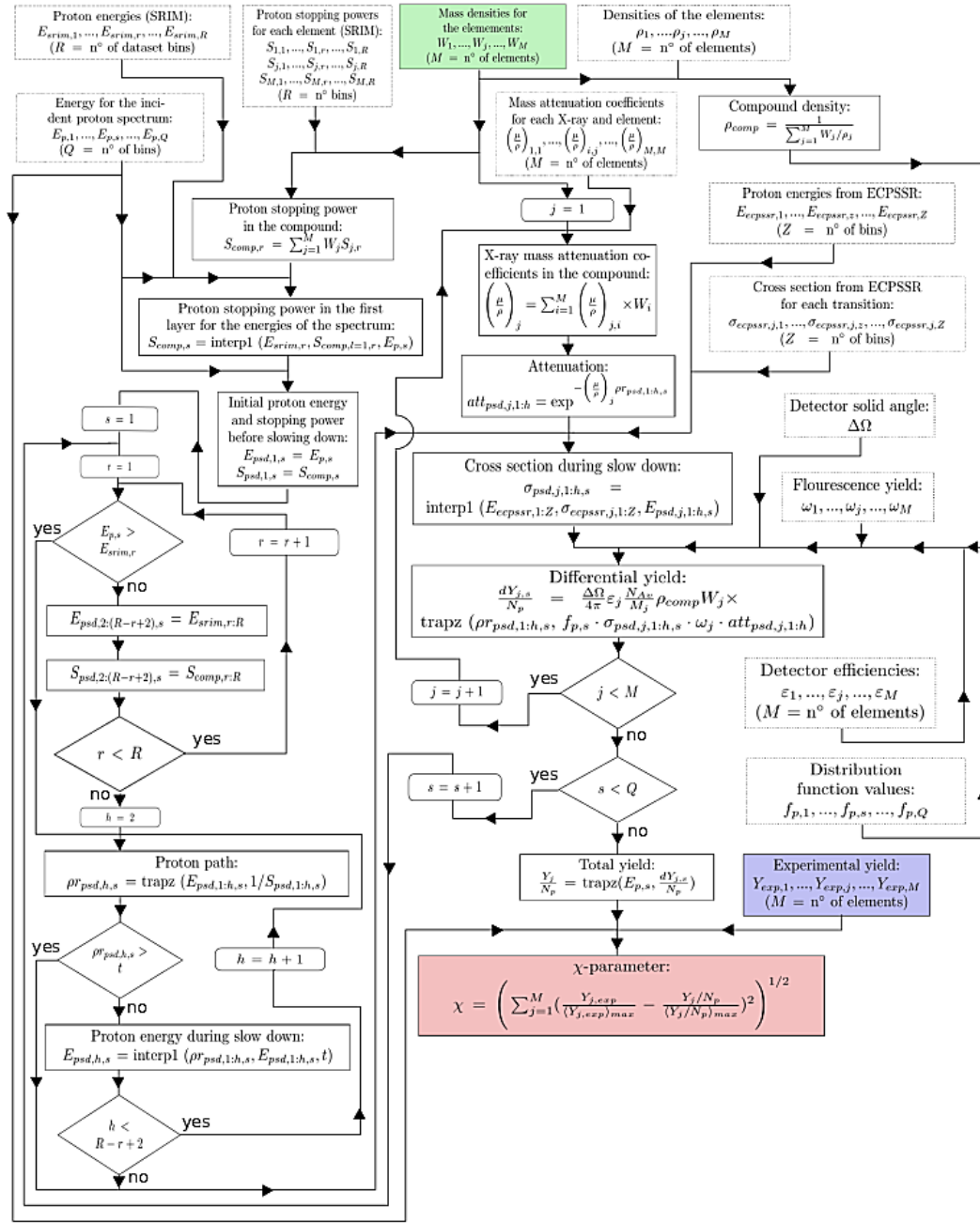


Figure C.2: Block diagram of the code for the thick homogeneous target analysis.

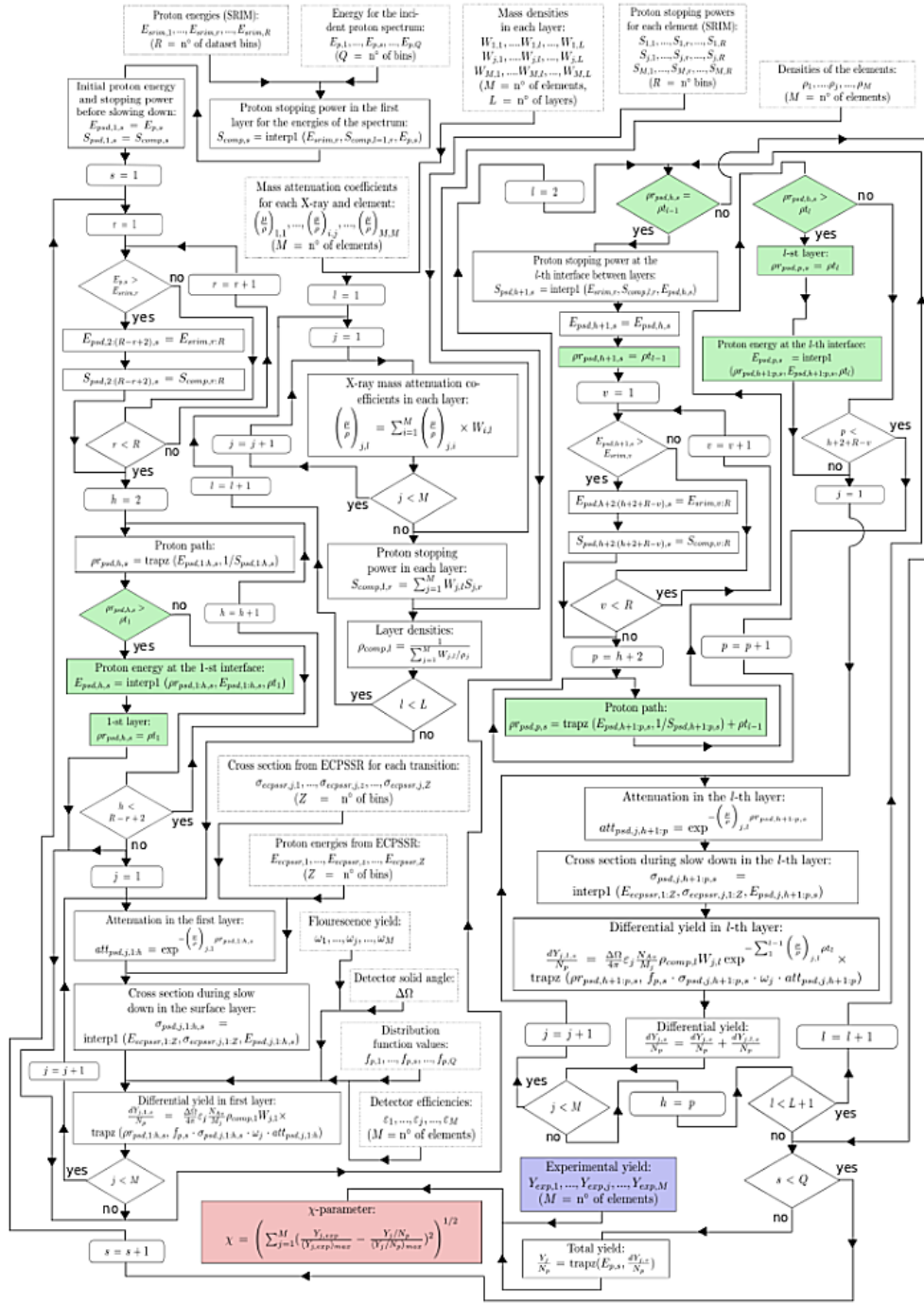


Figure C.3: Block diagram of the code for the Multilayer analysis.

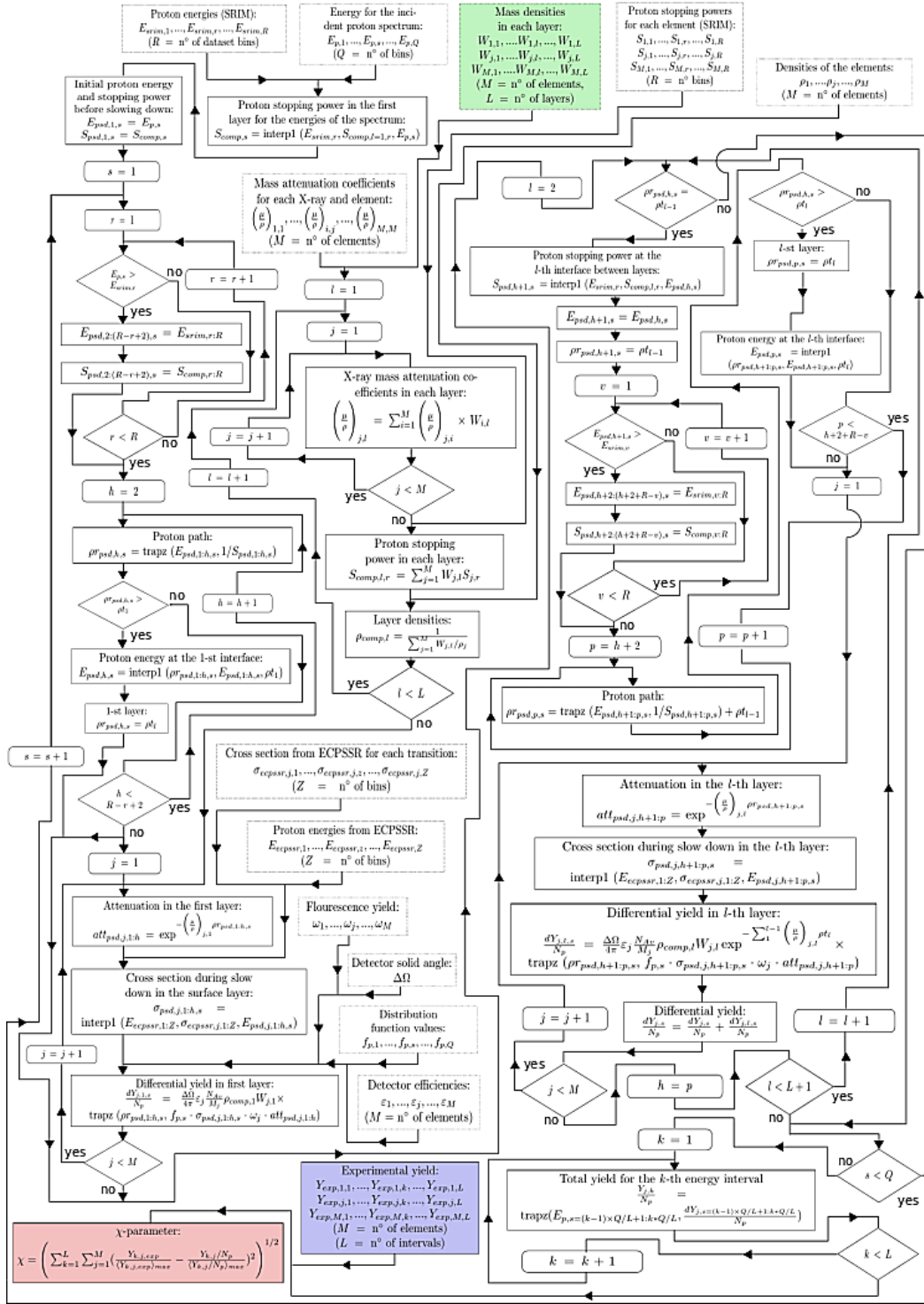


Figure C.4: Block diagram of the code for the Differential analysis.

### C.0.2 Databases

- The ionization cross sections employed have been derived from the Perturbed Stationary State Theory with Energy loss, Coulomb deflection, and relativistic effects (ECPSSR) [74, 75].
- The fluorescence yields can be found in the Evaluated Atomic Data Library (EADL) [76].
- The X-ray mass absorption coefficients can be calculated from the X-COM program [77].
- Proton stopping powers are calculated with The Stopping and Range of Ions in Matter (SRIM) program [78, 79].
- The Livermore Evaluation Atomic Data Library EADL [80, 81] contains the fluorescence yields.

# Bibliography

- [1] M. Barberio: *Laser-Accelerated Proton Beams as Diagnostics for Cultural Heritage*, 2017
- [2] Ľ. Šmit: *Differential PIXE measurements of thin metal layers*, 2004
- [3] A. Climent-Font: *Quantification of sodium in ancient Roman glasses with ion beam analysis*, 2008
- [4] P. A. Mandò: *Differential PIXE measurements for the stratigraphic analysis of the Madonna dei Fusi by Leonardo da Vinci*, 2005
- [5] H. R. Verna: *Atomic and Nuclear Analytical Methods*, Springer
- [6] C. Jeynes: *ION BEAM ANALYSIS : A CENTURY OF EXPLOITING THE ELECTRONIC AND NUCLEAR STRUCTURE OF THE ATOM FOR MATERIALS CHARACTERISATION*, 2011
- [7] L. Giuntini: *A review of external microbeams for ion beam analyses*, 2011
- [8] Rene Van Grieken, A. Markowicz: *Handbook of X-Ray Spectrometry, Second Edition*, CRC Press, 27 nov 2001
- [9] M. Steven Shackley: *An Introduction to X-Ray Fluorescence (XRF) Analysis in Archaeology*, 2010
- [10] Thomas B. Johansson: *Elemental trace analysis of small samples by proton induced x-ray emission*, 1975
- [11] Mitchell, I.V.: *Particle induced X-ray emission analysis application to analytical problems* , 1981
- [12] Sven A. E. Johansson: *Particle induced X-ray emission and complementary nuclear methods for trace element determination. Plenary lecture*, 1992
- [13] Paul van der Heide: *X-Ray Photoelectron Spectroscopy: An Introduction to Principles and Practices*, 2011
- [14] Noel H. Turner: *Surface analysis: x-ray photoelectron spectroscopy, Auger electron spectroscopy and secondary ion mass spectrometry*, 1984

- [15] Noel H. Turner: *Surface analysis: x-ray photoelectron spectroscopy and Auger electron spectroscopy*, 1988
- [16] R. Shimizu: *Quantitative Analysis by Auger Electron Spectroscopy*, 1983
- [17] H.Niehus: *Quantitative aspects of Ion Scattering Spectroscopy (ISS)*, 1975
- [18] M. Aono: *Quantitative Surface Atomic Structure Analysis by Low-Energy Ion Scattering Spectroscopy (ISS)*, 1985
- [19] M. Aono: *RECENT DEVELOPMENTS IN LOW-ENERGY ION SCATTERING SPECTROSCOPY (ISS) FOR SURFACE STRUCTURAL ANALYSIS*, 1989
- [20] A.Benninghoven: *Surface investigation of solids by the statical method of secondary ion mass spectroscopy (SIMS)*, 1973
- [21] A.Benninghoven: *Secondary Ion Mass Spectrometry SIMS V*, 1985
- [22] A.Benninghoven: *Secondary ion mass spectrometry: basic concepts, instrumental aspects, applications and trends*, 1987
- [23] Evtim V.Efremov: *Achievements in resonance Raman spectroscopy: Review of a technique with a distinct analytical chemistry potential* 2008
- [24] P. Roustron; *Raman Spectroscopy, a review*, 2016
- [25] G. H. Michler: *Electron Microscopy of Polymers*, 2008
- [26] J. I. Goldstein: *Scanning Electron Microscopy and X-Ray Microanalysis: A Text for Biologists, Materials Scientists, and Geologists*, Plenum Press
- [27] DUANE M. MOORE: *X'Ray Diffraction and the Identification and Analysis of Clay Mineral*, OXFORD UNIVERSITY PRESS, 1997
- [28] R. Jenkins: *Nomenclature system for X-ray spectroscopy*, 1991
- [29] <https://chepec.se/2014/09/13/xray-line-energies.html> 2014
- [30] Website: <http://pixe.physics.uoguelph.ca/gupix/main/>, J.L. Campbell
- [31] Website: <http://nmp.csiro.au/Geopixe.html>, C. Ryan
- [32] K. S. Johnson: *Aerosol composition and source apportionment in the Mexico City Metropolitan Area with PIXE/PESA/STIM and multivariate analysis*, 2006
- [33] W. MAENHAUT: *PIXE ANALYSIS OF AEROSOL SAMPLES COLLECTED OVER THE ATLANTIC OCEAN FROM A SAILBOAT*, 1981

- [34] C. G. Ryan: *Quantitative Analysis of PIXE Spectra in Geoscience Applications*, 1990
- [35] W. Maenhaut: *Particle-induced x-ray emission (PIXE) analysis of biological materials: Precision, accuracy and application to cancer tissues*, 1980
- [36] Ō. Šmit: *Metal analysis with PIXE: The case of Roman military equipment*, 2005
- [37] C. Neelmeijer: *Paintings — a Challenge for XRF and PIXE Analysis*, 2000
- [38] N. Grassi: *Differential and scanning-mode external PIXE for the analysis of the painting “Ritratto Trivulzio” by Antonello da Messina*, 2009
- [39] N. Grassi: *PIXE analysis of a painting by Giorgio Vasari*, 2009
- [40] Website: <http://www.srim.org/>, J. F. Ziegler
- [41] R. Kaur: *Quantitative Analysis of soil samples using PIGE technique*, 2010
- [42] R. Mateus: *A code for quantitative analysis of light elements in thick samples by PIGE*, 2004
- [43] Robert J. Van De Graaf: *Electrostatic generator*, feb 1935. US Patent 1,991,236.
- [44] J. D. Cockcroft and E. T. S. Walton: *Artificial production of fast protons*, Nature, 129:242, 1932.
- [45] Ernest O. Lawrence: *Method and apparatus for the acceleration of ions*, feb 1934. US Patent 1,948,384.
- [46] E.J.N. Wilson: *Fifty years of synchrotrons*, Conf.Proc., C960610:135–139, 1996.
- [47] A. Macchi: *Ion acceleration by superintense laser-plasma interaction*, 2013
- [48] N. López-Pino: *Monte Carlo Semi-Empirical Model for Si(Li) X-Ray Detector: Differences between Nominal and Fitted Parameters*, 2013
- [49] W. Reuter: *Quantitative analysis of complex targets by proton-induced x rays*, 1975
- [50] J. Rickards: *Multilayer PIXE analysis*, S. M. Seltzer
- [51] Website: <https://www-nds.iaea.org/exfor/exfor.htm>, Viktor Zerkin
- [52] N. Otuka: *Towards a More Complete and Accurate Experimental Nuclear Reaction Data Library (EXFOR): International Collaboration Between Nuclear Reaction Data Centres (NRDC)*, 2014

- [53] P. Dimitriou: *Development of a Reference Database for Particle-Induced Gamma-ray Emission spectroscopy*, 2015
- [54] M. Melzani: *Apar-T: code, validation, and physical interpretation of particle-in-cell results*, 2013
- [55] C. K. Birdsall, A. B. Langdon: *Plasma Physics via Computer Simulation*, 2004
- [56] T. D. Arber: *Contemporary particle-in-cell approach to laser-plasma modelling*, 2015
- [57] L. Fedeli: *High Field Plasmonics*, 2015-2016
- [58] A. Formenti: *Intense Laser Interaction with Nanostructured Plasmas: a Kinetic Numerical Investigation*, 2015-2016
- [59] S. Agostinelli: *Geant4—a simulation toolkit*, 2003
- [60] J. Allison: *Geant4 developments and applications*, 2006
- [61] J. Allison: *Recent developments in Geant4*, 2016
- [62] Geant4 Collaboration: *Geant4 User's Guide for Application Developers*, 2015
- [63] Z. Francis: *A comparison between Geant4 PIXE simulations and experimental data for standard reference samples*, 2013
- [64] M. G. Pia: *New models for PIXE simulation with Geant4*, 2010
- [65] A. Mantero: *PIXE simulation in Geant4*, 2011
- [66] K. Amako: *Geant4 and its validation*, 2006
- [67] Website: <https://it.mathworks.com/help/optim/ug/fmincon.html>, 2011
- [68] Da Vinci, L. (1501). *Madonna dei Fusi*. [Tempera on canvas] Private collection, United States: New York
- [69] P. A. Mandò: *Identification of lapis-lazuli pigments in paint layers by PIGE measurements*, 2004
- [70] S. Croft and W. Russ: *A SEMI-EMPIRICAL FORMULA FOR REPRESENTING THE FULL ENERGY PEAK EFFICIENCIES OF PLANAR GE DETECTORS*, 2005
- [71] Lars Anklamm: *A novel von Hamos spectrometer for efficient X-ray emission spectroscopy in the laboratory*, 2014



- [72] A. P. Shevelko: *X-ray spectroscopy of laser-produced plasmas using a von Hamos spectrograph*, 1998
- [73] C. C. Van Den Berg: *High Luminosity Spectrometry in the soft X-Ray Region, I. The Cylinder Spectrometer*, 1955
- [74] Brandr and Lapicki: *L-shell Coulomb ionization by heavy charged particles*, 1979
- [75] Brandr and Lapicki: *Energy-loss effect in inner-shell Coulomb ionization by heavy charged particles*, 1981
- [76] Website: <https://wci.llnl.gov/codes/tart/nuclearatomic.html>, Lawrence Livermore National Laboratory
- [77] Website: <https://www.nist.gov/pml/xcom-photon-cross-sections-database>, Lawrence Livermore National Laboratory
- [78] J. F. Ziegler: *The Stopping and Range of Ions in Solids*, 1985 (new edition in 1996)
- [79] J. F. Ziegler: *SRIM - The Stopping and Range of Ions in Matter*, 2008
- [80] J. Tuli: *Evaluated Nuclear Structure Data File*, 1987
- [81] H. D. Lemmel: *EADL: Evaluated Atomic Data Library of the Lawrence Livermore National Laboratory, USA. Summary documentation*, 1994

# Ringraziamenti

Voglio ringraziare innanzitutto i miei genitori, Enrico e Rosanna, e mia sorella, Maria, per avermi sostenuto durante questo lungo percorso.

Grazie al Professor Matteo Passoni, per avermi seguito e appoggiato costantemente in questo lavoro con professionalità. Grazie anche a Luca Fedeli per avermi assistito e supportato durante tutto lo svolgimento della tesi.

In fine ringrazio di cuore i miei amici, in particolare Sebastian, Alessandro, Daniele, Roberto, Cristiano, Marco, Luca, Mirko e Davide per avermi incoraggiato ed essermi sempre stati vicino durante questa parte impegnativa della mia vita.